Theresa Schmidt, BSc

IDEAL-fat-water separation for analysis of subcutaneous haemorrhage degradation

Master's Thesis

to achieve the university degree of

Diplom - Ingenieurin

Master's degree programme: Biomedical Engineering

submitted to

Graz University of Technology

Supervisor

Univ.-Prof. Dipl.-Ing. Dr.techn. Rudolf Stollberger

Institute of Medical Engineering

Head: Univ.-Prof. Dipl.-Ing. Dr.techn. Rudolf Stollberger

Graz, May 2018

Statutory Declaration

I declare that I have authored this thesis independently, that I have not used other than the declared sources/resources, and that I have explicitly indicated all material which has been quoted either literally or by content from the sources used. The text document uploaded to TUGRAZonline is identical to the present master's thesis dissertation.

Eidesstattliche Erklärung

Ich erkläre an Eides statt, dass ich die vorliegende Arbeit selbstständig verfasst, andere als die angegebenen Quellen/Hilfsmittel nicht benutzt, und die den benutzten Quellen wörtlich und inhaltlich entnommenen Stellen als solche kenntlich gemacht habe. Das in TUGRAZonline hochgeladene Textdokument ist mit der vorliegenden Dissertation identisch.

Date

Signature

Abstract

IDEAL-fat-water separation for analysis of subcutaneous haemorrhage degradation

The detection and age of subcutaneous haematoma is necessary in forensic medicine for the reconstruction of events. The current clinical standard for this is visual assessment. This approach is highly subjective and several attempts have been made to find more objective methods. This work ascertains a new possible method for age assessment through water-fat decomposition of MRI images via the IDEAL-algorithm (iterative decomposition with echo asymmetry and least-squares estimation). The fat and water images of haematoma at different time points from several test subjects were used to attain the sizes and mean water fractions. The normalized size and mean water fraction trends were analysed through the means of regression analysis. The calculated regression models show that both size and mean water fraction trends are subject to exponential decay. The similar water fraction decay rate for all test subjects indicates possible age dependency of the haematoma's mean water fraction.

Keywords: IDEAL, Dixon Methods, fat water separation, subcutaneous haematoma, chemical shift

Kurzfassung

IDEAL-Fett-Wasser Trennung für Analyse der Degradierung subkutaner Blutungen

Die Detektion und Altersbestimmung subkutaner Hämatome ist essentiell für die Rekonstruktion von Tatbeständen in der Gerichtsmedizin. Der derzeitige klinische Standard ist die visuelle Begutachtung der Hämatome. Dieses Vorgehen führt zu sehr subjektiven Resultaten, daher wurden einige Versuche unternommen um objektivere Methoden zu ermitteln. Diese Arbeit untersucht einen neuen Ansatz der Altersbestimmung anhand von Wasser-Fett-Trennung der MR-Bilder durch den IDEAL-Algorithmus (Iterative Dekomposition mit Echo Asymmetrie und Least-Squares Schätzung). Anhand der getrennten Wasser und Fett Bilder der Hämatome zu unterschiedlichen Zeitpunkten wurde der zeitliche Größenverlauf und der zeitliche Verlauf des mittleren Wasseranteils für verschiedene Probanden berechnet. Die Regressionsmodelle für den normalisierten Größen- und den Wasseranteilverlauf zeigen jeweils einen exponentiellen Zerfall. Eine ähnliche Zerfallsrate für den Wasseranteil bei allen Probanden deutet auf einen möglichen Zusammenhang zwischen Alter und mittleren Wasseranteil eines Hämatoms hin.

Schlüsselwörter: IDEAL, Dixon Methode, Fett Wasser Trennung, subkutane Hämatoma, chemische Verschiebung

Acknowledgement

I would like to acknowledge everyone who played a role in my academic accomplishments.
First of all, my parents, who supported me with love and understanding. Without you, I could never have reached this current level of success.
Secondly, my sister and her husband, who are to be thanked for the absences of spelling errors. Any remaining errors exist in spite of their efforts.
Thirdly, my boyfriend for multiple proof-readings and overall patience. Without you, this process would have taken much longer.
Fourthly, Dipl.-Ing. Andreas Petrovic and my supervisor Univ.-Prof. Dipl.-Ing. Dr.techn. Rudolf Stollberger, each of whom has provided patient advice and guidance throughout the research process.
Lastly, I would liked to express my thanks to the Ludwig Boltzmann Institute for clinical forensic imaging for providing the MRI data for this study.

Contents

List of Figures

List of Tables

1. Introduction

The signal detected by clinical magnetic resonance imaging (MRI) applications is generated by protons, as they make up over 90 % of nuclei in the human body [1]. These protons are mostly part of water, bound to molecules, or are present in fatty tissue. Because of relatively short T_1 relaxation time of the fat signal (about 230 ms at 1.5 T), fatty tissue appears hyper-intense in many clinical imaging sequences and therefore obscures underlying pathology such as oedema, inflammation, enhancing tumours or mild haemorrhage, as shown in figure 1.1.

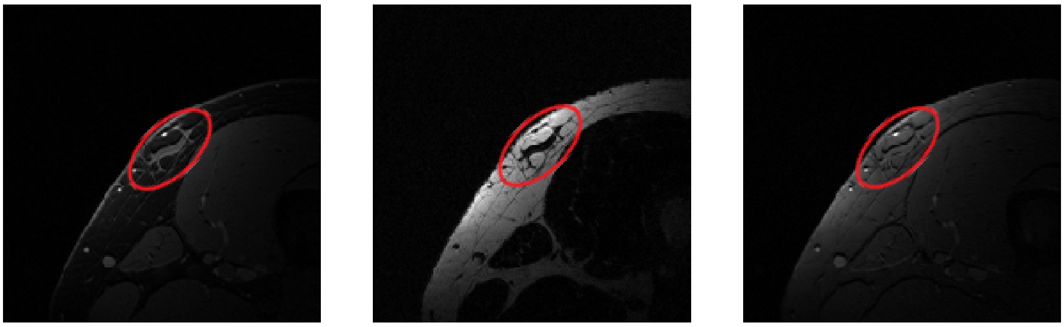

(a) Water-only image (b) Fat-only image (c) Original image

Figure 1.1.: Images of the internal anterior side of the thigh with a subcutaneous haematoma (circled in red). In the original image the haematoma is hardly distinguished from its surrounding. The haematoma is prominent in the water and fat image, as it either appears hyper-intense or hypo-intense to its surrounding.

To avoid misdiagnoses due to high fat signals, reliable fat suppression is necessary in many areas of clinical MRI. Additionally it may improve contrast if the anatomical origin of interest is embedded in or contains fatty tissue.

Most clinical protocols use fat suppression methods to eliminate the fat signal and improve the visualization of these abnormalities. Such methods are chemically selective fat suppression pulses (FAT-SAT), which partly saturate the fat tissue, spatial-spectral pulses (water excitation), which directly excite the water signal or short inversion time inversion recovery (STIR), which times its initial inversion pulse in a way that neutralises the fat signal. [1]

These fat suppression methods suffice for many clinical applications, however fat saturation routinely fails for extremity, off-isocenter and large field view imaging. In addition for some body areas such as the brachial plexus and the skull base. [2] This failure can be due to the sensitivity of spectrally selective RF pulse to both B_1 non-uniformity and B_0 inhomogeneity or the sensitivity of STIR to B_1 non-uniformity.
Another approach to the problem of hyper-intense fat signals is to separate the water and fat signals based on the chemical shift in post processing. The additionally gained information about the relative composition of fat and water can improve the diagnosis of bone marrow disease, some liver diseases and adrenal masses.[3]

One application for the fat suppression or water-fat separation methods is the enhancement of contrast between a haemorrhage and its surrounding tissue. The use of MRI for detection and analysis of intracranial haemorrhage is routine for clinical radiologists. The same cannot be said about

extracranial haemorrhage. This is mainly because the detection and investigation of extracranial haemorrhage, such as subcutaneous haematoma, rarely have diagnostic or therapeutic consequences.
This futility does not apply in the domain of forensic medicine, as haematoma and other injuries build the basis for the reconstruction of events. The current clinical standard for detection and age determination of a haematoma is visual assessment. This technique is highly subjective, thus several attempts to find objective and quantitative methods have been made. The application of MRI for detection of haematoma for forensic cases has gathered more interest recently, however there is still only limited experience. [4] [5] [6]

The aim of this thesis is to **(a)** use an iterative least-squares fat-water separation method to detect subcutaneous haematoma, **(b)** determine their relative size and the average water fraction and **(c)** to analyse the time-dependent change of the size and the water fraction.
The used separation method is the iterative decomposition with echo asymmetry and least-squares estimation (IDEAL) algorithm. This method is a refined version of the chemical shift based original Dixon water-fat separation.

1.1. Chemical shift

Depending on their molecular surrounding, protons experience different strengths of electronic shielding. The triglyceride molecules shield the protons on average stronger than the dihydrogen molecules. This results in

different microscopic magnetic fields and consequently different larmor frequencies for the individual protons depending on the molecular surrounding.
This phenomenon is called the chemical shift δ:

$$\delta = \frac{\nu_{sample} - \nu_{ref}}{\nu_{ref}} \tag{1.1}$$

Eq. 1.1 shows the chemical shift δ in ppm of a sample compound, where ν_{sample} is the absolute resonance frequency of the sample and ν_{ref} is the absolute resonance frequency of a standard reference compound. Generally, the standard reference compound used in medical MRI is water. [7]

$$\Delta f_{cs} = \frac{\gamma}{2\pi} B_0 \cdot \delta \cdot 10^{-6} \tag{1.2}$$

As defined in equation 1.2, the resonance frequency offset Δf_{cs} between the sample and the reference compound is directly proportional to the main magnetic field B_0, the gyromagnetic ration γ and the chemical shift δ between sample and reference. [1]

Figure 1.2 shows the nuclear magnetic resonance (NMR) spectrum of a water-fat mixture at 3 T. The spectrum demonstrates a single resonance peak for water and the main fat peak resonating 420 Hz slower.
Fat has a complex spectrum with multiple peaks due to the different individual fat molecules. Despite these complexities, the main contributing fat molecules are methylene and a few other proton species. The resonance

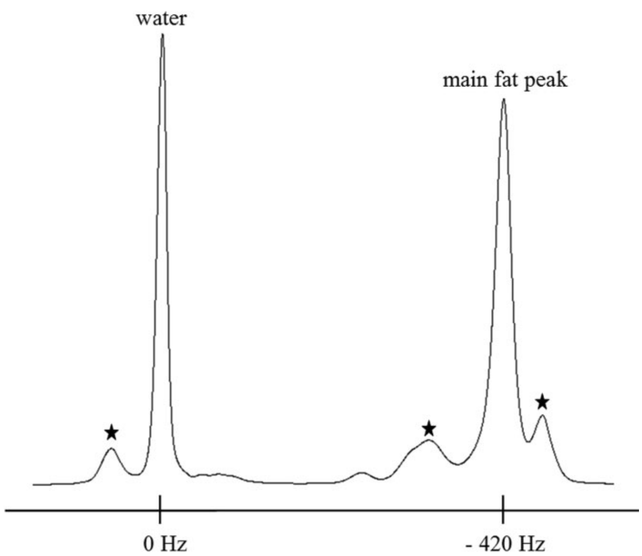

Figure 1.2.: NMR spectrum of water-fat mixture acquired at 3 T demonstrates the chemical shift between fat and water. (*) notes several additional fat peaks. Adapted from [1]

frequencies of these few lipid species are clustered around approximately 3.5 ppm down-field from the single water resonance peak. Aside from this fat species, a slight fat peak very closely to the water peak at approximately 0.5 ppm up-field from water is also noticeable. These multiple fat signal contributors generally result in a complex magnetization for fat, however for simplicity most separation techniques approximate the fat spectrum as consisting of two broadened peaks, with one at 3.5 ppm down-field from water and the another at its resonance. This approximation is satisfying for most applications, as the single fat resonance peak at approximately 3.5 ppm usually contains more than 10 times the signal energy of any other fat peak. [8]

1.2. Dixon Methods

The Dixon techniques achieve fat-water separation in post-processing after a modified data acquisition encoded the chemical shift difference into the signal phase.

1.2.1. Signal Model in Dixon Methods

Most Dixon techniques assume that water and fat are the only two signal-contributing chemical species. Under this assumption, the complex signal of a pixel at the spatial coordinates (x, y) is given as:

$$S(x,y) = [W(x,y) + F(x,y) \cdot e^{i\alpha}] \cdot e^{i\phi(x,y)} \cdot e^{i\phi_0(x,y)} \tag{1.3}$$

$W(x, y)$ and $F(x, y)$ are generally real, non-negative numbers and proportional to the magnitudes of the water or fat magnetizations. The phase differences between the fat and water magnetization are represented by α. The signal experiences further phase shifts because of ϕ, an error phase due to the B_0 inhomogeneity, and ϕ_0, another error phase caused by other system imperfections, such as spatial dependence of RF penetration and different signal time delays in the receiver chains. The vector relationship of equation 1.3 is illustrated in figure 1.3.

Typically Dixon techniques require several images with a specific set of α values. To achieve a desired value of α, the echo time (TE) is changed. This time change in the gradient echo sequence or time shift from a spin echo

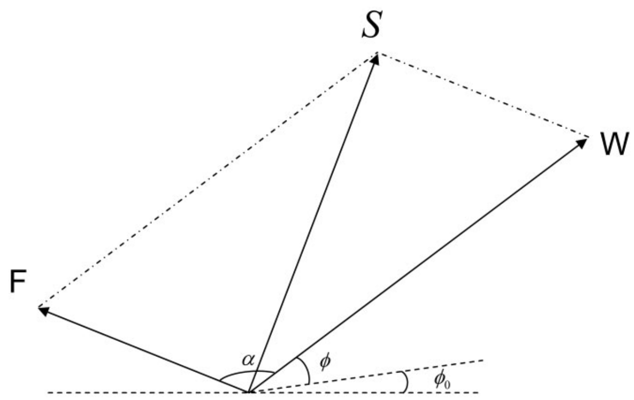

Figure 1.3.: Vector representation of the complex signal S as defined in equation 1.3. Reprinted from [8]

in the spin echo sequence is given by Δt. The resulting α caused by Δt is defined in equation 1.4.

$$\alpha = \gamma \cdot B_0 \cdot \delta \cdot \Delta t \tag{1.4}$$

Where γ is the proton gyromagnetic ration, δ is the chemical shift of fat relative to water and B_0 is the externally applied magnetic field. The phase angle due to B_0 inhomogeneity ϕ is also proportional to Δt (see equation 1.5).

$$\phi = \gamma \cdot \Delta B_0 \cdot \Delta t \tag{1.5}$$

Besides $W(x, y)$ and $F(x, y)$, ϕ, ϕ_0 and ΔB_0 are also spatially dependent and may vary from pixel to pixel. Though α is principally affected by changes in ΔB_0, these changes are negligible compared to the magnitude of B_0. Therefore, α can be considered as independent of B_0 and only affected by Δt and the chemical shift δ (see equation 1.4).[8]

The major distinctions between particular Dixon techniques consist in the amount of images acquired per slice, different sets of α values, the sampling and post-processing strategies. Counting on the amount of images acquired for post-processing, the techniques are classified as the one-, two-, three-, or four-point Dixon technique. Algorithms that are adaptable to different amounts of images are called multi-point Dixon techniques. Furthermore, these procedures are distinguished by the specific α values. The original approach requires two images and is usually known as the Original Two-Point Dixon Method (2PD).

1.2.2. The Original Two-Point Dixon Method

The two images needed for the fat-water separation applying the original 2PD method are acquired using the RF spin echo sequence shown in figure 1.4. The in-phase image I_0 is acquired when the fat and water magnetization are in phase ($\Delta t = 0$). The RF pulse for the out-of-phase image I_1 is either advanced or delayed by $\Delta t/2$, thus creating a phase angle α between the water and fat magnetization of $\pm$ 180°. Therefore, the original Dixon approach can be referred to as a two-point Dixon technique with a (0,$\pm$180°) or (0, $\pm\pi$) acquisition scheme.

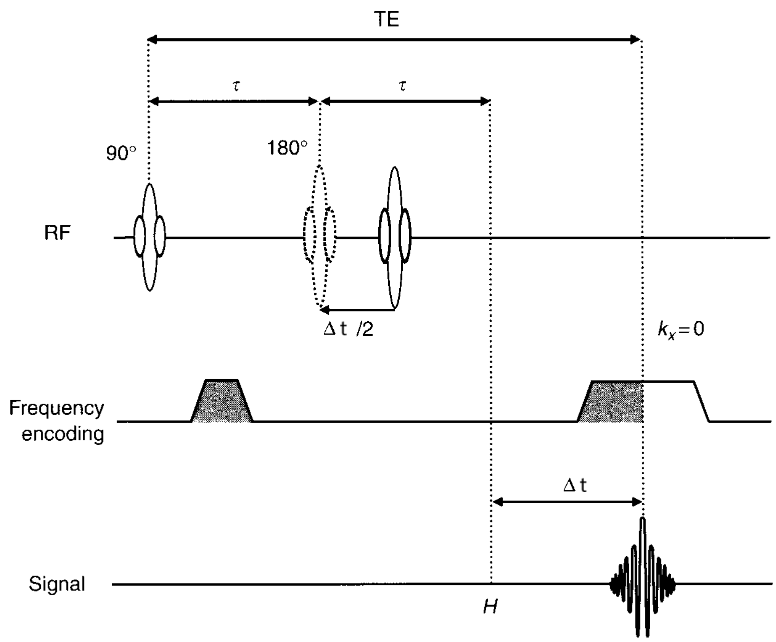

Figure 1.4.: 2PD RF spin echo pulse sequence. The RF spin echo is delayed by Δt if the 180° RF Impulse is delayed by $\Delta t/2$. Adapted from [3]

The magnitude of Δt depends on the resonance frequency offset Δf_{cs} between water and fat (see Eq. 1.6).

$$\Delta t = \frac{1}{2\Delta f_{cs}} \tag{1.6}$$

The image contrast of the two acquired images is heavily determined by the peak signal amplitude that occurs at $k_x = 0$. Assuming that the water and fat magnetization are as shown in figure 1.5, the complex images I_0 and I_1 can be approximately given by:

$$I_0 = (W + F) \cdot e^{i\phi_0}$$
$$I_1 = (W - F) \cdot e^{i\phi} \cdot e^{i\phi_0} \tag{1.7}$$

where W and F are the water and fat image, respectively.

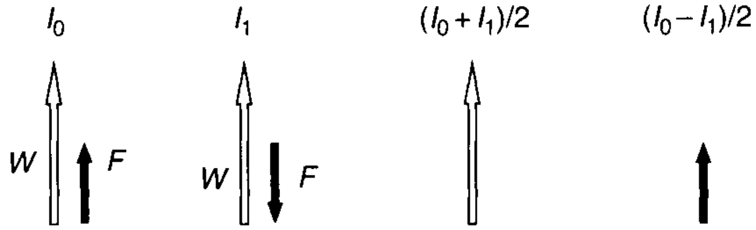

Figure 1.5.: Fat and water magnetization for the in-phase image I_0, the out-of-phase image I_1 and combined images assuming no B_0 inhomogeneity or magnetic susceptibility perturbation. Adapted from [3]

The original 2DP assumes perfect B_0 homogeneity ($\phi = 0$) and no image weighting from T_2^* relaxation, diffusion and flow or from other phase shifts that occur due to hardware group delays, eddy currents and B_1 receive-field nonuniformity ($\phi_0 = 0$).

Therefore, W and F can be determined directly by adding or subtracting I_0 and I_1, as shown in Eq. 1.8.

$$W = \frac{1}{2}(I_0 + I_1)$$
$$F = \frac{1}{2}(I_0 - I_1) \tag{1.8}$$

The assumption of $\Delta B_0 = 0$ and thus $\phi = 0$ is virtually never valid. The additional phase shift due to ΔB_0 prevents a clean water and fat separation as shown in figure 1.6.

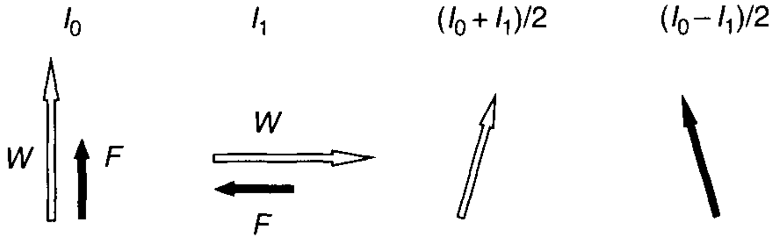

Figure 1.6.: Fat and water magnetization for the in-phase image I_0, the out-of-phase image I_1 and combined images assuming that B_0 inhomogeneity creates a phase shift $\phi = 90°$ between in-phase and out-of-phase images, which causes an overestimation of fat and unterestimation of water. Adapted from [3]

One solution to the B_0 sensitivity is to form the magnitude of I_0 and I_1 before summation and subtraction (see equation 1.9).

$$W = \frac{1}{2}(|I_0| + p_c|I_1|)$$
$$F = \frac{1}{2}(|I_0| - p_c|I_1|) \tag{1.9}$$

With this approach every pixel value of the water image W is the dominant signal of the corresponding pixel, regardless whether the dominant signal contributor is fat or water. This requires a binary choice p_c whether W represents the water or fat image for every pixel. Several techniques for calculating p_c exist, such as the extended Two-Point Dixon Method or Three-Point Dixon Methods (3PD). [3] [8]

1.2.3. The Three-Point Dixon Methods

One way for compensate the B_0 inhomogeneities is to acquire a third image with the modified acquisition scheme of either ($-\alpha$, 0, α) or (0, α, 2α). These 3PD techniques use the additional information to calculate a B_0 field inhomogeneity image ("field map"). The early 3PD techniques used $\alpha = 180°$ and following the same notations as for equation 1.7, the third image can then be written as:

$$
\begin{aligned}
I_{-1} &= (W - F) \cdot e^{-i\phi} \cdot e^{i\phi_0} \quad \text{for } (-180°, 0, 180°) \\
I_2 &= (W + F) \cdot e^{i2\phi} \cdot e^{i\phi_0} \quad \text{for } (0, 180°, 360°)
\end{aligned}
\tag{1.10}
$$

ϕ can be calculated by combining equations 1.7 and 1.10.

$$
\begin{aligned}
\hat{\phi} &= \frac{1}{2} \cdot \arctan[I_1 \cdot I^*_{-1}] \quad \text{for } (-180°, 0, 180°) \\
\hat{\phi} &= \frac{1}{2} \cdot \arctan[I_2 \cdot I^*_0] \quad \text{for } (0, 180°, 360°)
\end{aligned}
\tag{1.11}
$$

Assuming that ϕ is determined correctly (i.e. $\phi = \hat{\phi}$), the B_0 inhomogeneity effects can be removed from the signal equation 1.7 and the water and fat images can be calculated. The limitation of the arctan operator within the range of $-\pi$ to π creates the problem of phase wrapping. As the equation for α (see eq. 1.4) indicates, phase wrapping occurs when ΔB_0 is more than half the chemical shift difference (in the cases of water and fat: ≈ 1.75 ppm). Phase unwrapping is necessary in most 3PD approaches.

As most phase unwrapping algorithms lack the robustness for routine clinical practice, other techniques have been introduced. Such procedures are direct phase encoding (DPE) or the IDEAL-algorithm that manage the separation without phase unwrapping. [8]

2. Methods

2.1. Materials

This thesis used MRI scans from the same data set as in the papers [4] and [9]. Scans of 34 test subjects were provided. Early on, 3 test subjects were excluded because of technical reasons like severe motion artefacts. Some scans of other test subjects with motion artefacts were also excluded, however enough usable scans of the concerned test subjects remained.

The final data set consists of MRI scans of the thigh of the 31 healthy test subjects (16 females, 15 male, mean age $\pm$ standard deviation: 24,61 $\pm$ 2,98 y). The haematoma was artificially created by an injection of 4 ml of their own venous blood into the subcutaneous fatty tissue of the internal anterior side of the thigh. The haematoma was examined with MRI (3T, TimTrio, Siemens AG, Germany) directly after the injection and after 3 hours, 1 day, 3 days, 1 and 2 weeks. For 15 of the test subjects, an additional base line scan before the injection was provided. These base line scans were included into the calculation of the decomposition images. However later on they were emitted from any size or water fraction determination. For detailed information about the data set see appendix chapter B.

Besides other MRI sequences, the necessary sequence for the acquisition scheme was applied. This obtained one image, in which fat and water are in quadrature and two images, in which they are $\pm 120°$ from quadrature. The combination of phase shifts at $(-\pi/6, \pi/2, 7\pi/6)$ optimizes the noise performance, as it provides an uniform sampling around the unit circle [10]. The spatial relationship of the water and fat magnetization at each phase shift is illustrated in figure 2.1.

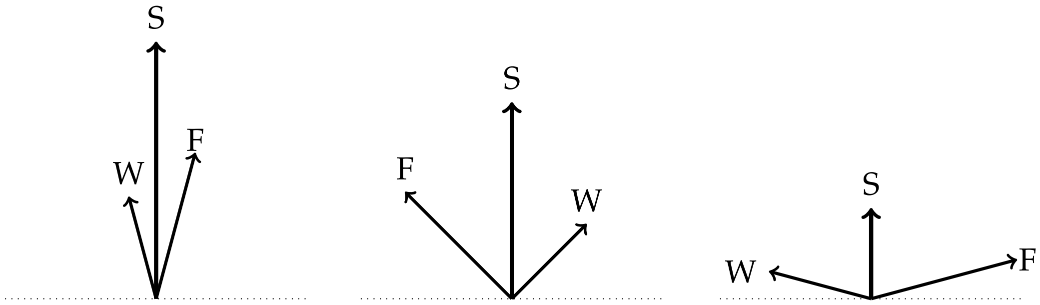

(a) 120° before quadrature or $-\pi/6$ (TE_1)　(b) quadrature or $\pi/2$ (TE_2)　(c) 120° after quadrature or $7\pi/6$ (TE_3)

Figure 2.1.: Spatial relationship of the fat and water magnetization during the different phase shift of the acquisition scheme and the resulting complex signal vector.

The sequence parameters of the acquisition are listed in table 2.1. Table 2.2 shows the different echo times (TE) used to achieve the desired acquisition scheme, where TE_2 is the TE for the in quadrature acquisition and TE_1 and TE_3 are the echo times for the out-of-phase acquisition.

Table 2.1.: Acquisition parameters

Sequence Variation	Sequence Type	In-plane resolution (mm^2)	Slice thickness (mm)	Slices
GR	SP\OSP	0.625×0.625	1.5	3

Acquisition parameters of the used MR sequence for the IDEAL-algorithm

Table 2.2.: Echo Times

TE_1	TE_1	TE_1
4.72	5.54	6.36

Specific TE used for the acquisition of the 3 MR images

All calculations for the fat-water separation, the segmentation, size determination and regression analysis were produced using MATLAB 20015b ([11], www.mathworks.com). The preliminary segmentation was done manually using the ITK-SNAP software ([12], www.itksnap.org).

2.2. IDEAL-Algorithm

The IDEAL-algorithm can theoretically separate as many species with chemical shift differences as required. The number of different species is only limited by practicality and necessity. To achieve the decomposition of n species, $n+1$ images of the same slice at different TEs are required. This thesis' goal demands the separation of only water and fat, thus the theory of the IDEAL-algorithm will be applied to only two species. For the more generic formulas see paper [13].

2.2.1. Theory

The signal model from equation 1.3 can be rewritten as:

$$S_n(x,y) = [W(x,y) + F(x,y) \cdot e^{i2\pi\Delta f_{cs} t_n}] \cdot e^{i2\pi\psi(x,y)t_n} \tag{2.1}$$

where $S_n(x,y)$ is the complex signal from the pixel (x,y) of the nth acquired image, $\psi(x,y)$ is the local magnetic resonance offset and t_n is the echo time. The signal model specific for the IDEAL algorithm sees $W(x,y)$ and $F(x,y)$ as complex terms [1] with their own magnitude and phase. The phase shifts due to ϕ and ϕ_0 in equation 1.3 are combined to $\phi + \phi_0 = 2\pi\psi t$.

Equation 2.1 contains 5 unknowns, the scalar unknown $\psi(x,y)$, the magnitudes and phases of the two complex unknowns $W(x,y)$ and $F(x,y)$. As each acquired MRI image contributes a real and an imaginary measurement, 3 acquisitions are required to determine the system and separate fat from water.

For simplicity the explicit dependence of W, F, ψ and S_n on the spatial coordinates (x,y) will be left out hereafter. The IDEAL-algorithm uses Gaus-Newton algorithm [14] to approximate the true field map.

Given an initial estimation of the field map ψ_0 (e.g. $\psi_0 = 0$), equation 2.1 can be rewritten as:

$$\hat{S}_n = S_n \cdot e^{-i2\pi\psi_0 t_n} = W + F \cdot e^{i2\pi\Delta f_{cs} t_n} \tag{2.2}$$

[1] The generic signal model for Dixon model in chapter 1 explained the complex signal $S(x,y)$ as sum of the magnitudes of water and fat. The adapted signal model for the IDEAL-algorithm assumes water and fat as complex signals with their own magnitude and phase.

Equation 2.2 can be split in its real and imaginary parts:

$$\begin{aligned}\hat{S}_n &= \hat{S}_n^R + i\hat{S}_n^I \\ &= W^R + F^R\cos(2\pi\Delta f_{cs}t_n) - F^I\sin(2\pi\Delta f_{cs}t_n) \\ &+ i[W^I + F^R\sin(2\pi\Delta f_{cs}t_n) + F^I\cos(2\pi\Delta f_{cs}t_n)]\end{aligned} \tag{2.3}$$

As 3 images are acquired for each slice ($n = 0\ldots2$), the equation 2.3 results in a linear system of equations, which can be written in matrix format:

$$\hat{\mathbf{S}} = \mathbf{A}\mathbf{p} \tag{2.4}$$

with $\hat{\mathbf{S}}$ as the estimated signal vector, $\mathbf{A}$ as the system matrix and $\mathbf{p}$ as the component vector, which contains the real and imaginary parts of the signals contributed by water and fat (see 2.5 - 2.7).

$$\hat{\mathbf{S}} = \begin{bmatrix}\hat{S}_0^R & \hat{S}_1^R & \hat{S}_2^R & \hat{S}_0^I & \hat{S}_1^I & \hat{S}_2^I\end{bmatrix}^T \tag{2.5}$$

$$\mathbf{p} = \begin{bmatrix}W^R & W^I & F^R & F^I\end{bmatrix}^T \tag{2.6}$$

$$\mathbf{A} = \begin{bmatrix}1 & 0 & \cos(2\pi\Delta f_{cs}t_0) & -\sin(2\pi\Delta f_{cs}t_0) \\ 1 & 0 & \cos(2\pi\Delta f_{cs}t_1) & -\sin(2\pi\Delta f_{cs}t_1) \\ 1 & 0 & \cos(2\pi\Delta f_{cs}t_2) & -\sin(2\pi\Delta f_{cs}t_2) \\ 0 & 1 & \sin(2\pi\Delta f_{cs}t_0) & \cos(2\pi\Delta f_{cs}t_0) \\ 0 & 1 & \sin(2\pi\Delta f_{cs}t_1) & \cos(2\pi\Delta f_{cs}t_1) \\ 0 & 1 & \sin(2\pi\Delta f_{cs}t_2) & \cos(2\pi\Delta f_{cs}t_2)\end{bmatrix} \tag{2.7}$$

With t_0, t_1 and t_2 representing the echo times of the three acquired images. Solving the linear systems of equations using a least-squares fitting approach it can be shown that:

$$\hat{\mathbf{p}} = (\mathbf{A^T A})^{-1} \mathbf{A^T} \hat{\mathbf{S}} \tag{2.8}$$

The estimation of the real and imaginary part of water and fat only holds true if $\psi_0 = \psi$ (see 2.2). To obtain a better estimation for $\hat{\mathbf{p}}$ the initial field map ψ_0 has to be refined.

Assuming that $W^R = \hat{W}^R + \Delta W^R$, $W^I = \hat{W}^I + \Delta W^I$, $F^R = \hat{F}^R + \Delta F^R$, $F^I = \hat{F}^I + \Delta F^I$ and $\psi = \psi_0 + \Delta\psi$, then equation 2.1 can be written as:

$$S_n \approx [\hat{W} + \Delta W + (\hat{F} + \Delta F) \cdot e^{i2\pi\Delta f_{cs} t_n}] \cdot e^{i2\pi\psi_0 t_n} \cdot e^{i2\pi\Delta\psi t_n} \tag{2.9}$$

Using the Taylor approximation $e^{i2\pi\Delta\psi t_n} \approx 1 + i2\pi\Delta\psi t_n$, dividing each side by $e^{i2\pi\psi_0 t_n}$ and accounting for equation 2.2 leads to:

$$\begin{aligned} &\hat{S}_n^R + i\hat{S}_n^I = \\ &[\hat{W}^R + \Delta W^R + i(\hat{W}^I + \Delta W^I) + (\hat{F}^R + \Delta F^R + i(\hat{F}^I + \Delta F^I)) \\ &\quad \cdot (\cos(2\pi\Delta f_{cs} t_n) + i\sin(2\pi\Delta f_{cs} t_n))] \cdot (1 + i2\pi\Delta\psi t_n) \end{aligned} \tag{2.10}$$

Equation 2.10 is rearranged and split into its real and imaginary components to obtain a better approximation:

$$\begin{aligned}\hat{\hat{S}}_n^R &= \hat{S}_n^R - \hat{W}^R - \hat{F}^R \cdot \cos(2\pi\Delta f_{cs} t_n) + \hat{F}^I \cdot \sin(2\pi\Delta f_{cs} t_n) \\ &= 2\pi\Delta\psi \cdot [-\hat{W}^I - \hat{F}^R \cdot \sin(2\pi\Delta f_{cs} t_n) - \hat{F}^I \cdot \cos(2\pi\Delta f_{cs} t_n)] \\ &+ \Delta W^R + \Delta F^R \cdot \cos(2\pi\Delta f_{cs} t_n) - \Delta F^I \cdot \sin(2\pi\Delta f_{cs} t_n)\end{aligned} \tag{2.11}$$

$$\begin{aligned}\hat{\hat{S}}_n^I &= \hat{S}_n^I - \hat{W}^R - \hat{F}^R \cdot \cos(2\pi\Delta f_{cs} t_n) - \hat{F}^I \cdot \sin(2\pi\Delta f_{cs} t_n) \\ &= 2\pi\Delta\psi \cdot [\hat{W}^R + \hat{F}^R \cdot \cos(2\pi\Delta f_{cs} t_n) - \hat{F}^I \cdot \sin(2\pi\Delta f_{cs} t_n)] \\ &+ \Delta W^I + \Delta F^R \cdot \sin(2\pi\Delta f_{cs} t_n) + \Delta F^I \cdot \cos(2\pi\Delta f_{cs} t_n)\end{aligned} \tag{2.12}$$

The new system of linear equations can be written in matrix format:

$$\hat{\hat{\mathbf{S}}} \approx \mathbf{B}\mathbf{y} \tag{2.13}$$

with **B** as the coefficient matrix and **y** as the error vector, which contains the differences between the old and refined values for ψ, W^R, W^I, F^R and F^I (see 2.14 - 2.17).

$$\hat{\hat{\mathbf{S}}} = \begin{bmatrix} \hat{\hat{S}}_0^R & \hat{\hat{S}}_1^R & \hat{\hat{S}}_2^R & \hat{\hat{S}}_0^I & \hat{\hat{S}}_1^I & \hat{\hat{S}}_2^I \end{bmatrix}^T \tag{2.14}$$

$$\mathbf{y} = \begin{bmatrix} \Delta\psi & \Delta W^R & \Delta W^I & \Delta F^R & \Delta F^I \end{bmatrix}^T \tag{2.15}$$

$$\mathbf{B} = \begin{bmatrix} g_0^R & 1 & 0 & \cos(2\pi\Delta f_{cs} t_0) & -\sin(2\pi\Delta f_{cs} t_0) \\ g_1^R & 1 & 0 & \cos(2\pi\Delta f_{cs} t_1) & -\sin(2\pi\Delta f_{cs} t_1) \\ g_2^R & 1 & 0 & \cos(2\pi\Delta f_{cs} t_2) & -\sin(2\pi\Delta f_{cs} t_2) \\ g_0^I & 0 & 1 & \sin(2\pi\Delta f_{cs} t_0) & \cos(2\pi\Delta f_{cs} t_0) \\ g_1^I & 0 & 1 & \sin(2\pi\Delta f_{cs} t_1) & \cos(2\pi\Delta f_{cs} t_1) \\ g_2^I & 0 & 1 & \sin(2\pi\Delta f_{cs} t_2) & \cos(2\pi\Delta f_{cs} t_2) \end{bmatrix} \tag{2.16}$$

$$\begin{aligned} g_n^R &= 2\pi t_n \cdot [-\hat{W}^I - \hat{F}^R \sin(2\pi\Delta f_{cs} t_n) - \hat{F}^I \cos(2\pi\Delta f_{cs} t_n)] \\ g_n^I &= 2\pi t_n \cdot [\hat{W}^R + \hat{F}^R \cos(2\pi\Delta f_{cs} t_n) - \hat{F}^I \sin(2\pi\Delta f_{cs} t_n)] \end{aligned} \tag{2.17}$$

As with the system 2.4 the estimates of $\mathbf{y}$ can be calculated by:

$$\mathbf{y} = (\mathbf{B^T B})^{-1} \mathbf{B^T} \hat{\hat{\mathbf{S}}} \tag{2.18}$$

The calculated error terms in $\mathbf{y}$ are used to recalculate $\hat{\hat{\mathbf{S}}}_\mathbf{n}$ (see equations 2.11 and 2.12). This refinement is repeated until $\Delta\psi$ is small enough (e.g. < 1 Hz). After this least-squared approach has been completed for each pixel, the final field map ψ is spatially filtered with a low pass to reduce noise. As the last step the final estimation of water and fat are calculated with the equation 2.4. [13]

The flow chart in figure 2.2 visualizes the IDEAL-method.

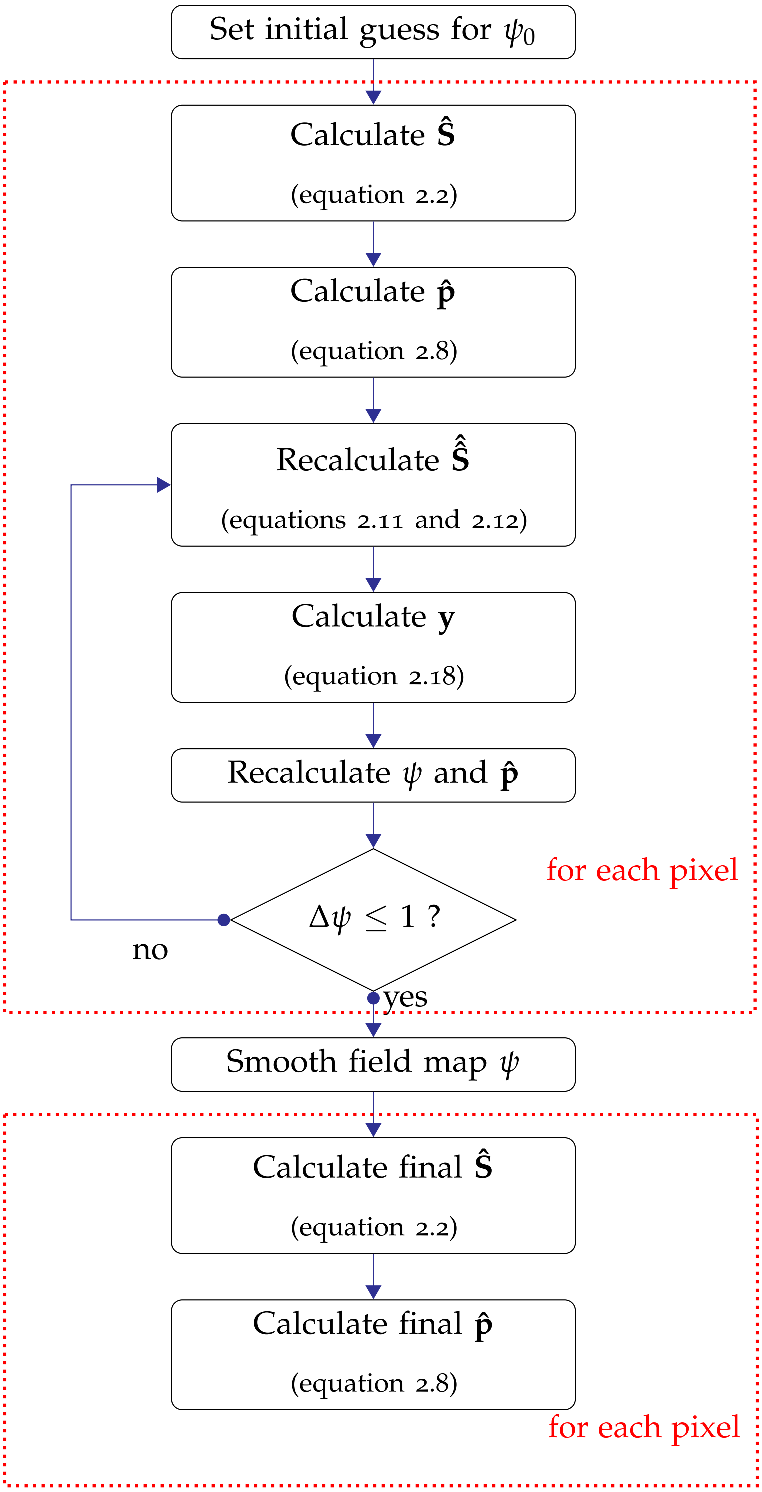

Figure 2.2.: Flowchart illustration of the IDEAL-algorithm. The dotted red bordered part is performed for each pixel individually.

2.2.2. Implementation

The IDEAL-algorithm was implemented in MATLAB 2015b. The created script consists of three main steps:

1. Import and preprocessing of the MRI data
2. Separation via the IDEAL-algorithm
3. Export of the decomposed images

The location of the MRI data acquired for the IDEAL approach is determined by the function $getpaths()$. Using the folder paths provided by $getpaths()$, the function $getfiles()$ reads in the MRI data sets and preprocesses it. The magnitude images are not changed after read in, however the phase images are normalized to a range of $-\pi$ to π. The IDEAL-algorithm expects complex images, so the imported magnitude and phase images are recombined. The complex images, a vector storing the relevant chemical shifts, a vector including all echo times, a matrix containing the initial guess of the field map (e.g.: $\psi_0 = 0$) and the resonance frequency are the inputs for the function $ideal()$.

This procedure implements the algorithm shown in figure 2.2. As with the theoretical algorithm, the MATLAB function $ideal()$ is capable to separate more than two compounds (e.g. fat, water and silicone). Mostly the theoretical algorithm and the implemented procedure concur. Differences exist in two places:

1. The matrix **B** (see equation 2.16) can become singular if the current complex pixel is zero (e.g.: due to measurement errors). A singular matrix has no inverse, thus rendering the solution of equation 2.18 impossible. To prevent MATLAB warning in such cases, the function *ideal*() tests for singularity before executing the matrix division. If the matrix is singular, the pseudo inverse is used to solve the linear system of equations, as shown in the listing 2.1.

   Listing 2.1: MATLAB code that tests for singular Matrix

```
if rcond(B.'*B) > eps
    y = (B.'*B)\(B.'*S);
else
    y = pinv(B.'*B)*B.'*S;
end
```

2. The requirement $\Delta\psi < 1$ Hz can lead to an endless loop. A counter was introduced to escape the iterative least-squares phase of the algorithm after 10000 tries.

The function *ideal*() returns a 3 dimensional complex matrix. This matrix contains all decomposed complex images and the complex source image at quadrature. The calculated field map ψ and a binary map showing instances, in which the iterative approach has diverged, are optional outputs.

After the decomposition the magnitude of the calculated fat and water images and the original one at quadrature are written into a result folder by the MATLAB function *dcmsave*().

The flow chart in figure 2.3 illustrates the MATLAB script, in which the implemented IDEAL-algorithm was embedded.

The IDEAL-algorithm determines the field map by minimizing a cost function. This makes the algorithm vulnerable to local minima entrapment. The initial estimation for the field map ψ_0 heavily influences the success of the decomposition (see figures 3.2 and 3.3). The default assumption of no B_0 inhomogeneities ($\psi = 0$) is suitable for a large set of the data. However, for some MRI scans, this assumption of homogeneity caused imperfect decomposition. In these cases different values for ψ_0 were tested. As a rather homogeneous B_0 field was still likely, values in the range of -0.3 to 0.3 were declared as the new initial field map. The specific values for each MRI scan are listed in appendix table B.2. Some MRI scans were excluded as no correct decomposition could be achieved. [15] [16] [17] [18]

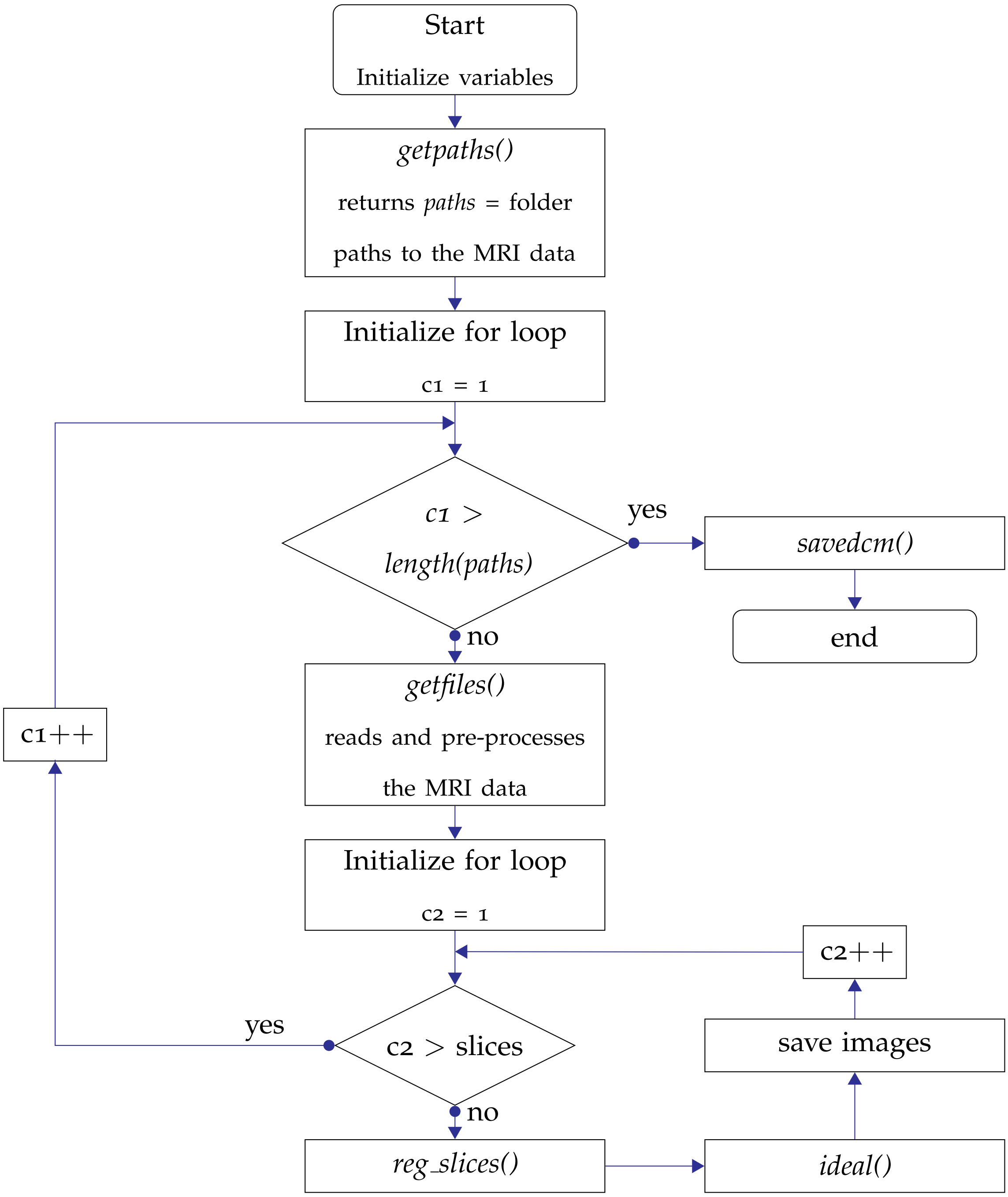

Figure 2.3.: Flowchart illustration the MATLAB script that calls the IDEAL-algorithm

2.3. Size Determination

2.3.1. Segmentation

After the decompensation the test subject P33 was excluded from further analysis, as too few data points remained (see table B.2). The water image was chosen for segmentation due to the hyper-intense appearance of the haematoma. The haematoma was manually outlined using the software ITK-SNAP (see figure 2.4). This rough segmentation was exported as a $*$.mha file and then imported into MATLAB by the function $import\_seg()$. The function *import_seg* uses functions of the file exchange package Read Medical Data 3D [19] to import the $*$.mha files correctly.

A refined segmentation was accomplished by first multiplying the water image with the ITK-SNAP mask and then applying the MATLAB function $multithresh()$. This function was applied instead of the more obvious function $graythresh()$, because the thresholds calculated by $multithresh()$ are in the same range as the input image. This is unlike $graythresh()$, which returns a normalized threshold in the range 0 to 1 [20]. The result of the segmentation was binarized. The pixel size of each haematoma was determined by the calculation of the summation of the final segmentation map. The average size over all three slices was determined for each session.

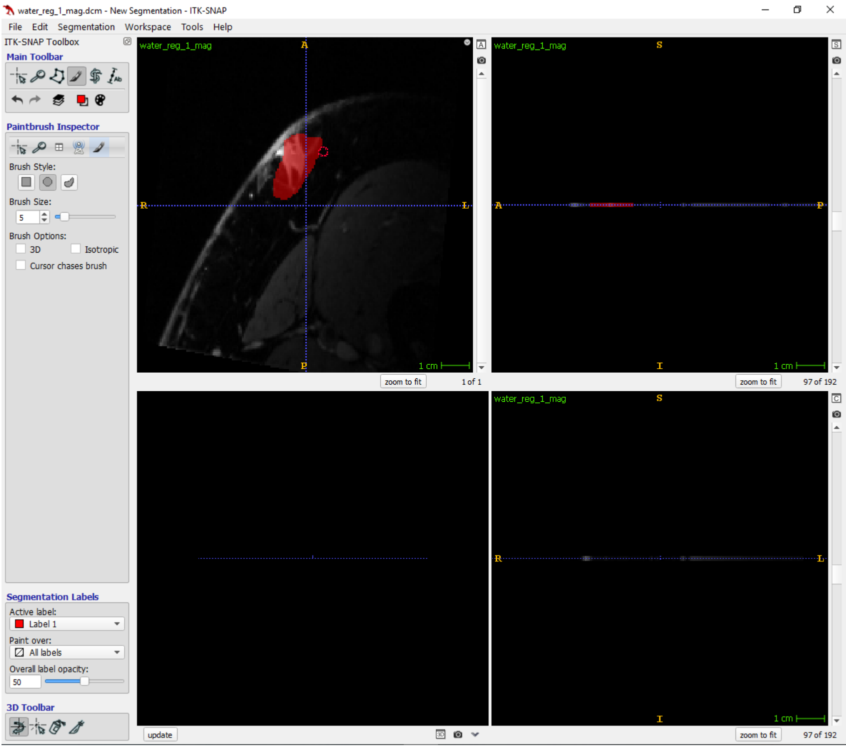

Figure 2.4.: Screenshot of the software ITK-SNAP, which was used to roughly segmenting the hyper-intense haematoma from its surround

2.3.2. Regression Analysis

Initially, one linear regression analysis [21] and an exponential regression analysis were performed on all the included data points. The linear regression analysis was implemented via a simple MATLAB script. For the exponential regression analysis the MATLAB function $fitnlm()$ was used. The performed regression models were:

$$\begin{aligned} f_{linear}(t) &= st + m \\ f_{exponential}(t) &= ab^t \end{aligned} \tag{2.19}$$

After calculating the normal and the adjusted coefficient of determination R^2 and R^2_{adj} of each model [22], the nonlinear regression model was deemed suitable to be applied to each test subjects' data individually.

To facilitate the comparisons between the test subjects, the included data points were normalized between 0 and 1. Having done that the model was applied to each test subject individually.

2.4. Water Fraction

2.4.1. Segmentation

The calculated water and fat images were merged, as described in equation 2.20, to obtain the water and fat fraction images.

$$\text{Water Fraction} = \frac{\text{Water}}{\text{Water} + \text{Fat}}$$
$$\text{Fat Fraction} = \frac{\text{Fat}}{\text{Water} + \text{Fat}} \tag{2.20}$$

The binary mask obtained during the size determination was used to set every pixel value of each fraction image outside the determined haematoma area to zero. Thereafter, the image matrix was summed up and divided by the haematoma's size to calculate the mean. This is used as the mean fraction value for the haematoma at each slice and time point.

A local minima entrapment during the decomposition can lead to a correct estimation whether the dominant species is water or fat, however the correct ratio between these two is only estimated if the global minima is found. Images that were presumed to be the result of a local minima were excluded. Decomposed images that featured areas of strong hyper-intensity and images that introduced a point of strong inflexion into the water fraction trend were assumed to be caused by a false ratio (see figure 2.5).

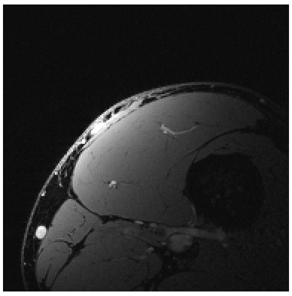

(a) Water image with strong hyper-intensity

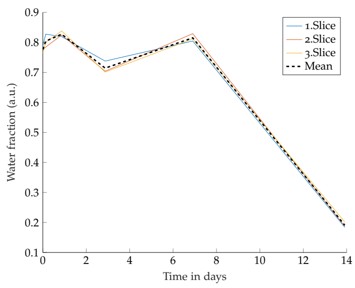

(b) Water fraction trend with point of strong inflexion

Figure 2.5.: Water image and mean water fraction trend due to local minima

2.4.2. Regression Analysis

Only the water fraction was used for further regression analysis. Two different regression models were tried first for all data points (see equations 2.21).

$$\begin{aligned} f_{linear}(t) &= st + m \\ f_{exponential}(t) &= ab^t \end{aligned} \tag{2.21}$$

As with the regression models for the haematoma's size the best regression model was determined and then applied to all test subjects. No normalization was necessary.

3. Results

3.1. Fat-Water Separation

The IDEAL-algorithm decomposed 98 of the 189 MRI data sets with the proposed default value $\psi_0 = 0$ for the initial field map. Figure 3.1 shows one of the resulting fat and water images and the corresponding field map and one of the source images.

As mentioned in section 2.2.2 the implemented IDEAL-algorithm can become entrapped in a local minima. Figures 3.2 and 3.3 displays the water image and the corresponding field map with different initial guesses for ψ_0. Figures 3.4a and 3.4c illustrate the results due to local minima entrapment and **??** and 3.4d the the results with a newly chosen guess for the initial field map.

Adapting the initial guess for ψ_0 lead to successful decomposition in 60 of the previous 91 imperfect separated images. Any further calculations were preformed with the 158 of 189 images where separation was possible.

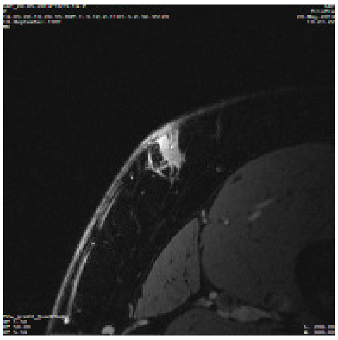

(a) water image

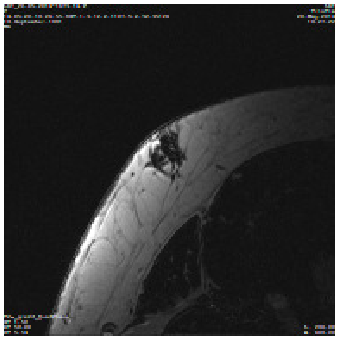

(b) fat image

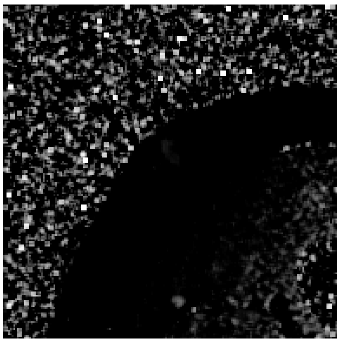

(c) Field map

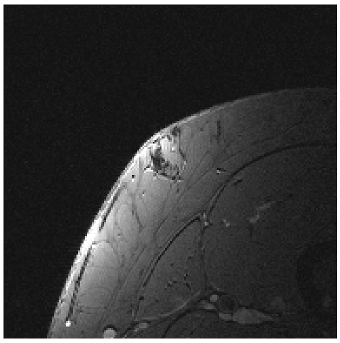

(d) Source image at quadrature

Figure 3.1.: Results of the IDEAL-algorithm

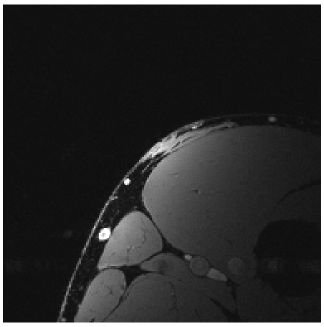

(a) $\psi_0 = -1$

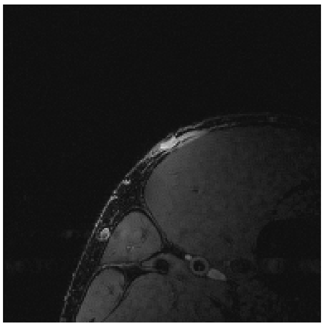

(b) $\psi_0 = -0.8$

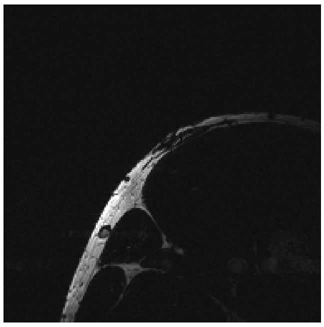

(c) $\psi_0 = -0.6$

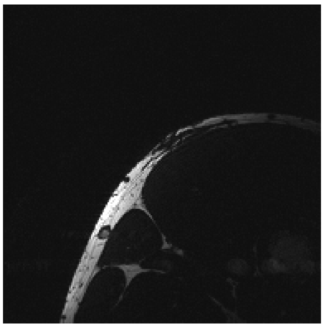

(d) $\psi_0 = -0.4$

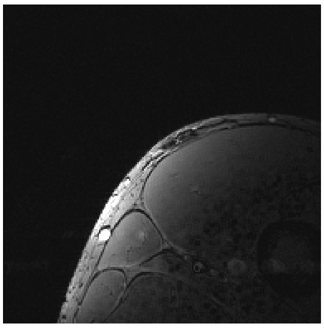

(e) $\psi_0 = -0.2$

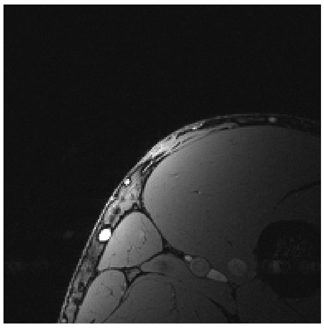

(f) $\psi_0 = 0$

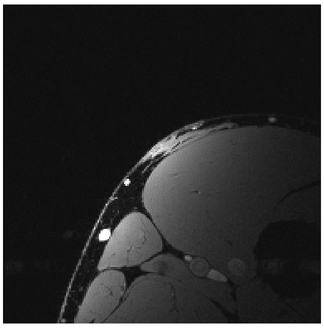

(g) $\psi_0 = 0.2$

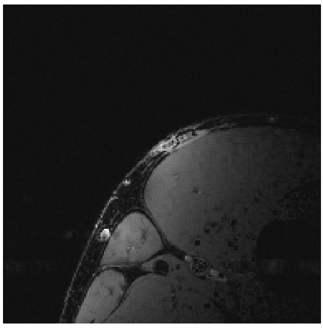

(h) $\psi_0 = 0.4$

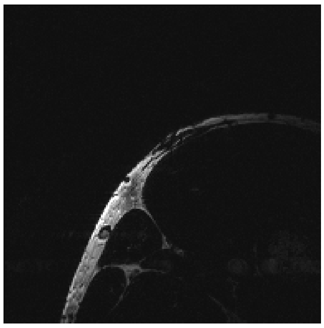

(i) $\psi_0 = 0.6$

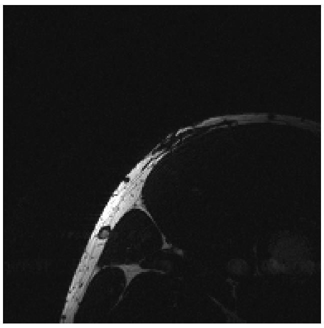

(j) $\psi_0 = 0.8$

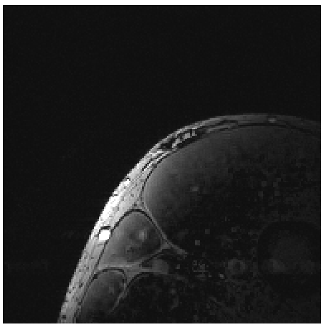

(k) $\psi_0 = 1$

Figure 3.2.: Water-only image as the result of different initial ψ_0's

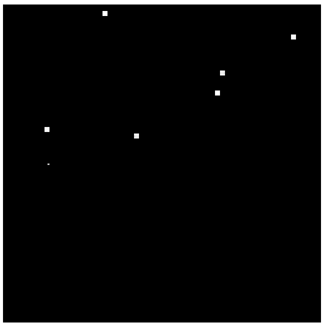

(a) $\psi_0 = -1$

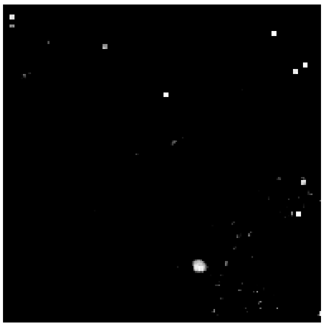

(b) $\psi_0 = -0.8$

(c) $\psi_0 = -0.6$

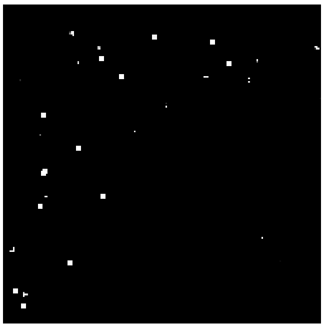

(d) $\psi_0 = -0.4$

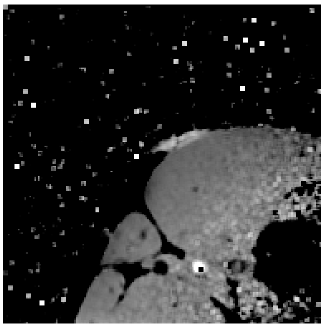

(e) $\psi_0 = -0.2$

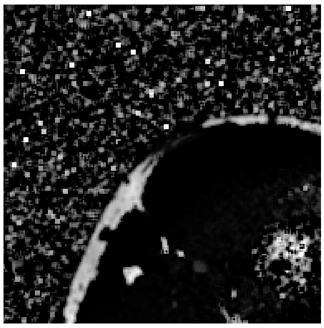

(f) $\psi_0 = 0$

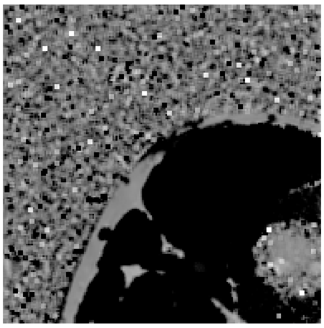

(g) $\psi_0 = 0.2$

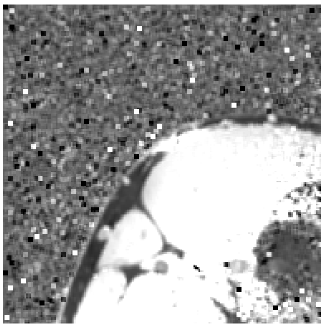

(h) $\psi_0 = 0.4$

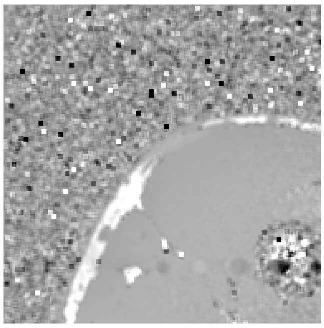

(i) $\psi_0 = 0.6$

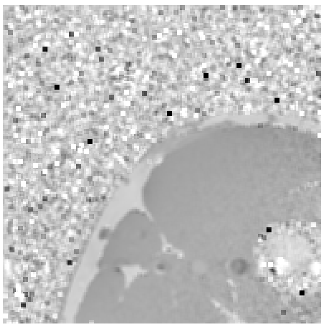

(j) $\psi_0 = 0.8$

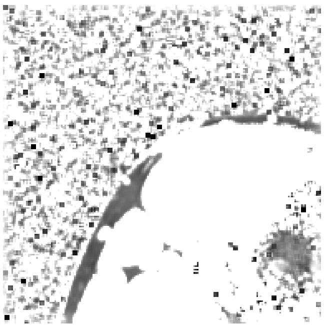

(k) $\psi_0 = 1$

Figure 3.3.: Field maps as the result of different initial ψ_0's

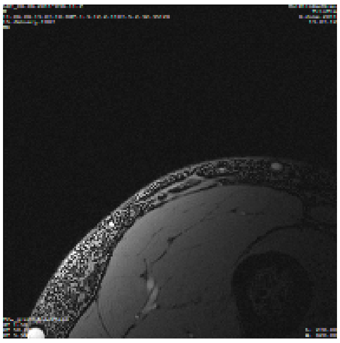

(a) water image $\psi_0 = 0$

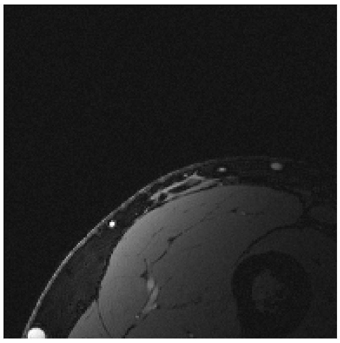

(b) water image $\psi_0 = 0.2$

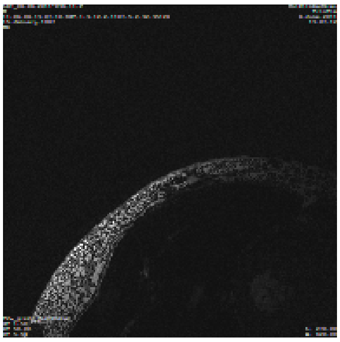

(c) fat image $\psi_0 = 0$

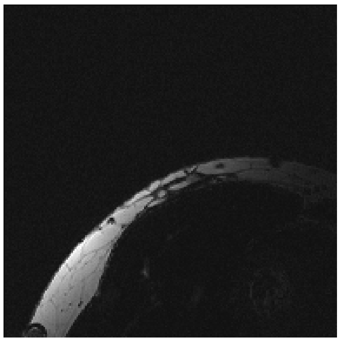

(d) fat image $\psi_0 = 0.2$

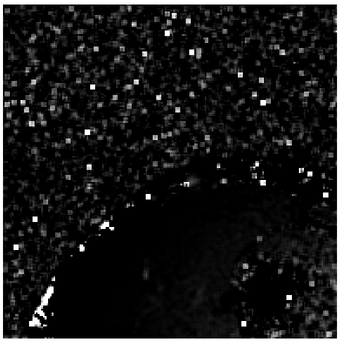

(e) field map $\psi_0 = 0$

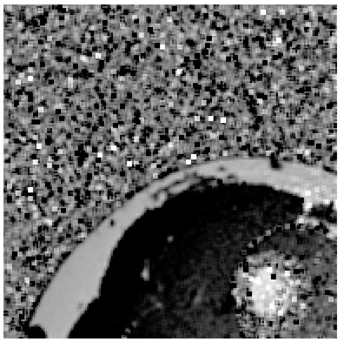

(f) field map $\psi_0 = 0.2$

Figure 3.4.: Incorrect (right) and correct (left) decomposition of IDEAL-algorithm. **(a) - (b)** water images **(c) - (d)** fat images **(e) - (f)** final field maps

The calculated field maps varied between the individual scans, as can be observed in figure 3.5.

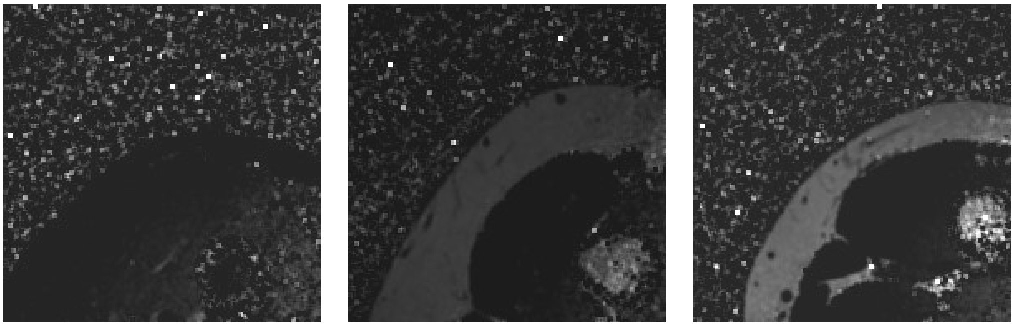

(a) Field map of the 2. slice of test subject P6's third session

(b) Field map of the 1. slice of test subject P31's fifth session

(c) Field map of the 3. slice of test subject P7's sixth session

Figure 3.5.: Different calculated field maps of several test subjects.

If the assumptions made in chapter 1.2.1 are correct, recombining the fat and water images (see equation 3.1 and figure 3.6a) should theoretically yield the original image at quadrature (see figure 3.6b). In praxis the recombination differs from the original image due to inhomogeneities other than ΔB_0, however it is still a valid comparison.

$$
\begin{aligned}
S_2 &= |W| + i|F| \\
|S_2| &= ||W| + i|F||
\end{aligned}
\tag{3.1}
$$

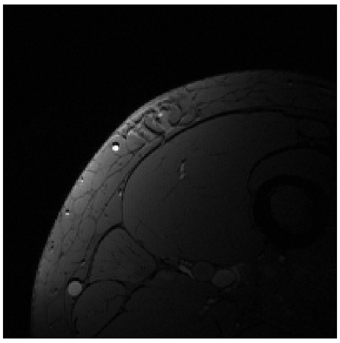

(a) recombined image

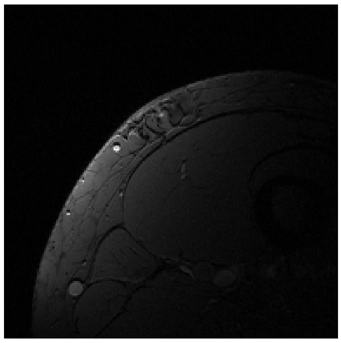

(b) original image at quadrature

Figure 3.6.: Illustration of the merged and original MRI image

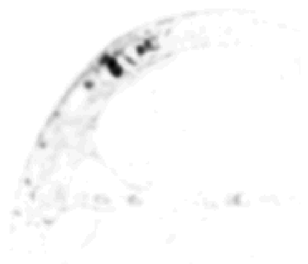

Figure 3.7.: SSIM map

For the assessment of the image quality of the decomposed images the root mean squared error (RMSE), the mean structural similarity (MSSIM) and the Peak Signal to Noise Ratio (PSNR) were calculated for all images and the mean, standard deviation (SD) and coefficient of variation (CV) were determined (see table 3.1). Figure 3.7 shows the MSSIM map of the images 3.6a and 3.6b. The map shows the highest dissimilarities around the haematoma and in regions of fatty tissues.

Of all three quality metrics in table 3.1 MSSIM is most noteworthy. The MSSIM ranges from 0 to 1, where 1 is only possible if two identical images

Table 3.1.: Quality metrics

Measure	RMSE	MSSIM	PSNR
Mean	28.5218	0.9991	68.52 dB
SD	19.3363	0.0026	19.34 dB
CV	67.8%	0.26%	67.8 dB

Mean, standard deviation, coefficient of variation of RMSE, MSSIM and PSNR

are compared.

The IDEAL-algorithm was mainly calculated in MATLAB, however the algorithm was also implemented in Java and Python for comparison. The average execution times per MRI slices are listed in table 3.2 and execution time for different amount of MRI images are displayed in figure 3.8. For further analysis of the three implementations look at appendix chapter A.

Table 3.2.: Mean and standard deviation of the over all execution times per MRI slice

Matlab		Python		Java	
Mean	SD	Mean	SD	Mean	SD
3.0529 s	0.0899 s	6.6965 s	0.4843 s	0.5286 s	0.0789 s

Mean and standard deviation of the over all execution times per MRI slices for all 3 implementations of the IDEAL-algorithm

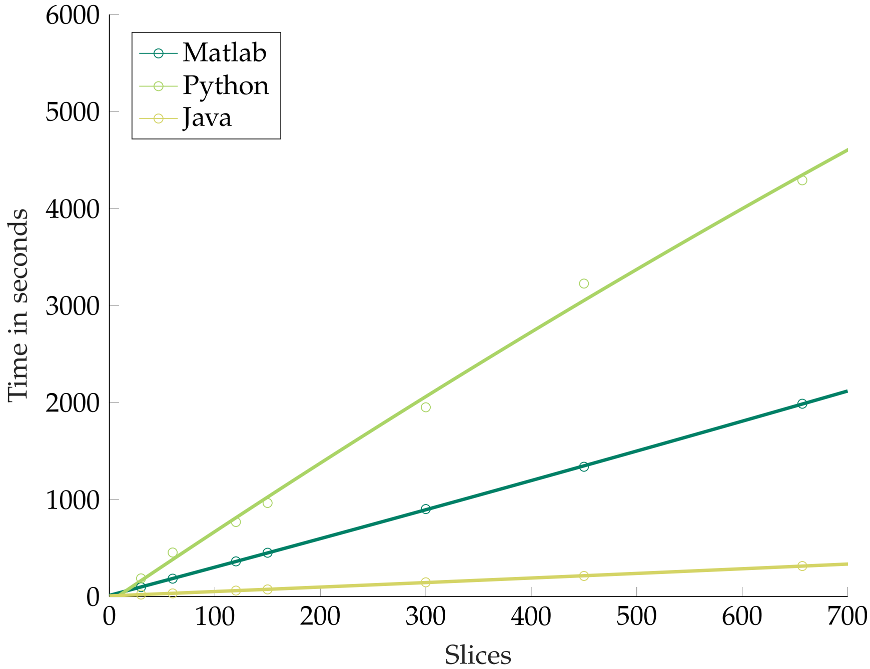

Figure 3.8.: Execution time of Matlab, Java and Python implementation.

3.2. Size Determination

3.2.1. Segmentation

Figure 3.9 shows the water image at several stages of the chain process to obtain the haematoma's sizes. The manual segmentation (see figure 3.9 (b)), refined segmentation (see figure 3.9 (c)) and binarization (see figure 3.9 (d)) are done for all three slices individually. After obtaining the size trend for all three slices, the mean at the desired time points is calculated (see figure 3.9 (e)).

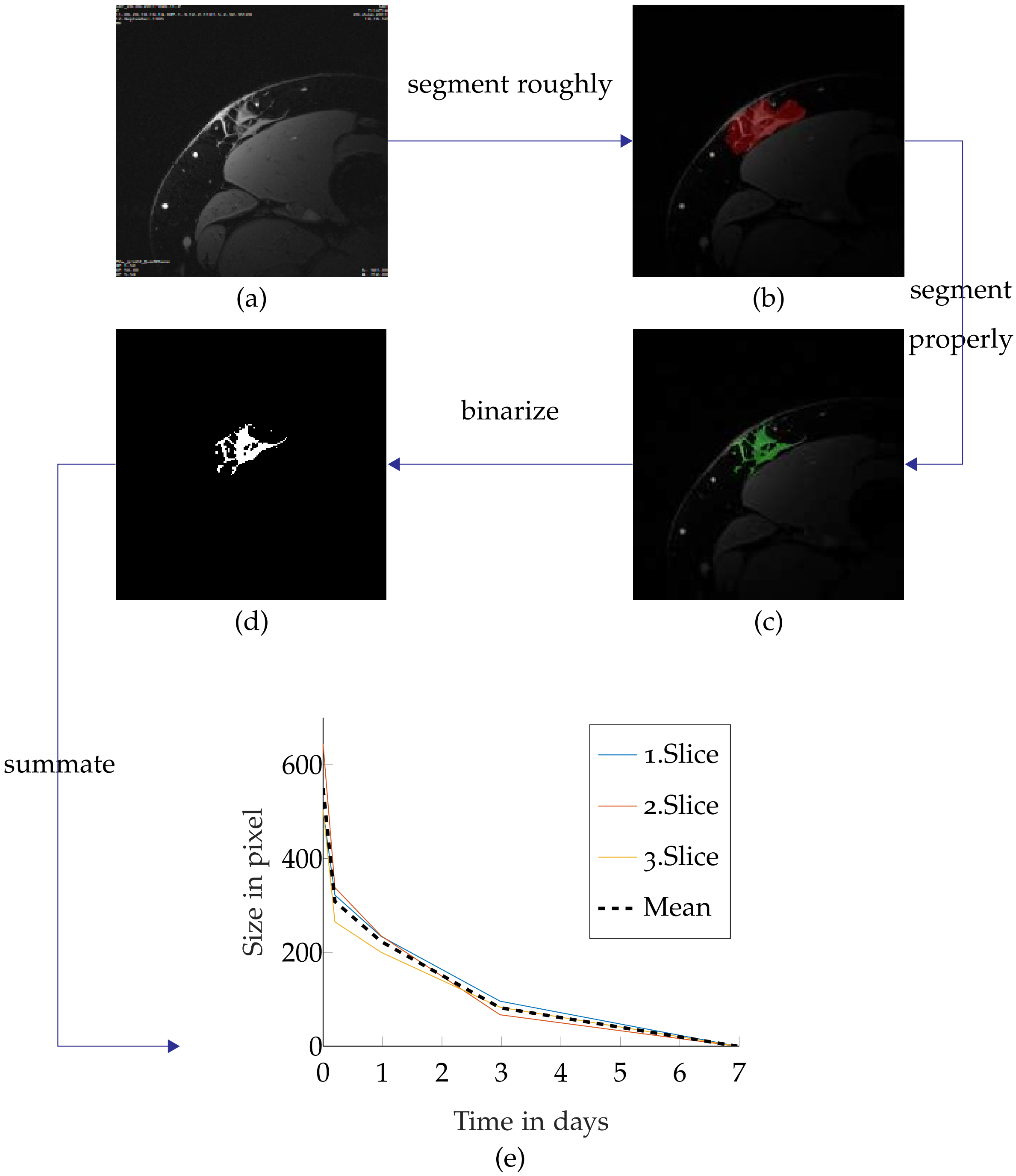

Figure 3.9.: Process to obtain haematoma's size. **(a)** Calculated water MRI images. **(b)** MRI image with rough segmentation of ITK-Snap overlaid. **(c)** MRI images with final segmentation map overlaid. **(d)** Binarized image with haematoma area in white. **(e)** Haematoma's sizes of all three slices and the average over time for one test subject.

All obtained mean sizes from figure 3.9 (e) for every test person are displayed in figure 3.10. The size trend illustrates the disappearance of the haematoma for most test subjects after one or two weeks (marked as red circles). The test subjects P21 and P32 show differing behaviour.

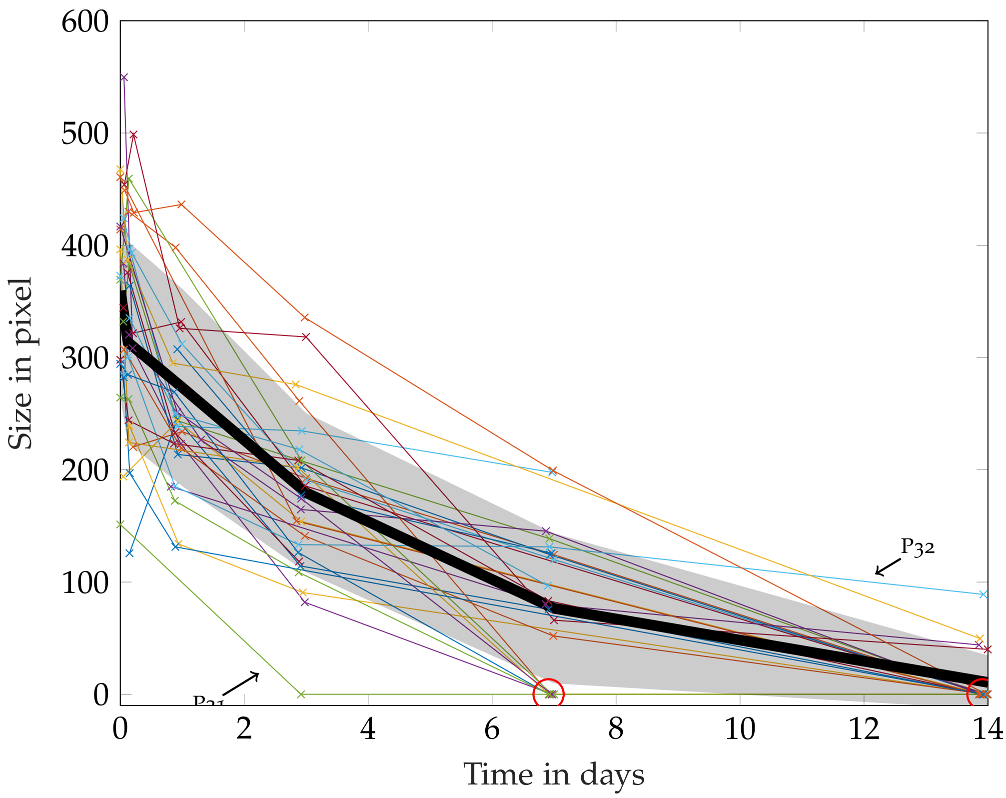

Figure 3.10.: Absolute haematoma mean size over time for all test subjects with mean (black solid line) and corresponding SD (shaded area). The haematoma disappeared for most test subjects after one or two weeks (see red circles). The size trend for test subjects P21 and P32 appear to differ.

Figure 3.11 displays the results of figure 3.10 with each test subject's sizes individually normalized between 0 and 1. The relative size graph illustrates that the haematoma's size maxima occurred as late as 1 day after injection (see blue circles). If the test subject shows differing behaviour in the absolute size graph, it shows this behaviour in the relative size graph too. The normalization revealed the additional differing behaviour of test subject P30. Test subject P13 experiences the steepest decline.

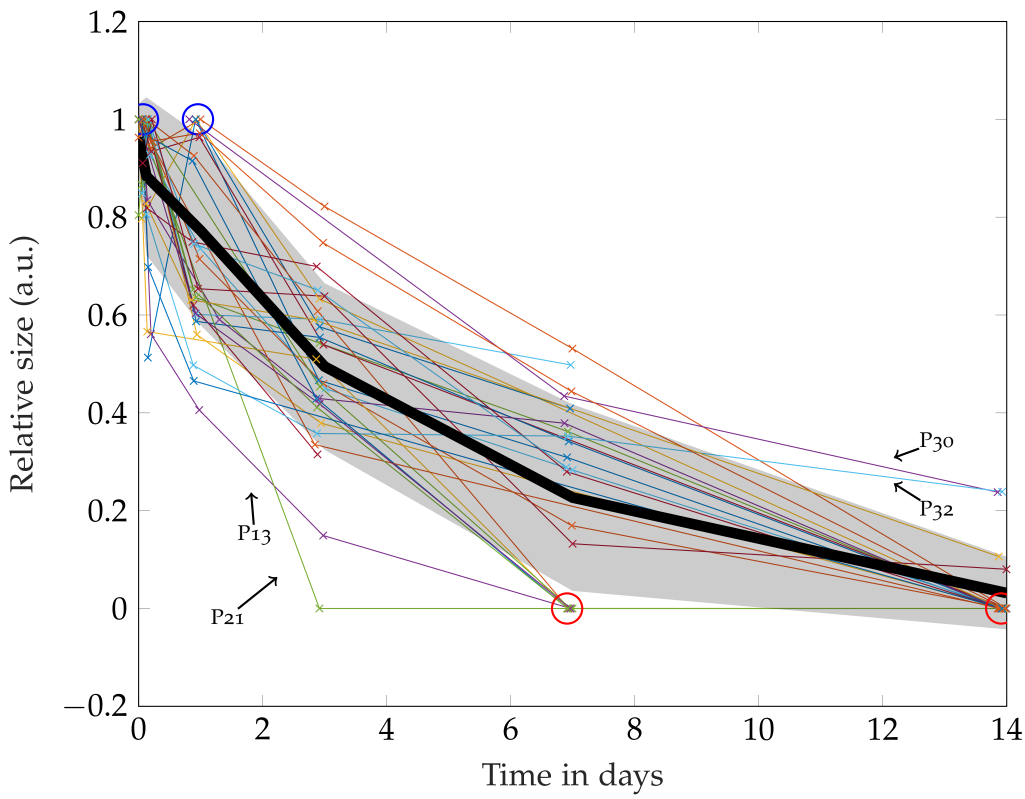

Figure 3.11.: Relative haematoma mean size over time for all test subjects with mean (black solid line) and corresponding SD (shaded area). The haematoma disappeared for most test subjects after one or two weeks (see red circles). The haematoma's size maxima cluster directly after injection and one day after injection (see blue circles). The size trend for test subjects P21, P32 and P30 appear to differ. Test subject P13 shows the steepest decline.

The mean, standard deviation and coefficient of variation of the haematoma sizes at selected time points are listed in table 3.3. The coefficients of variation increase over time.

Table 3.3.: Mean, standard deviation and coefficient of variation of haematoma's sizes

	absolute Size			relative Size		
Time point	Mean	SD	CV	Mean	SD	CV
0 hours	359.5303	95.3201	26.51 %	0.9632	0.069	7.16 %
3 hours	313.5294	90.0364	28.72 %	0.8839	0.1613	18.25 %
1 day	273.3226	87.9468	32.18 %	0.7727	0.1938	25.08 %
3 days	179.5402	70.918	39.5 %	0.4947	0.1704	34.45 %
1 week	76.55072	66.8314	87.3 %	0.2266	0.1907	84.14 %
2 weeks	10.60317	24.0445	226.77 %	0.0316	0.0743	235.28 %

Mean, standard deviation and Coefficient of Variation of the absolute and relative haematoma's sizes at selected time points.

3.2.2. Regression Analysis

The visual representation of the preliminary tested regression models is illustrated in figure 3.12. The specific values of the preliminary tested linear and exponential regression models (table 3.4) confirm the assumption that the exponential regression model approximates the area decline of the haematoma more accurately.
As both regression models were applied to the same size of data samples, the normal coefficient of determination R^2 obtained sufficed to choose the exponential regression model for further analysis.

For better comparison between all test subjects the exponential regression model was applied to the normalized data set of haematoma sizes (see figure 3.11). This boosted the regression model, as is shown by comparing the coefficients of determination in table 3.5 to the values of table 3.4.

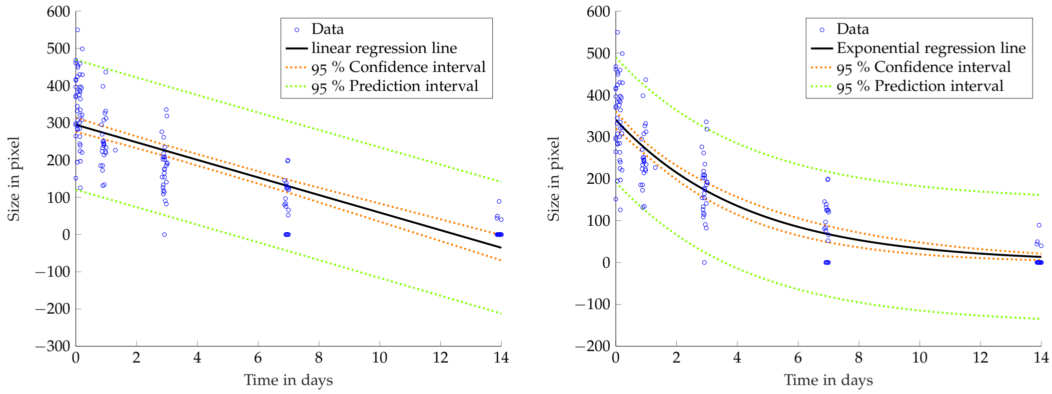

(a) Linear regression (b) Exponential regression

Figure 3.12.: Preliminary regression models

Table 3.4.: Preliminary regression model values

	linear model	exponential model
R^2	0.628	0.725
R^2_{adj}	0.626	0.723
RMSE	86.9	74.7
p-value	$4.2 \cdot 10^{-32}$	$2.58 \cdot 10^{-74}$

Normal and adjusted coefficient of determination (R^2, R^2_{adj}), root mean squared error (RMSE) and pvalue for the preliminary regression models.

Table 3.5.: Exponential regression model values for a normalized data set

	normalized exponential model
R^2	0.821
R^2_{adj}	0.82
RMSE	0.154
p-value	$4.55 \cdot 10^{-91}$

Normal and adjusted coefficient of determination (R^2, R^2_{adj}), root mean squared error (RMSE) and pvalue for the normalized data set.

The normalized exponential regression model is shown in figure 3.13.

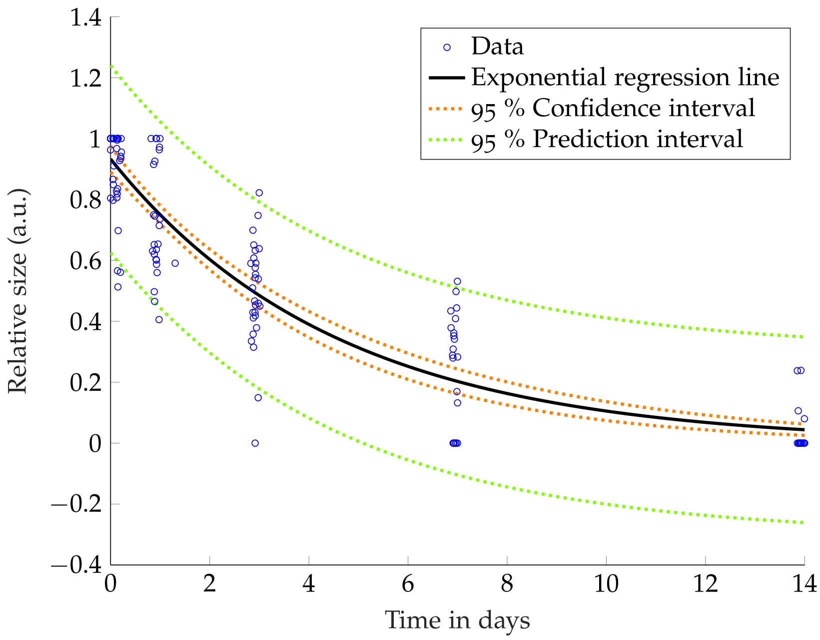

Figure 3.13.: Normalized regression model

Finally, the chosen regression model was applied to each test subject individually. Figure 3.14 displays the regression model of one test subject. For the regression models of all test subject see appendix chapter C.2.

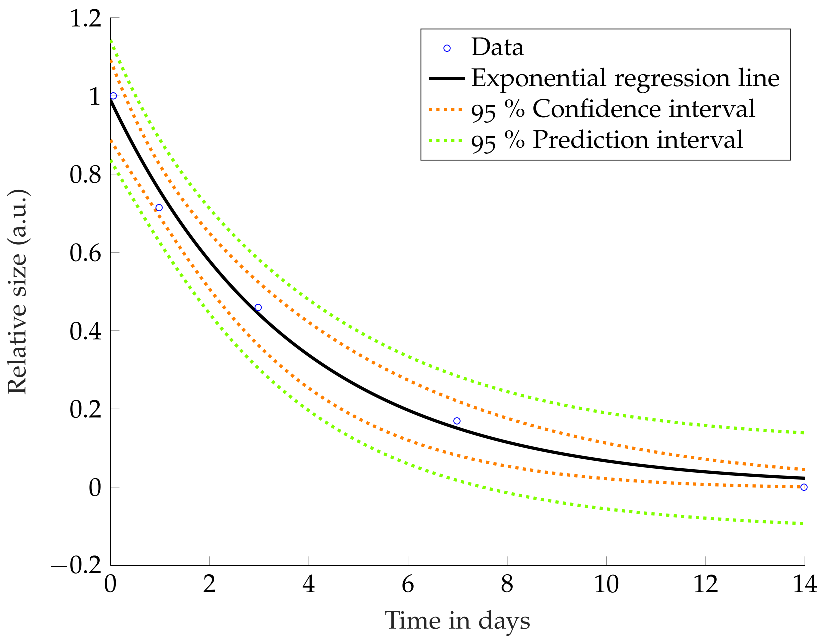

Figure 3.14.: Exponential regression model of test person P18

Upon analysing the regression models for each test subject, one was excluded. This exclusion was necessary because only one MRI scan showed a haematoma of any kind and therefore too few data points remained for a meaningful regression analysis (see figure 3.15).

The values for the coefficients of the exponential regression line all reside in the same range, except for P10, P23, P29 and P32 in the case of coefficient a. Notable exceptions for coefficient b are P8 and P13. (see figure 3.16).

The normal and adjusted coefficients of determination are valuable metrics to determine the relevance of the regression model. The bar char 3.17 shows

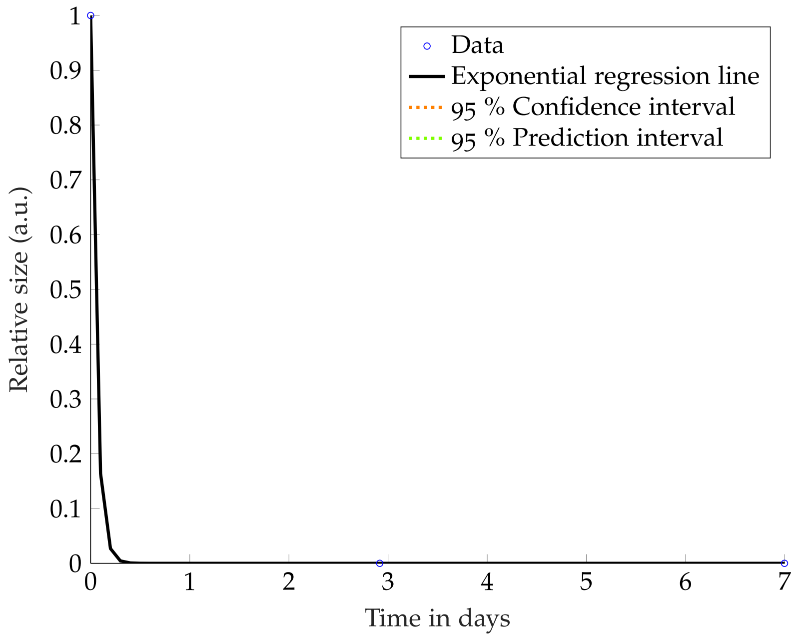

Figure 3.15.: Exponential regression model of excluded test person P21

these values for each test subject. Test subjects P10, P23 and P32 stand out with low coefficients of determination.

Figure 3.18 shows the p-values of the coefficients presented in figure 3.16. For coefficient a only P8, P24 and P27 exceeds a p-value of 0.05. The p-value of coefficient b is exceeding 0.05 for several test subjects (P8, P13, P24).

The bar chart in figure 3.19 depicts the p-values of the regression models for each test subject. P24 and P27 have a p-value higher then 0.05.

The means, standard deviations and coefficients of variation over all regression models for both regression parameters a and b are listed in table 3.6.

Table 3.7 shows the mean, standard deviation and coefficient of variation for the quality metrics of the regression models.

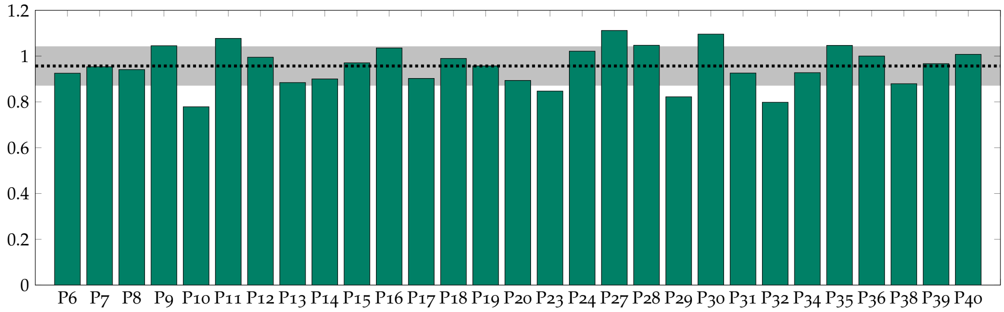

(a) Bar chart for coefficient *a*, with the mean plotted as a dotted black line and the standard deviation as shaded area.

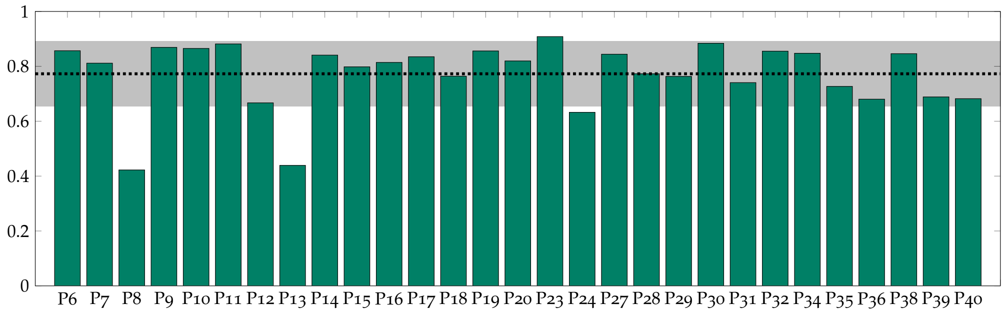

(b) Bar chart for coefficient *b*, with the mean plotted as a dotted black line and the standard deviation as shaded area.

Figure 3.16.: Bar charts for regression model coefficients

Table 3.6.: Values (mean, SD, CV) for the nonlinear model's coefficients and its parameters

	Coefficient a			Coefficient b		
	Mean	SD	CV	Mean	SD	CV
Estimate	0.9568	0.0868	9.07 %	0.7728	0.1201	15.54 %
SE	0.1241	-	-	0.0573	-	-
p-value	0.0211	-	-	0.0126	-	-

Mean, standard deviation and the coefficient of variation for the estimates of coefficients and the mean for standard error (SE) and p-value for the exponential regression models of each test subject.

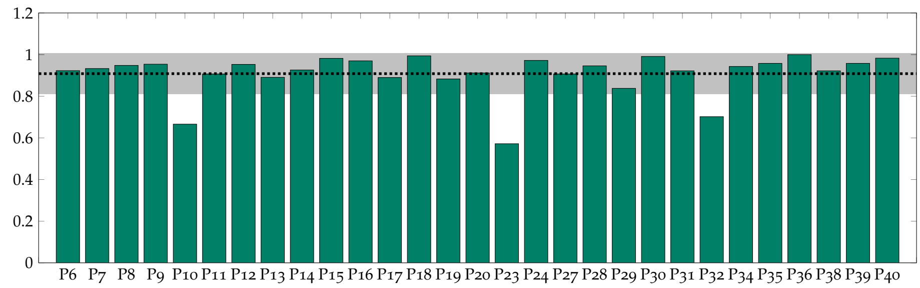

(a) Bar chart for R^2, with the mean plotted as a dotted black line and the standard deviation as shaded area.

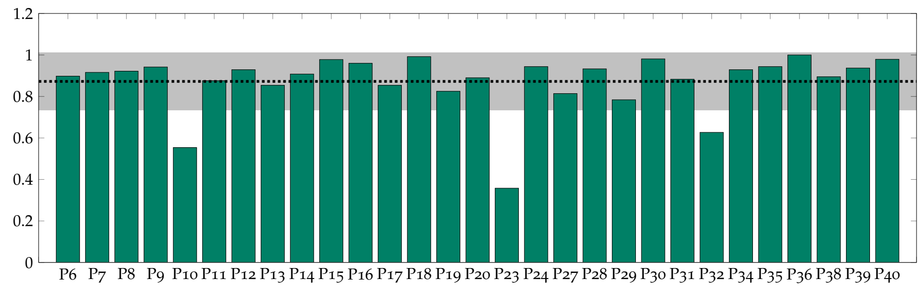

(b) Bar chart for R^2_{adj}, with the mean plotted as a dotted black line and the standard deviation as shaded area.

Figure 3.17.: Bar charts for the normal and adjusted Coefficient of determination

Table 3.7.: Values (mean, SD, CV) of the nonlinear model for each test subject

	Mean	SD	CV
R^2	0.9085	0.0994	10.94 %
R^2_{adj}	0.8726	0.1401	16.05 %
RMSE	0.1161	0.0507	43.66 %
p-value	0.0155	-	-

Mean, standard deviation and coefficient of variation for the normal and adjusted coefficient of confidence (R^2, R^2_{adj}) and Root mean square error(RMSE) and the mean of the p-value for the exponential regression model of each test subject.

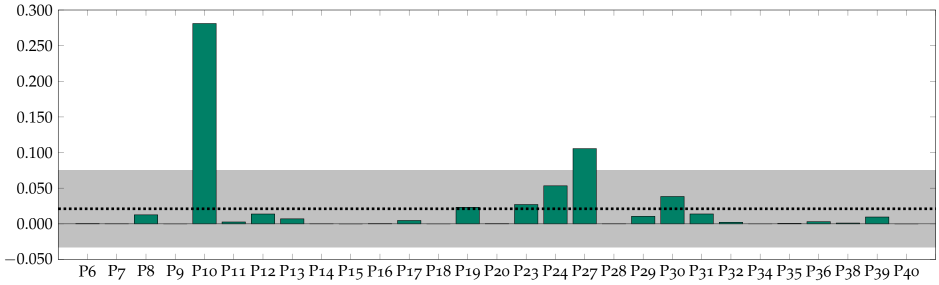

(a) Bar chart for p-value of coefficient *a*, with the mean plotted as a dotted black line and the standard deviation as shaded area.

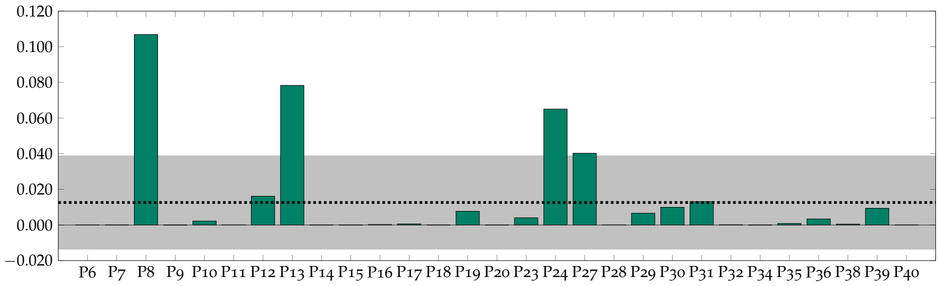

(b) Bar chart for p-value of coefficient b, with the mean plotted as a dotted black line and the standard deviation as shaded area.

Figure 3.18.: Bar charts for the p-values of the coefficients of the regression models

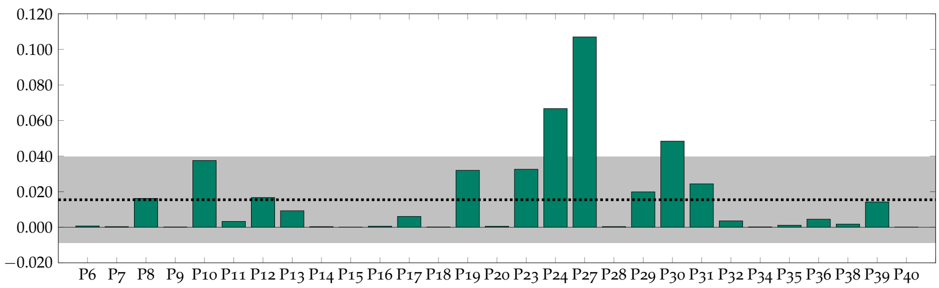

Figure 3.19.: Bar chart for pvalue of the regression models, with the mean plotted as a dotted black line and the standard deviation as shaded area.

Figure 3.20a is the boxplot for the coefficients of the regression line and the normal and adjusted coefficients of determination

The boxplot for the p-values of the coefficients of the regression line and the regression model is represented in figure 3.20b.

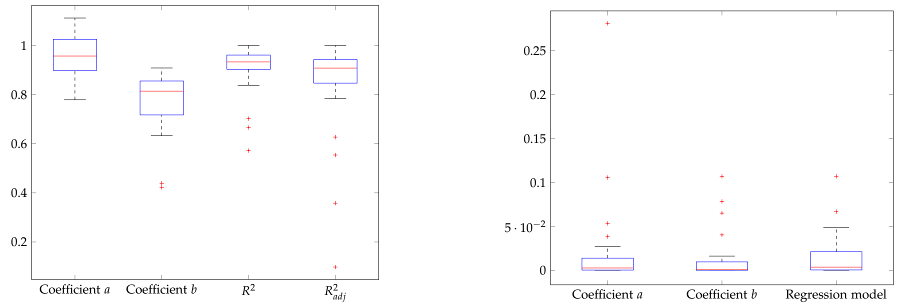

(a) Coefficients, R^2 and R^2_{adj}

(b) p-values

Figure 3.20.: Box plots for coefficients, R^2 and R^2_{adj} and p-values of the coefficients and the regression models

3.3. Water Fraction

3.3.1. Segmentation

Figure 3.21 depicts the process of obtaining the haematoma's water fraction.

All obtained mean water fractions from figure 3.21 (e) for every test subject are displayed in figure 3.22.

Some test subjects' water fractions differ significantly from the other. These test subjects are marked with an arrow. Upon closer inspection some data

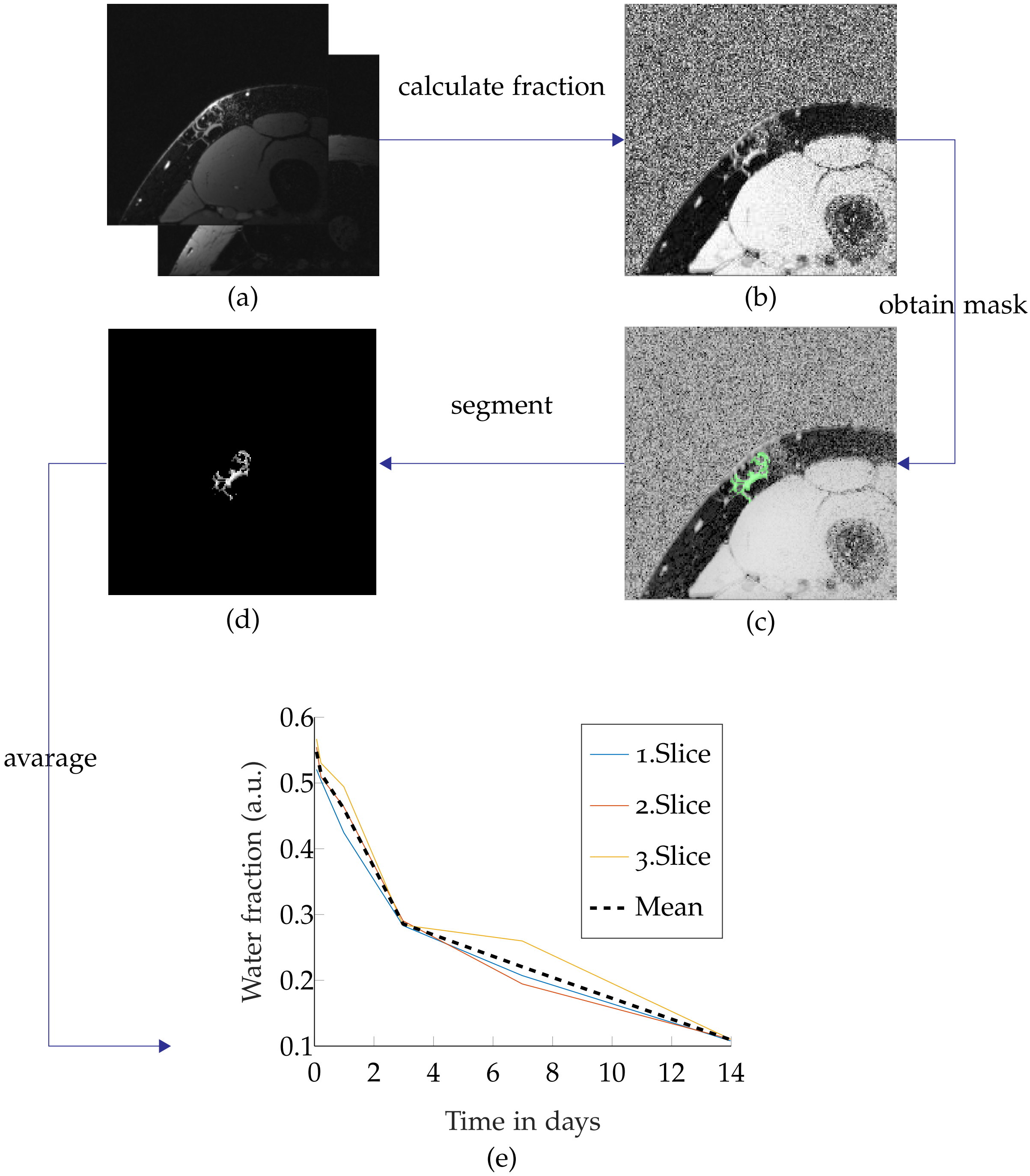

Figure 3.21.: Process to obtain haematoma's water fraction. **(a)** Calculated water and fat MRI images. **(b)** Water fraction image (Water / (Fat+Water)) **(c)** Water fraction image with final segmentation map from size determination in green overlaid. **(d)** Final images that will be used to calculate average. **(e)** Haematoma's water fraction of all three slices and the average over time for one test subject.

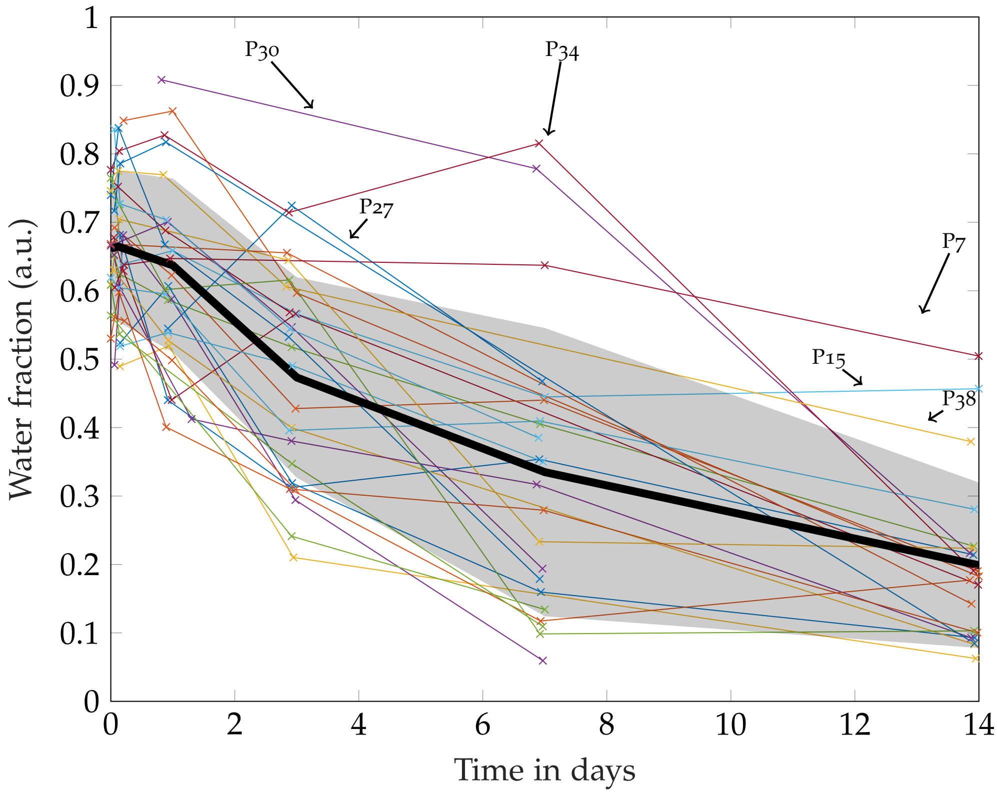

Figure 3.22.: Haematoma mean water fraction over time for all test subjects with mean (black solid line) and corresponding SD (shaded area). Test subjects that show differing behaviour are marked with an arrow.

points of some test subjects were excluded as an inaccuracy due to imperfect decomposition was suspected.
The test subject P7 was excluded, because the water fraction showed almost no variation over time. The data points for P34 (7 days), P27(3 days), P10(3 days), P11(14 days) and P15(14 days) were also excluded. Test subject P27 was then totally excluded, as too few data points remained. Test subject P30 was excluded too.

These exclusions are accounted in all following calculations and illustrations The water fraction without these outliers is presented in figure 3.23.

Figure 3.24 shows the fat ratio of all remaining test subjects.

The mean, standard deviation and coefficient of variation of the haematoma's water and fat fraction at selected time points are listed in table 3.8. The CV of the water fraction increases with time.

Table 3.8.: Mean, SD and CV of haematoma's water and fat fraction

	Water Fraction			Fat Fraction		
Time point	Mean	SD	CV	Mean	SD	CV
0 hours	0.6644	0.0878	13.22 %	0.3356	0.0878	26.17 %
3 hours	0.6644	0.1104	16.61 %	0.3356	0.1104	32.88 %
1 day	0.6374	0.1202	18.86 %	0.3626	0.1202	33.15 %
3 days	0.4639	0.1406	30.3 %	0.5361	0.1406	26.22 %
1 week	0.2594	0.1313	50.61 %	0.7406	0.1313	17.73 %
2 weeks	0.1666	0.0817	49.02 %	0.8334	0.0817	9.8 %

Mean, standard deviation(SD) and Coefficient of Variation(CV) of the haematoma's water and fat fraction at selected time points.

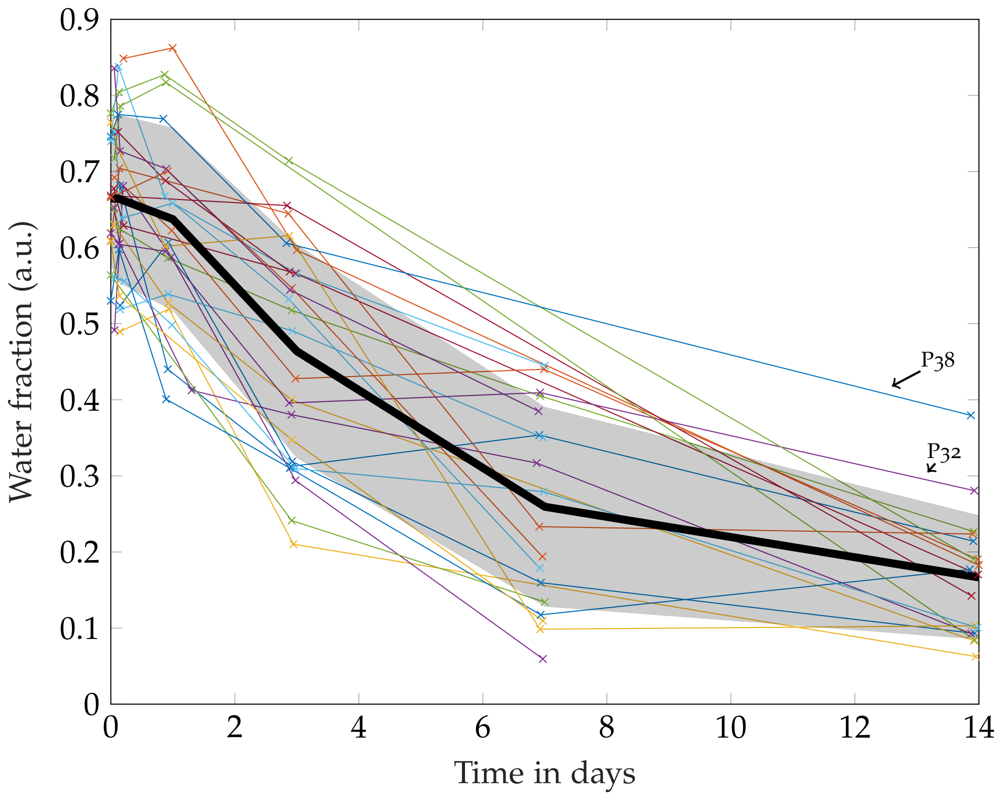

Figure 3.23.: Haematoma mean water fraction over time for test subjects with correct separation with mean (black solid line) and corresponding SD (shaded area).

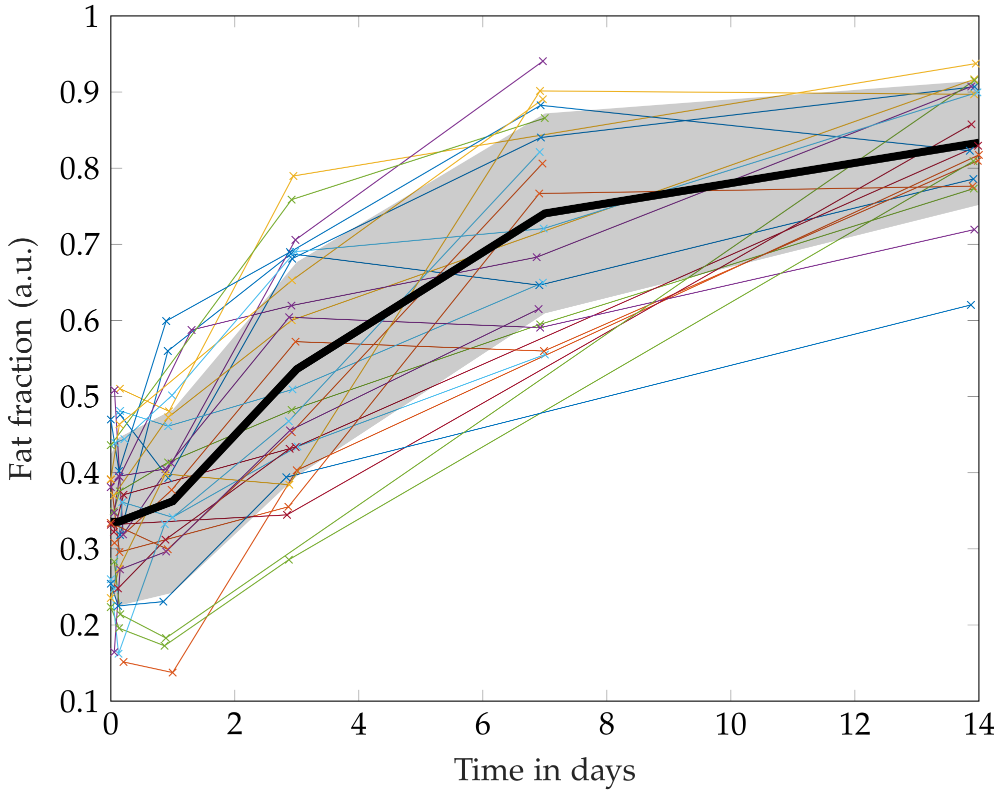

Figure 3.24.: Haematoma mean fat fraction over time for test subjects with correct separation mean (black solid line) and corresponding SD (shaded area).

3.3.2. Regression Analysis

The preliminary tested regression models are depicted in figure 3.25. Based on the specific values of the preliminary regression models (see table 3.9) the exponential regression model was selected as the best fitted model.

Table 3.9.: Preliminary regression model values

	linear model	exponential model
R^2	0.664	0.726
R^2_{adj}	0.661	0.723
RMSE	0.129	0.117
p-value	$2.25 \cdot 10^{-31}$	$6.7 \cdot 10^{-84}$

Normal and adjusted coefficient of determination (R^2, R^2_{adj}), root mean squared error (RMSE) and p-value for the preliminary regression models.

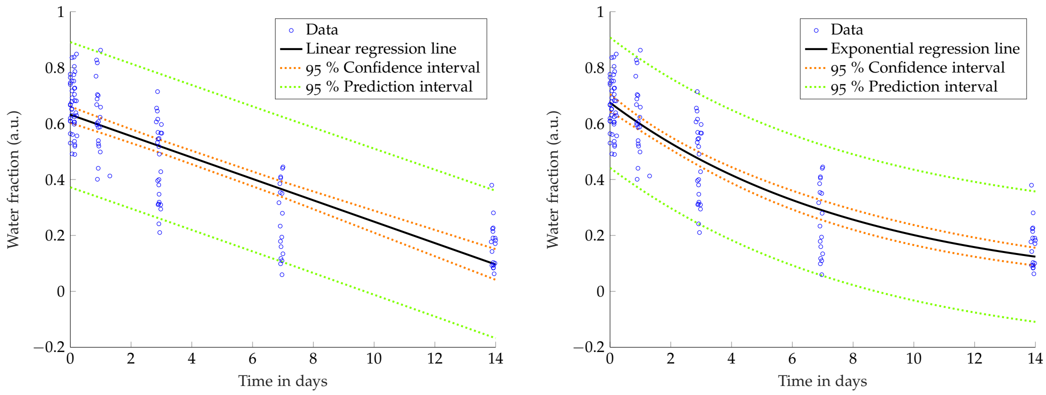

(a) Linear Regression

(b) Exponential Regression

Figure 3.25.: Preliminary Regression Models

At the end, the chosen exponential regression model was applied to each test subject individually. Figure 3.26 displays the regression model of one test subject. For the regression models of all test subjects see appendix chapter C.3.

The values of coefficient b of the exponential regression line all reside in the range of 0.7774 to 0.9484 and the values of coefficient a vary more significantly (see figure 3.27).

The bar char 3.28 shows normal and adjusted coefficient of determination for each test subject. Test subject P10 shows the lowest R^2 value.

Figure 3.29 displays the p-values of the coefficients.

The bar chart in figure 3.30 depicts the p-values of the regression models for each test subject. Only test subject P36 is outside the 95%-Confidence interval.

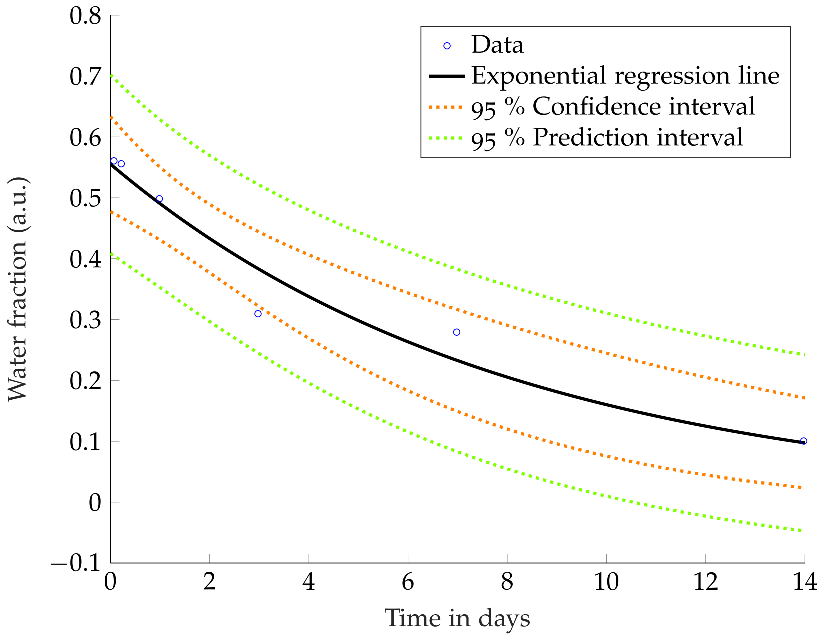

Figure 3.26.: Exponential regression model of test person P9

The means, standard deviations and coefficients of variation over all regression models for both regression parameters a and b are listed in table 3.10.

Table 3.10 shows the mean, standard deviation and coefficient of variation for the quality metrics of the regression models.

Figure 3.31a is the boxplot for the coefficients of the regression line and the normal and adjusted coefficients of determination

The boxplot for the p-values of the coefficients of the regression line and the regression model is shown in figure 3.31b.

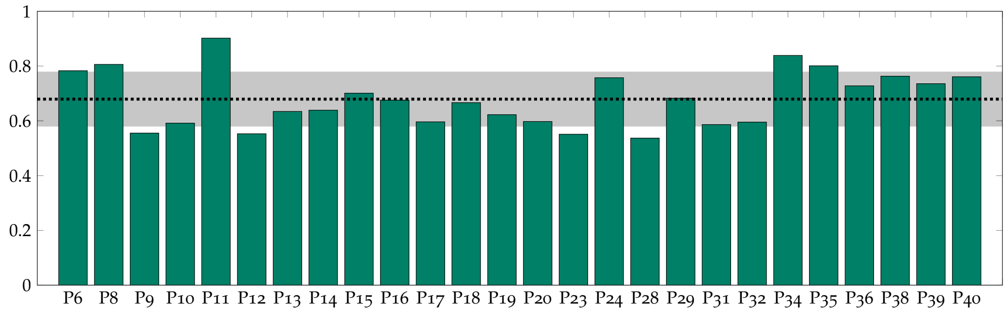

(a) Bar chart for coefficient a, with the mean plotted as a dotted black line and the standard deviation as shaded area.

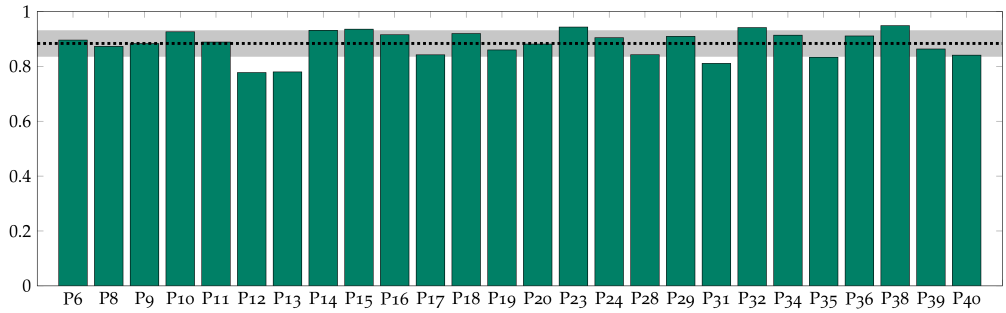

(b) Bar chart for coefficient b, with the mean plotted as a dotted black line and the standard deviation as shaded area.

Figure 3.27.: Bar charts for regression model coefficients

Table 3.10.: Values (mean, SD, CV) for the nonlinear model's coefficients and its parameters

	Coefficient a			Coefficient b		
	Mean	SD	CV	Mean	SD	CV
Estimate	0.6792	0.1009	14.85 %	0.8834	0.0487	5.55 %
SE	0.0467	-	-	0.0286	-	-
p-value	0.00686	-	-	0.0022	-	-

Mean, standard deviation and the coefficient of variation for the estimates of coefficients and the mean for standard error (SE) and p-value for the exponential regression models of each test subject.

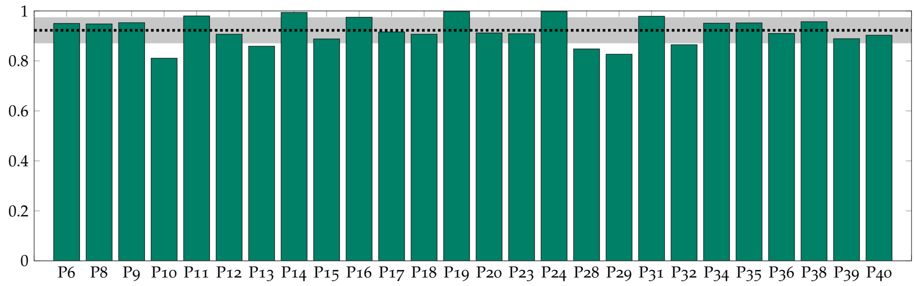

(a) Bar chart for R^2, with the mean plotted as a dotted black line and the standard deviation as shaded area.

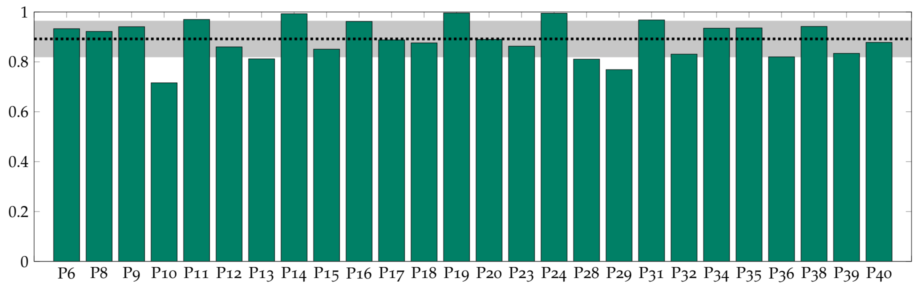

(b) Bar chart for R^2_{adj}, with the mean plotted as a dotted black line and the standard deviation as shaded area.

Figure 3.28.: Bar charts for the normal and adjusted coefficient of determination

Table 3.11.: Values (mean, SD, CV) of the nonlinear model for each test subject

	Mean	SD	CV
R^2	0.92254	0.05257	5.7 %
R^2_{adj}	0.892	0.0735	8.24 %
RMSE	0.06613	0.03405	51.49 %
p-value	0.00929	-	-

Mean, standard deviation and coefficient of variation
for the normal and adjusted coefficient of confidence (R^2, R^2_{adj})
and Root mean square error(RMSE) and the mean of the p-value
for the exponential regression model of each test subject.

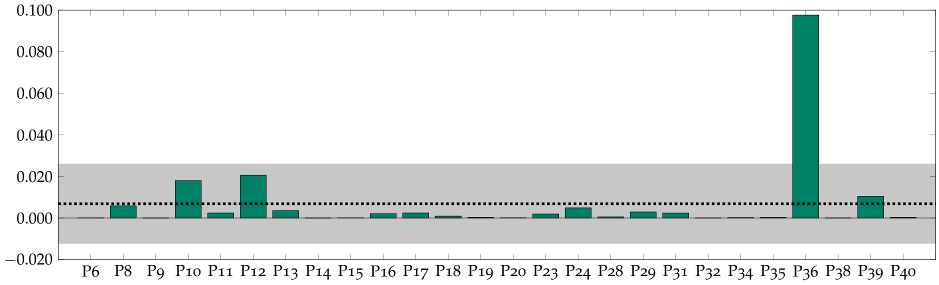

(a) Bar chart for p-value of coefficient *a*, with the mean plotted as a dotted black line and the standard deviation as shaded area.

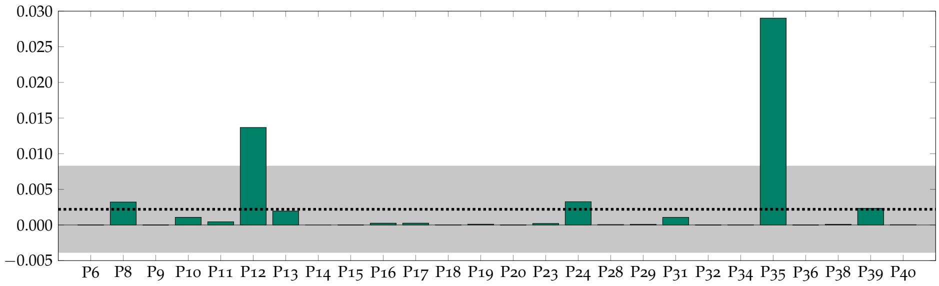

(b) Bar chart for p-value of coefficient *b*, with the mean plotted as a dotted black line and the standard deviation as shaded area.

Figure 3.29.: Bar charts for the p-values of the coefficients of the regression models

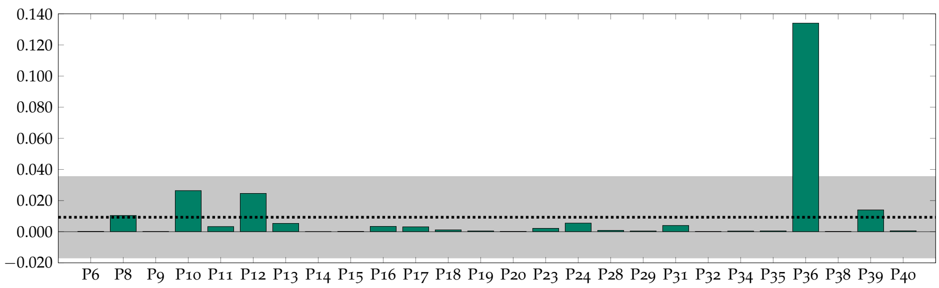

Figure 3.30.: Bar chart for p-value of the regression models, with the mean plotted as a dotted black line and the standard deviation as shaded area.

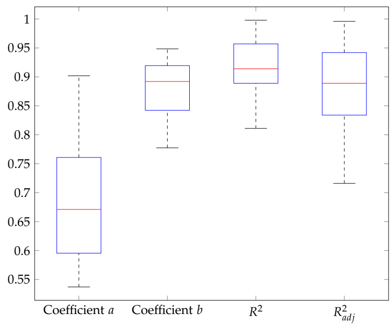

(a) Coefficients, R^2 and R^2_{adj}

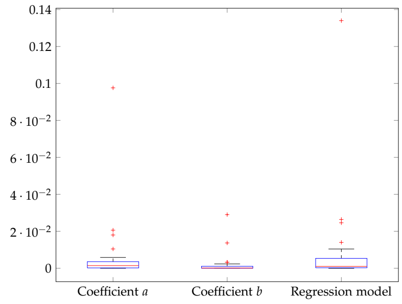

(b) P-values

Figure 3.31.: Box plots for coefficients, R^2 and R^2_{adj} and p-values of the coefficients and the regression models

4. Discussion

4.1. Fat-Water Separation

The thesis' goal of fat-water separation through the IDEAL-algorithm was successfully accomplished for most of the provided data sets. In these cases the algorithm presents itself as an effective method to decompose the fat and water parts of the MRI signal (see figure 3.1). The expandability of the computation to more than two species of different chemical shifts makes the method quite usable in various different manners. Even restricted to fat-water separation, the algorithm could be extended to accommodate more than one fat peak [1]. However, this expansion would require more images, which causes restrictions due to the prolonged acquisition time.

As shown in figure 3.4 and mentioned in chapter 2, the decomposition was not always successful. This is due to the limitation in the determination of the field map ψ. The field map estimation is a critical step in the decomposition process. However, the true field map can only be directly determined if it ranges between $\pm\Delta f_{cs}/2$ [15]. As exceeding this range is possible, some techniques use phase unwrapping to address this problem. The IDEAL method bypasses this by using an iterative field map estimation method. This iterative approach does not solve the intrinsic ambiguity as the iterative method has multiple exact solutions due to local minima (see figure 4.1).

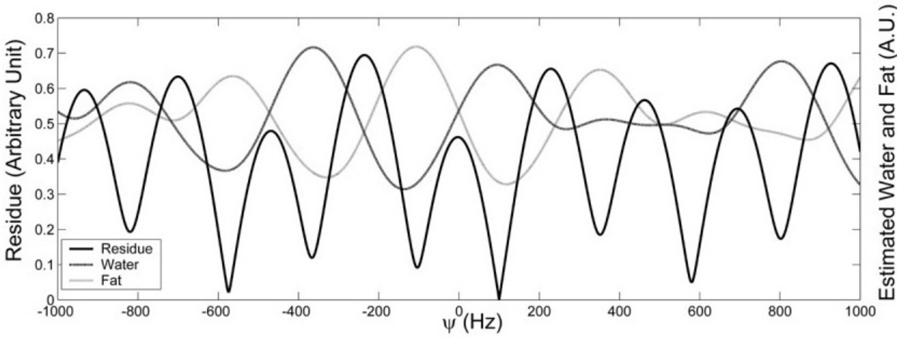

Figure 4.1.: Residue-ψ curve with a true water-fat ratio of 2:1. The overall residue of all signals is minimal at the true field map value (here $\psi_t = 100Hz$). The IDEAL-algorithm determines ψ by minimizing $\Delta\psi$, where $\Delta\psi$ is minimal if the residue over all signals is minimal. The Residue-ψ curve represents the dynamics of the estimated ψ and corresponding residue. Reprinted from [15].

For every pixel a single solution is assumed. In the presence of two feasible solutions, the one to which the method converges depends on the initialization. As seen in figure 4.1 an incorrect field map value due to a local minima does not necessarily imply a pixel swapping, as alternating aliased solutions correctly estimate the dominant component (with the exception of $\psi_e \approx 580$ Hz). Even though the correct dominant species is given, the fat-water ratio at a local minimum is not the true ratio.

Several different approaches have been introduced in literature to overcome the local minima entrapment, such as the hierarchical IDEAL [16], a region growing method [15] and a max-flow based approach [18]. The introduction of a more robust approach to avoid being trapped by a local minima would have overreached the scope of work for this thesis.

Regarding the thesis' goal of size determination, the true fat-water ratio is not necessary and does not impair the obtained size values as long as the true dominant component is determined. For the calculation of the water fraction a manual exclusion of possible imperfect decomposition was necessary.

The image quality was objectively measured by comparing the merged water and fat image with the original in quadrature image. Out of the three image quality metrics calculated, the similarity index is most suitable to asses the perceptual image quality. The highest dissimilarities around the haematoma and in regions of fatty tissues are due to separation ambiguity at the borders between different tissues and the fact that the IDEAL-algorithm effectively corrects for chemical shift.[1]

Though the calculations for this thesis were accomplished in MATLAB, the shorter execution time in Java (see table 3.2) should be considered if the algorithm is to be applied in a time sensitive manner.

The main advantage of chemical shift based water-fat separation compared to fat saturation or water excitation is that neither the water information nor the fat information is lost. However this additional information involves a more complex reconstruction and longer scan times. The separated fat and water components can be recombined in different manners to create different images such as the 'in-phase' image (water + fat), the 'out-of-phase' image (water - fat), the 'fat fraction' image (fat/(water+fat)), the 'water fraction' image (water/(water+fat)) and the 'fat:water ratio' image (fat/water).[10]

4.2. Size Determination

After the successful decomposition of the water and fat components, the relative size of each haematoma was obtained by ways of segmentation and thresholding. The time-depended trend of the absolute and relative size of all test subjects (see figures 3.10 and 3.11) indicate an exponential decline. This indication was confirmed by the exponential regression models calculated for each test subject's haematoma (see chapter C.2). The high coefficient of variation for the last week of observation is due to the different rates of the healing process of each test subject. For several subjects no haematoma could be observed as early as one week after the initial injection.

The different rates of the healing process also caused the high variance between the coefficients b of the regression lines, as an increase of the base of an exponential function increases the decay speed of an exponential function.
The rapid decline of P13 can be observed in figure 3.11. The presumed decline of P8 is uncertain, as no data points for 3 and 7 days after the injection could be used (see figure C.3).

The coefficient a defines the ordinate-intercept of the regression line. Assuming that the haematoma's maximum size occurred directly after the injection, the coefficient a should be 1, as the data set was normalized. The deviation from 1 is small for most test subjects and can be explained by small size increases after the injection. These increases can either be true increases due to spreading of the blood in the thigh or to developing of an oedema because of a trauma caused by the injection or false increases due to imperfect segmentation.

The proposed exponential regression model fits most test subjects data well, as can be observed by the coefficient of determination in figure 3.17. Two of the three test subjects deviate (P10 and P23) , because of missing data points for the haematoma size past 7 days after injection.

As the haematoma's size has to be normalized for effective comparison, the simple separation of the water and fat components and subsequent size determination is no valuable option to determine the age of a subcutaneous haematoma. The need for normalization does not exists for fraction images.

4.3. Water Fraction

The calculation of the average water fraction of the haematoma builds on the size determination, as it uses the final segmentation mask to split the haematoma from the rest of the fraction image. The average water fraction of a haematoma decreases with time, as the fluid components of the haematoma are more easily reduced than the solid components.

The exclusion of certain images, because they were assumed to contain incorrect water/fat ratios due to presumed local minima entrapment, introduced some bias in the results of the water fractions.

The average water content of adipose tissue according to literature is in the range of 11.4 - 30.5 % [23]. The mean of the water fraction only lies inside this range one and two weeks after the injection. This coincides with the earliest time points for visual disappearance of the haematoma.

The heighten water fraction due to a haematoma does decrease over time. The coefficient of variation increases over time, which was also observed during the size determination. However, the CV is far smaller for the water fraction determination, because the water fraction does not tend to zero.

The coefficient *a* represents the water content of the haematoma at the starting point. Presumable the initial water content varies with the water content of blood (79 - 80.8 % [23]) and the baseline water content of the adipose tissue. The coefficient *b* represents the decline of the water content. The coefficient of variation for coefficient *b* is low (see table 3.10). This indicates that the water content drop over the time is similar between all test subjects and over all depended on the baseline water content of fatty tissue and the age of the haematoma.

4.4. Conclusion

This thesis has shown that the IDEAL-algorithm can be used to analyse the properties of subcutaneous haematoma. Though size determination is possible, the true benefit of a fat/water separation instead of a fat or water suppression emerges with the utilization of both the water and the fat image together. The water fraction of a subcutaneous haematoma could be an useful diagnostic parameter concerning the age of a haematoma. Further studies should try to implement a more robust IDEAL-algorithm, that addresses the local minima problem, and accounts for the baseline water fraction of the adipose tissue.

Bibliography

[1] T. A. Bley, O. Wieben, C. J. François, J. H. Brittain, and S. B. Reeder, "Fat and water magnetic resonance imaging," *Journal of Magnetic Resonance Imaging*, vol. 31, no. 1, pp. 4–18, 2010, ISSN: 1522-2586 (cit. on pp. 1, 2, 4, 5, 65, 67).

[2] S. B. Reeder, A. R. Pineda, Z. Wen, A. Shimakawa, H. Yu, J. H. Brittain, G. E. Gold, C. H. Beaulieu, and N. J. Pelc, "Iterative decomposition of water and fat with echo asymmetry and least-squares estimation (ideal): Application with fast spin-echo imaging," *Magnetic resonance in medicine*, vol. 54, no. 3, pp. 636–644, 2005 (cit. on p. 2).

[3] M. Bernstein, K. King, and X. Zhou, *Handbook of MRI Pulse Sequences*. Elsevier Science, 2004, ch. 10, ISBN: 9780080533124 (cit. on pp. 2, 9–11).

[4] E. M. Hassler, K. Ogris, A. Petrovic, B. Neumayer, T. Widek, K. Yen, and E. Scheurer, "Contrast of artificial subcutaneous hematomas in mri over time," *International journal of legal medicine*, vol. 129, no. 2, pp. 317–324, 2015 (cit. on pp. 3, 14).

[5] K. Ogris, A. Petrovic, S. Scheicher, H. Sprenger, M. Urschler, E. M. Hassler, K. Yen, and E. Scheurer, "Detection and volume estimation of artificial hematomas in the subcutaneous fatty tissue: Comparison of different mr sequences at 3.0 t," *Forensic science, medicine, and pathology*, vol. 13, no. 2, pp. 135–144, 2017 (cit. on p. 3).

[6] A. Petrovic, A. Krauskopf, E. Hassler, R. Stollberger, and E. Scheurer, "Time related changes of t1, t2, and t2* of human blood in vitro," *Forensic science international*, vol. 262, pp. 11–17, 2016 (cit. on p. 3).

[7] R. K. Harris, E. D. Becker, S. M. C. De Menezes, R. Goodfellow, and P. Granger, "Nmr nomenclature. nuclear spin properties and conventions for chemical shifts (iupac recommendations 2001)," *Pure and Applied Chemistry*, vol. 73, no. 11, pp. 1795–1818, 2001 (cit. on p. 4).

[8] J. Ma, "Dixon techniques for water and fat imaging," *Journal of Magnetic Resonance Imaging*, vol. 28, no. 3, pp. 543–558, 2008, ISSN: 1522-2586 (cit. on pp. 5, 7, 8, 11, 13).

[9] B. Neumayer, E. Hassler, A. Petrovic, T. Widek, K. Ogris, and E. Scheurer, "Age determination of soft tissue hematomas," *NMR in Biomedicine*, vol. 27, no. 11, pp. 1397–1402, 2014 (cit. on p. 14).

[10] S. B. Reeder, C. A. McKenzie, A. R. Pineda, H. Yu, A. Shimakawa, A. C. Brau, B. A. Hargreaves, G. E. Gold, and J. H. Brittain, "Water–fat separation with ideal gradient-echo imaging," *Journal of Magnetic Resonance Imaging*, vol. 25, no. 3, pp. 644–652, 2007 (cit. on pp. 15, 67).

[11] MATLAB, *Version 8.6.0.267246 (R2015b)*. Natick, Massachusetts: The MathWorks Inc., 2015 (cit. on p. 16).

[12] P. A. Yushkevich, J. Piven, H. Cody Hazlett, R. Gimpel Smith, S. Ho, J. C. Gee, and G. Gerig, "User-guided 3D active contour segmentation of anatomical structures: Significantly improved efficiency and reliability," *Neuroimage*, vol. 31, no. 3, pp. 1116–1128, 2006 (cit. on p. 16).

[13] S. B. Reeder, Z. Wen, H. Yu, A. R. Pineda, G. E. Gold, M. Markl, and N. J. Pelc, "Multicoil dixon chemical species separation with an iterative least-squares estimation method," *Magnetic Resonance in Medicine*, vol. 51, no. 1, pp. 35–45, 2004 (cit. on pp. 16, 21).

[14] A. Bjórck, *Numerical Methods for Least Squares Problems*, ser. Other Titles in Applied Mathematics. Society for Industrial and Applied Mathematics (SIAM, 3600 Market Street, Floor 6, Philadelphia, PA 19104), 1996, ISBN: 9781611971484 (cit. on p. 17).

[15] H. Yu, S. B. Reeder, A. Shimakawa, J. H. Brittain, and N. J. Pelc, "Field map estimation with a region growing scheme for iterative 3-point water-fat decomposition," *Magnetic resonance in medicine*, vol. 54, no. 4, pp. 1032–1039, 2005 (cit. on pp. 25, 65, 66).

[16] J. Tsao and Y. Jiang, "Hierarchical ideal: Fast, robust, and multiresolution separation of multiple chemical species from multiple echo times," *Magnetic Resonance in Medicine*, vol. 70, no. 1, pp. 155–159, 2012 (cit. on pp. 25, 66).

[17] M. Jacob and B. P. Sutton, "Algebraic decomposition of fat and water in mri," *IEEE Transactions on Medical Imaging*, vol. 28, no. 2, pp. 173–184, Feb. 2009, ISSN: 0278-0062 (cit. on p. 25).

[18] A. S. Soliman, J. Yuan, K. K. Vigen, J. A. White, T. M. Peters, and C. A. McKenzie, "Max-ideal: A max-flow based approach for ideal water/fat separation," *Magnetic Resonance in Medicine*, vol. 72, no. 2, pp. 510–521, (cit. on pp. 25, 66).

[19] D.-J. Kroon, *Read medical data 3d*, version 1.1, Feb. 19, 2018. [Online]. Available: https://de.mathworks.com/matlabcentral/fileexchange/29344-read-medical-data-3d (cit. on p. 27).

[20] Mathworks. (2018). multithresh multilevel image thresholds using otsu's method, [Online]. Available: https://de.mathworks.com/help/images/ref/multithresh.html (visited on 05/04/2018) (cit. on p. 27).

[21] D. Altman, D. Machin, T. Bryant, and M. Gardner, *Statistics with Confidence: Confidence Intervals and Statistical Guidelines*. Wiley, 2013, ch. 8, ISBN: 9781118702505 (cit. on p. 29).

[22] J. Natrop, *Angewandte Deskriptive Statistik: Praxisbezogenes Lehrbuch Mit Fallbeispielen*, ser. De Gruyter Studium. De Gruyter Oldenbourg, 2015, ISBN: 9783110408584 (cit. on p. 29).

[23] F. Duck, *Physical Properties of Tissues: A Comprehensive Reference Book*. Elsevier Science, 2013, ISBN: 9781483288420 (cit. on p. 70).

Appendices

A. Comparision of Matlab, Java and Python Implementation

Besides the overall execution time for all three implementations (see figure 3.8). Interim times were measured for three different subprocess of the whole implementation.

- The first subprocess was the import and preprocessing of the DICOM images (see figure A.1).
- The second subprocess was the IDEAL algorithm itself (see figure A.2).
- The third subprocess was the export of the decomposed images ad DICOM files (see figure A.3).

Figure A.4 shows these interim times as percentage of the overall execution time. Table A.1 displays the profiling tools used to obtain the measured times.

Table A.1.: Profiling tools

Matlab	Python	Java
MATLAB Profiler	cProfile	YourKit

Used Profilers for Matlab, Python and Java

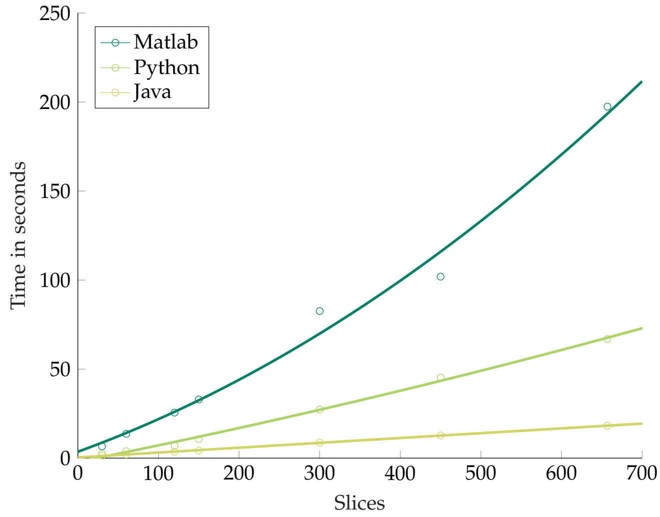

Figure A.1.: Import execution time of Matlab, Java and Python implementation.

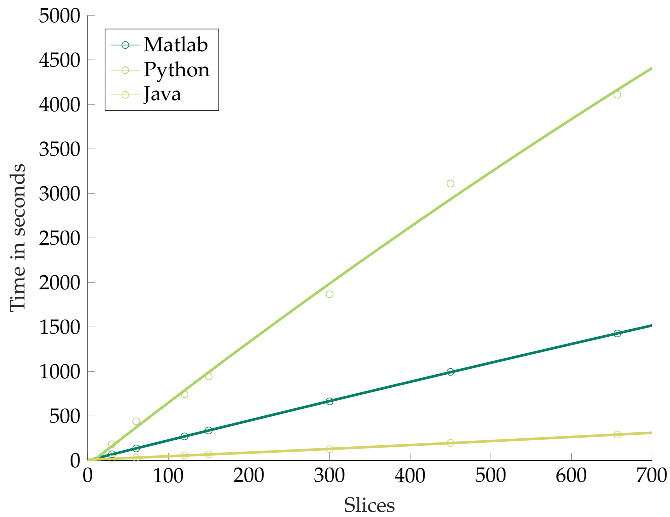

Figure A.2.: IDEAL execution time of Matlab, Java and Python implementation.

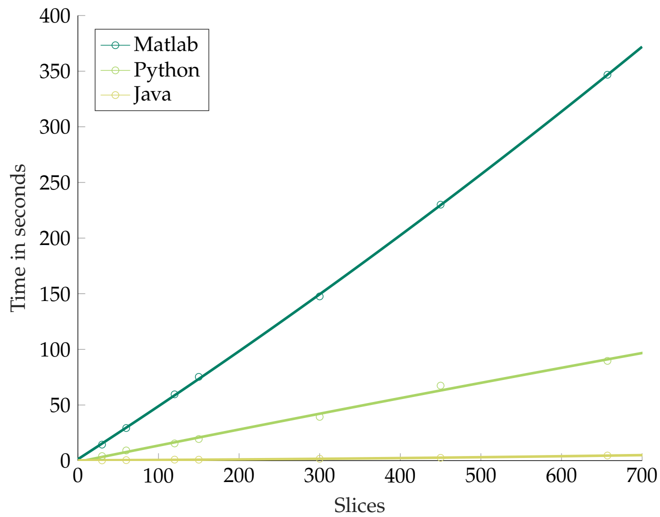

Figure A.3.: Export execution time of Matlab, Java and Python implementation.

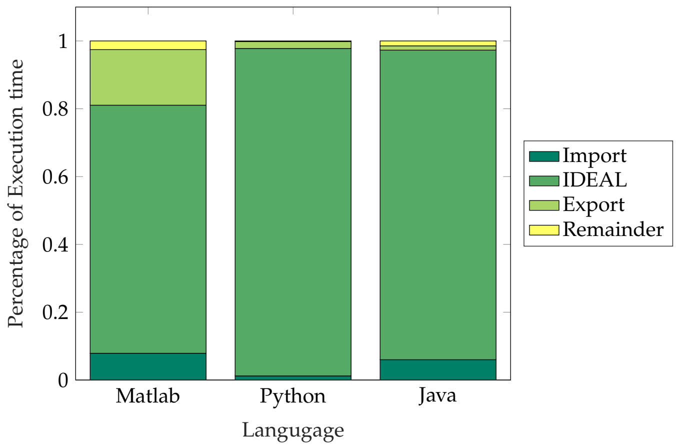

Figure A.4.: Percentage of execution time for each step of the Matlab, Java and Python implementation. The yellow remainder exists, as each steps is represented by the mean over its percentage for different amounts of slices and as a clean separation of each step was only possible for python.

B. Test Data

Table B.1.: Test person's weight, age and sex

Test person	Weight (kg)	Age (years)	Sex
P6	85	24	M
P7	65	25	F
P8	70	21	F
P9	65	28	F
P10	65	24	M
P11	70	26	M
P12	60	32	F
P13	60	25	F
P14	65	18	M
P15	75	25	M
P16	65	26	F
P17	70	26	F
P18	70	25	F
P19	85	25	M
P20	75	27	M
P21	65	32	F
P22	115	31	M

Test person	Weight (kg)	Age (years)	Sex
P23	56	24	F
P24	59	25	F
P25	95	35	M
P26	66	21	M
P27	75	24	M
P28	65	24	F
P29	85	28	M
P30	75	23	M
P31	105	22	F
P32	56	22	F
P33	66	22	M
P34	105	22	F
P35	82	25	M
P36	70	23	M
P38	80	23	M
P39	70	28	F
P40	76	23	M

Table B.2.: Test person Data

Study Nummer	Test person	Time of measurement	Initial Estimate ψ_0	No successful decompositions
032-11-F	P6/S1	B	0	
033-11-F	P6/S2	P.I.	0.2	
035-11-F	P6/S3	3 h	0	
036-11-F	P6/S4	1 d	0.2	
038-11-F	P6/S5	3 d	0	
040-11-F	P6/S6	7 d	0	
042-11-F	P6/S7	14 d	-	X
044-11-F	P7/S1	B	0.3	
045-11-F	P7/S2	P.I.	0.3	
048-11-F	P7/S3	3 h	0	
050-11-F	P7/S4	1 d	0	
052-11-F	P7/S5	3 d	0.3	
054-11-F	P7/S6	7 d	0	
056-11-F	P7/S7	14 d	0	
046-11-F	P8/S1	B	0	
047-11-F	P8/S2	P.I.	0	
049-11-F	P8/S3	3 h	0	
051-11-F	P8/S4	1 d	0.2	
053-11-F	P8/S5	3 d	-	X
055-11-F	P8/S6	7 d	-	X
057-11-F	P8/S7	14 d	0.3	
058-11-F	P9/S1	B	0.2	
059-11-F	P9/S2	P.I.	0	
062-11-F	P9/S3	3 h	0	
064-11-F	P9/S4	1 d	0	
066-11-F	P9/S5	3 d	0	
068-11-F	P9/S6	7 d	0	
070-11-F	P9/S7	14 d	0	
060-11-F	P10/S1	B	0.2	
061-11-F	P10/S2	P.I.	-	X
063-11-F	P10/S3	3 h	0.2	
065-11-F	P10/S4	1 d	0.2	
067-11-F	P10/S5	3 d	0.2	
069-11-F	P10/S6	7 d	0	
071-11-F	P10/S7	14 d	0.2	
072-11-F	P11/S1	B	0	

073-11-F	P11/S2	P.I.	-	X
076-11-F	P11/S3	3 h	0.2	
078-11-F	P11/S4	1 d	0.2	
080-11-F	P11/S5	3 d	0	
082-11-F	P11/S6	7 d	0.2	
084-11-F	P11/S7	14 d	0	
074-11-F	P12/S1	B	0	
075-11-F	P12/S2	P.I.	-	X
077-11-F	P12/S3	3 h	0	
079-11-F	P12/S4	1 d	0.2	
081-11-F	P12/S5	3 d	0.3	
083-11-F	P12/S6	7 d	-	X
085-11-F	P12/S7	14 d	0.3	
086-11-F	P13/S1	B	0.2	
087-11-F	P13/S2	P.I.	0	
090-11-F	P13/S3	3 h	0.2	
092-11-F	P13/S4	1 d	0.2	
094-11-F	P13/S5	3 d	0.3	
096-11-F	P13/S6	7 d	0.2	
088-11-F	P14/S1	B	0.2	
089-11-F	P14/S2	P.I.	0.2	
091-11-F	P14/S3	3 h	0	
093-11-F	P14/S4	1 d	0	
095-11-F	P14/S5	3 d	0	
097-11-F	P14/S6	7 d	0.2	
098-11-F	P14/S7	14 d	0	
402-11-F	P15/S1	B	-	X
403-11-F	P15/S2	P.I.	0	
404-11-F	P15/S3	3 h	0	
405-11-F	P15/S4	1 d	0	
406-11-F	P15/S5	3 d	0.2	
407-11-F	P15/S6	7 d	0	
408-11-F	P15/S7	14 d	0	
409-11-F	P16/S1	B	0.2	
410-11-F	P16/S2	P.I.	0	
413-11-F	P16/S3	3 h	0	
415-11-F	P16/S4	1 d	0	
417-11-F	P16/S5	3 d	0	
419-11-F	P16/S6	7 d	-	X
421-11-F	P16/S7	14 d	0	

411-11-F	P17/S1	B	0.2	
412-11-F	P17/S2	P.I.	-	X
414-11-F	P17/S3	3 h	0	
416-11-F	P17/S4	1 d	0.2	
418-11-F	P17/S5	3 d	0	
420-11-F	P17/S6	7 d	0	
422-11-F	P17/S7	14 d	0	
423-12-F	P18/S1	B	0.2	
424-12-F	P18/S2	P.I.	0	
427-12-F	P18/S3	3 h	-	X
429-12-F	P18/S4	1 d	0.2	
431-12-F	P18/S5	3 d	0.3	
433-12-F	P18/S6	7 d	0	
435-12-F	P18/S7	14 d	0	
425-12-F	P19/S1	B	0.2	
426-12-F	P19/S2	P.I.	0.2	
428-12-F	P19/S3	3 h	-	X
430-11-F	P19/S4	1 d	0	
432-12-F	P19/S5	3 d	0	
434-12-F	P19/S6	7 d	-	X
436-12-F	P19/S7	14 d	0	
437-12-F	P20/S1	B	0.2	
438-12-F	P20/S2	P.I.	0	
439-12-F	P20/S3	3 h	0	
440-12-F	P20/S4	1 d	0.2	
441-12-F	P20/S5	3 d	0.3	
442-12-F	P20/S6	7 d	0.2	
443-12-F	P20/S7	14 d	0.2	
1600	P21/S1	P.I.	0.2	
1602	P21/S2	3 h	exclusion due to artefacts	
1604	P21/S3	1 d	exclusion due to artefacts	
1606	P21/S4	3 d	0	
1608	P21/S5	7 d	0	
1610	P21/S6	14 d	exclusion due to artefacts	
	P22		exclusion due to artefacts	
1612	P23/S1	P.I.	exclusion due to artefacts	
1614	P23/S2	3 h	0	
1616	P23/S3	1 d	0.2	
1618	P23/S4	3 d	0.2	

1620	P23/S5	7 d	0	
1622	P23/S6	14 d	exclusion due to artefacts	
1613	P24/S1	P.I.	exclusion due to artefacts	
1615	P24/S2	3 h	0.2	
1617	P24/S3	1 d	0.2	
1619	P24/S4	3 d	0.3	
1621	P24/S5	7 d	exclusion due to artefacts	
1623	P24/S6	14 d	exclusion due to artefacts	
	P25		exclusion due to artefacts	
	P26		exclusion due to artefacts	
1636	P27/S1	P.I.	exclusion due to artefacts	
1638	P27/S2	3 h	exclusion due to artefacts	
1640	P27/S3	1 d	0	
1642	P27/S4	3 d	0	
1644	P27/S5	7 d	0	
1646	P27/S6	14 d	-	X
1637	P28/S1	P.I.	0	
1639	P28/S2	3 h	-0.2	
1641	P28/S3	1 d	0	
1643	P28/S4	3 d	0	
1645	P28/S5	7 d	0.2	
1647	P28/S6	14 d	0	
1648	P29/S1	P.I.	-0.2	
1650	P29/S2	3 h	0.2	
1652	P29/S3	1 d	-	X
1654	P29/S4	3 d	0.2	
1656	P29/S5	7 d	0	
1658	P29/S6	14 d	0	
1649	P30/S1	P.I.	-	X
1651	P30/S2	3 h	-	X
1653	P30/S3	1 d	0	
1655	P30/S4	3 d		X
1657	P30/S5	7 d	0	
1659	P30/S6	14 d	0.2	
1660	P31/S1	P.I.	0.2	
1662	P31/S2	3 h	0	
1664	P31/S3	1 d	-	X
1666	P31/S4	3 d	0.3	
1668	P31/S5	7 d	0	
1670	P31/S6	14 d	-	X

1661	P32/S1	P.I.	0	
1663	P32/S2	3 h	0	
1665	P32/S3	1 d	0.2	
1667	P32/S4	3 d	0	
1669	P32/S5	7 d	0	
1671	P32/S6	14 d	0	
1672	P33/S1	P.I.	-	X
1674	P33/S2	3 h	0.2	
1676	P33/S3	1 d	-	X
1678	P33/S4	3 d	-	X
1680	P33/S5	7 d	-	X
1682	P33/S6	14 d	0	
1673	P34/S1	P.I.	0	
1675	P34/S2	3 h	0	
1677	P34/S3	1 d	0	
1679	P34/S4	3 d	0	
1681	P34/S5	7 d	0.2	
1683	P34/S6	14 d	0	
1684	P35/S1	P.I.	0	
1686	P35/S2	3 h	0.2	
1688	P35/S3	1 d	0	
1690	P35/S4	3 d	0	
1692	P35/S5	7 d	0	
1694	P35/S6	14 d	-	X
1685	P36/S1	P.I.	0	
1687	P36/S2	3 h	-	X
1689	P36/S3	1 d	-	X
1691	P36/S4	3 d	0	
1693	P36/S5	7 d	-	X
1695	P36/S6	14 d	0	
1696	P38/S1	P.I.	0	
1697	P38/S2	3 h	0	
1698	P38/S3	1 d	0.2	
1699	P38/S4	3 d	0	
1700	P38/S5	7 d	-	X
1701	P38/S6	14 d	0	
1702	P39/S1	P.I.	0	
1704	P39/S2	3 h	-	X
1706	P39/S3	1 d	0	

1708	P39/S4	3 d	0	
1710	P39/S5	7 d	0	
1712	P39/S6	14 d	-	X
1703	P40/S1	P.I.	0.2	
1705	P40/S2	3 h	0	
1707	P40/S3	1 d	0	
1709	P40/S4	3 d	0	
1711	P40/S5	7 d	0	
1713	P40/S6	14 d	0	

C. Regression Models

C.1. Included Test subjects

Table C.1.: Included Test subjects

Test subject	Size vs Time	Water Fraction vs Time	Test subject	Size vs Time	Water Fraction vs Time
P6	x	x	P23	x	x
P7	x		P24	x	x
P8	x	x	P27	x	
P9	x	x	P28	x	x
P10	x	x	P29	x	x
P11	x	x	P30	x	
P12	x	x	P31	x	x
P13	x	x	P32	x	x
P14	x	x	P33	x	
P15	x	x	P34	x	x
P16	x	x	P35	x	x
P17	x	x	P36	x	x
P18	x	x	P38	x	x
P19	x	x	P39	x	x
P20	x	x	P40	x	x
P21	x	x			

Included test subject for size vs time and water fraction vs time analyses

C.2. Size vs Time

P6

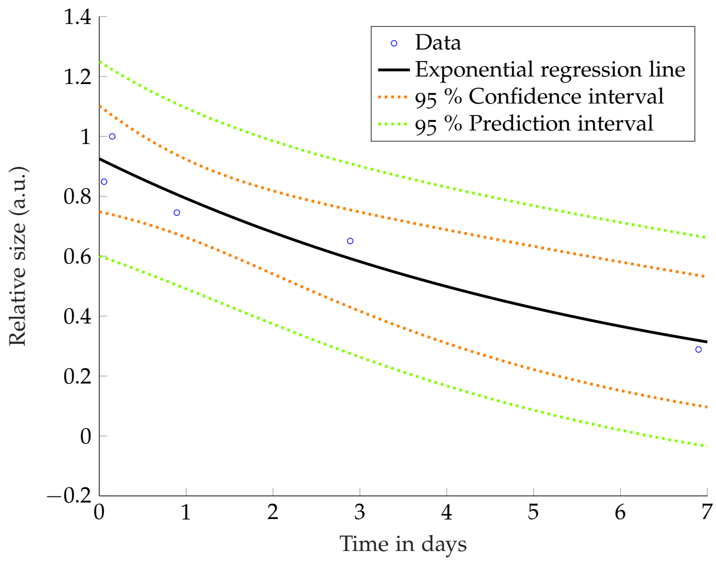

Figure C.1.: Graph of regression model

Table C.2.: Model parameter

Coefficients	a	b
Estimate	0.92523	0.85683
SE	0.055539	0.029668
tStat	16.659	28.88
p-Value	0.00047089	$9.1157 * 10^{-5}$

Parameter estimates and statistically values

Table C.3.: Model parameter

	Confidence interval	Prediction interval
Mean	(0.38951) - (0.74281)	(0.24058) - (0.89173)
SD	(0.2075) - (0.15135)	(0.19418) - (0.16374)

0.95% confidence and 0.95% prediction intervals

Table C.4.: Metrics of regression model

R^2	R^2_{adj}	SSE	SSR	SST	RMSE	pValue
0.923	0.898	0.021944	0.25691	0.28567	0.0855	0.0007

Statistically values for regression model

P7

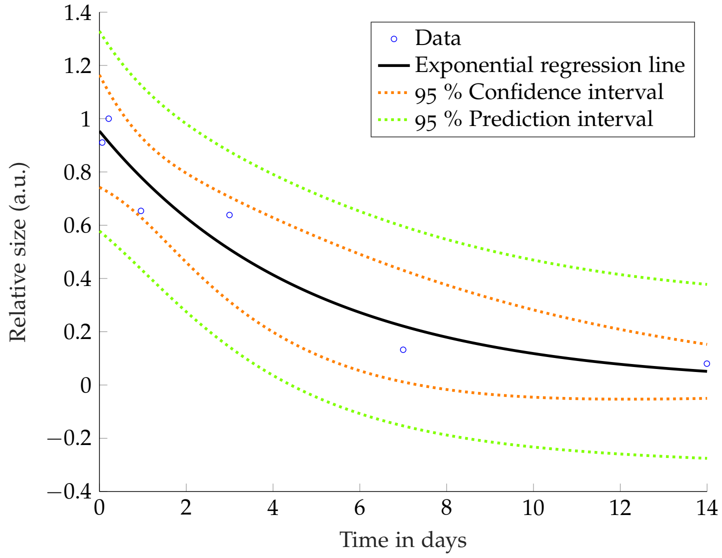

Figure C.2.: Graph of regression model

Table C.5.: Model parameter

Coefficients	a	b
Estimate	0.95353	0.81154
SE	0.075972	0.043431
tStat	12.551	18.686
p-Value	0.00023188	$4.8289*10^{-5}$

Parameter estimates and statistically values

Table C.6.: Model parameter

	Confidence interval	Prediction interval
Mean	(0.13434) - (0.48568)	(-0.048038) - (0.66806)
SD	(0.23994) - (0.26084)	(0.24403) - (0.25317)

0.95% confidence and 0.95% prediction intervals

Table C.7.: Metrics of regression model

R^2	R^2_{adj}	SSE	SSR	SST	RMSE	pValue
0.933	0.916	0.050003	0.69314	0.7439	0.112	0.000346

Statistically values for regression model

P8

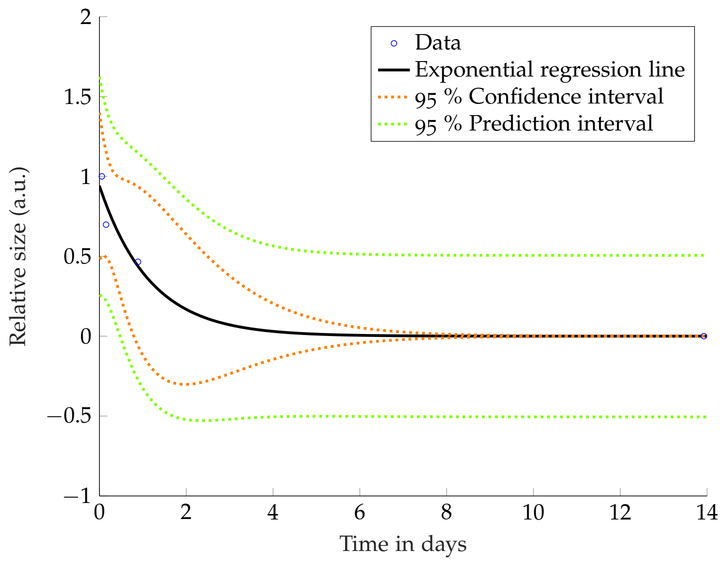

Figure C.3.: Graph of regression model

Table C.8.: Model parameter

Coefficients	a	b
Estimate	0.94107	0.42224
SE	0.10661	0.15038
tStat	8.8273	2.8078
pValue	0.012592	0.10689

Parameter estimates and statistically values

Table C.9.: Model parameter

	Confidence interval	Prediction interval
Mean	(-0.049008) - (0.2106)	(-0.46568) - (0.62727)
SD	(0.13926) - (0.33212)	(0.14349) - (0.2368)

0.95% confidence and 0.95% prediction intervals

Table C.10.: Metrics of regression model

R^2	R^2_{adj}	SSE	SSR	SST	RMSE	pValue
0.948	0.922	0.027598	0.51052	0.53368	0.117	0.0162

Statistically values for regression model

P9

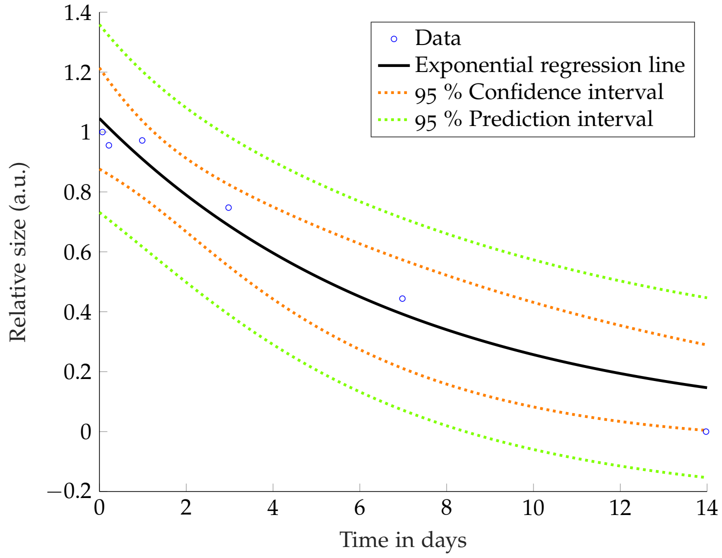

Figure C.4.: Graph of regression model

Table C.11.: Model parameter

Coefficients	a	b
Estimate	1.0453	0.86905
SE	0.060858	0.023358
tStat	17.177	37.205
p-Value	$6.7397*10^{-5}$	$3.1164*10^{-6}$

Parameter estimates and statistically values

Table C.12.: Model parameter

	Confidence interval	Prediction interval
Mean	(0.29902) - (0.61782)	(0.14955) - (0.76729)
SD	(0.26654) - (0.24408)	(0.2605) - (0.24942)

0.95% confidence and 0.95% prediction intervals

Table C.13.: Metrics of regression model

R^2	R^2_{adj}	SSE	SSR	SST	RMSE	pValue
0.954	0.942	0.036178	0.65616	0.78585	0.0951	0.0001

Statistically values for regression model

P10

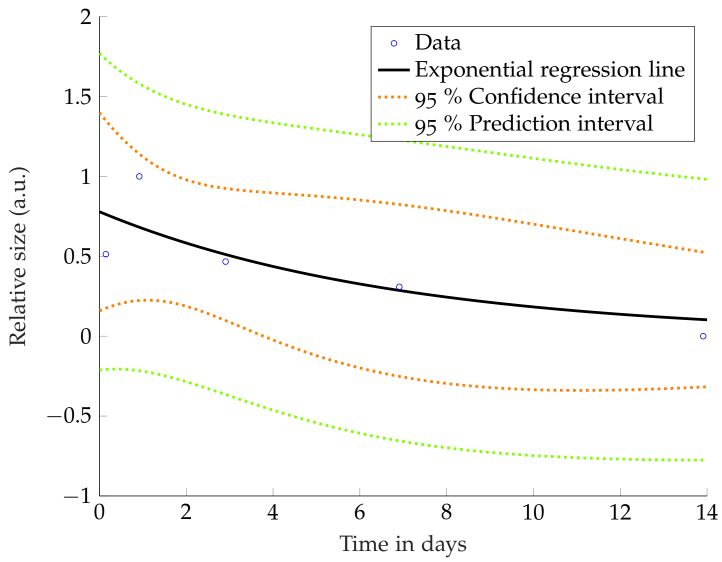

Figure C.5.: Graph of regression model

Table C.14.: Model parameter

Coefficients	a	b
Estimate	0.77876	0.86515
SE	0.19494	0.087307
tStat	3.9948	9.9092
p-Value	0.028104	0.002186

Parameter estimates and statistically values

Table C.15.: Model parameter

	Confidence interval	Prediction interval
Mean	(-0.15159) - (0.82006)	(-0.57924) - (1.2477)
SD	(0.20748) - (0.18752)	(0.19801) - (0.18825)

0.95% confidence and 0.95% prediction intervals

Table C.16.: Metrics of regression model

R^2	R^2_{adj}	SSE	SSR	SST	RMSE	pValue
0.666	0.554	0.17673	0.30036	0.52887	0.243	0.0375

Statistically values for regression model

P11

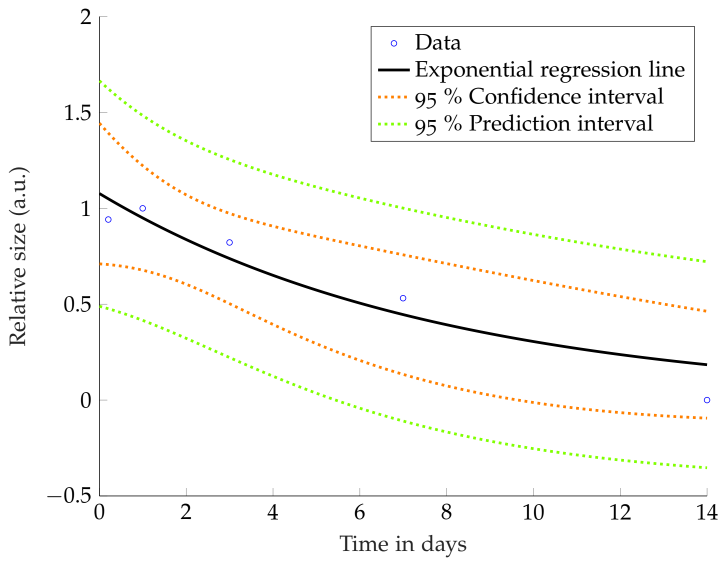

Figure C.6.: Graph of regression model

Table C.17.: Model parameter

Coefficients	a	b
Estimate	1.0772	0.88155
SE	0.11529	0.033369
tStat	9.3436	26.418
p-Value	0.002596	0.000119

Parameter estimates and statistically values

Table C.18.: Model parameter

	Confidence interval	Prediction interval
Mean	(0.21621) - (0.79725)	(-0.037488) - (1.0509)
SD	(0.26985) - (0.24205)	(0.26188) - (0.24789)

0.95% confidence and 0.95% prediction intervals

Table C.19.: Metrics of regression model

R^2	R^2_{adj}	SSE	SSR	SST	RMSE	pValue
0.907	0.876	0.062525	0.51421	0.67327	0.144	0.00326

Statistically values for regression model

P12

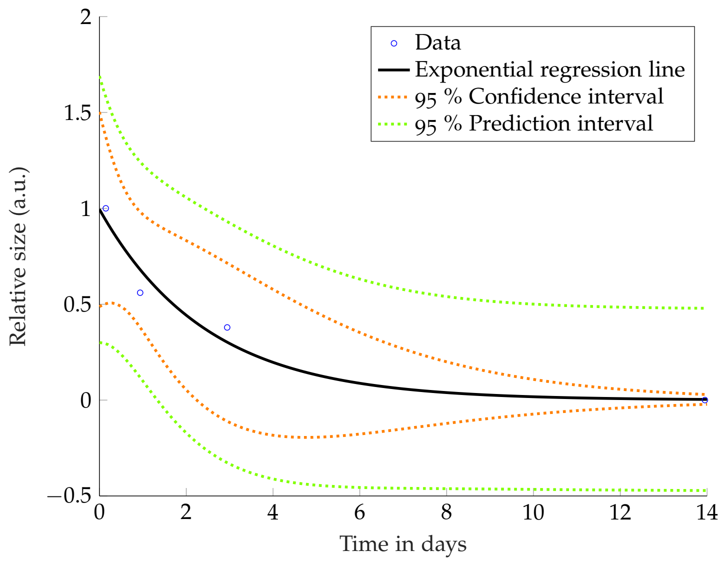

Figure C.7.: Graph of regression model

Table C.20.: Model parameter

Coefficients	a	b
Estimate	0.99503	0.66689
SE	0.11802	0.085744
tStat	8.4313	7.7776
p-Value	0.013777	0.016132

Parameter estimates and statistically values

Table C.21.: Model parameter

	Confidence interval	Prediction interval
Mean	(-0.039483) - (0.39379)	(-0.35957) - (0.71387)
SD	(0.17509) - (0.35595)	(0.20534) - (0.28816)

0.95% confidence and 0.95% prediction intervals

Table C.22.: Metrics of regression Model

R^2	R^2_{adj}	SSE	SSR	SST	RMSE	pValue
0.953	0.929	0.024326	0.50819	0.51733	0.11	0.0167

Statistically values for regression model

P13

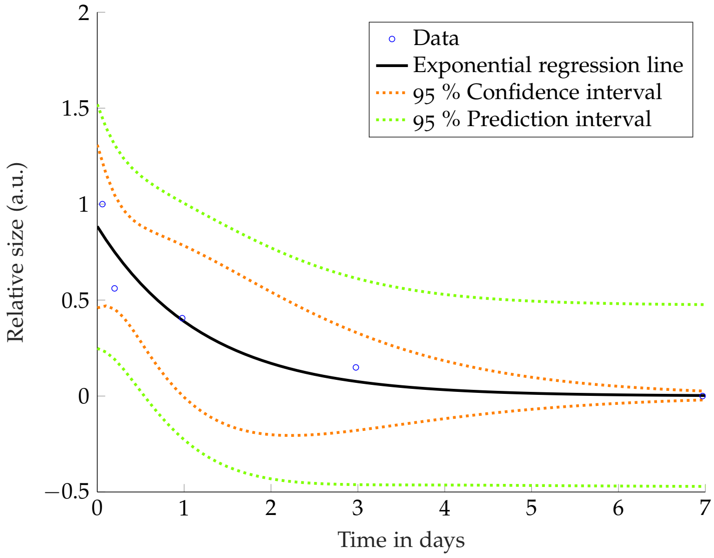

Figure C.8.: Graph of regression model

Table C.23.: Model parameter

Coefficients	a	b
Estimate	0.88429	0.43901
SE	0.13346	0.16691
tStat	6.626	2.6303
p-Value	0.0070017	0.0078307

Parameter estimates and statistically values

Table C.24.: Model parameter

	Confidence interval	Prediction interval
Mean	(-0.050963) - (0.36526)	(-0.37473) - (0.68902)
SD	(0.16283) - (0.32973)	(0.18698) - (0.26148)

0.95% confidence and 0.95% prediction intervals

Table C.25.: Metrics of regression Model

R^2	R^2_{adj}	SSE	SSR	SST	RMSE	pValue
0.891	0.854	0.066308	0.58075	0.60616	0.149	0.0854

Statistically values for regression model

P14

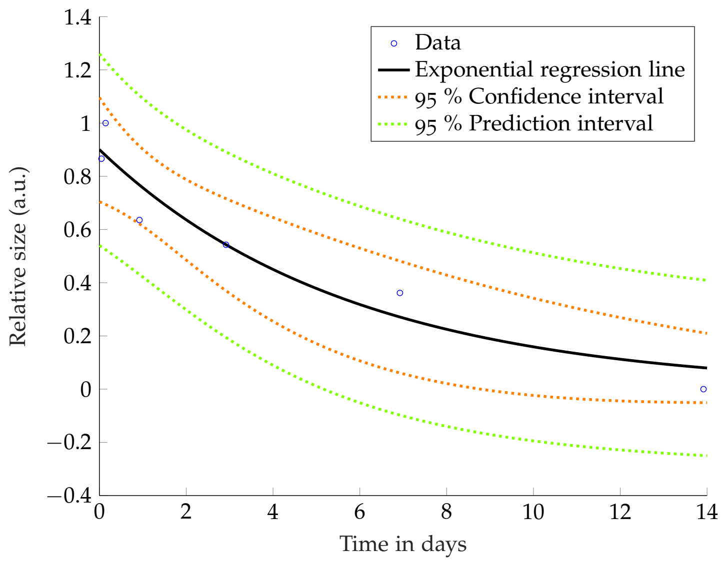

Figure C.9.: Graph of regression model

Table C.26.: Model parameter

Coefficients	a	b
Estimate	0.90027	0.84085
SE	0.070482	0.037477
tStat	12.773	22.436
p-Value	0.00021648	$2.3368*10^{-5}$

Parameter estimates and statistically values

Table C.27.: Model parameter

	Confidence interval	Prediction interval
Mean	(0.16068) - (0.51792)	(-0.012869) - (0.69146)
SD	(0.23271) - (0.22907)	(0.23085) - (0.22887)

0.95% Confidence and 0.95% prediction intervals

Table C.28.: Metrics of regression model

R^2	R^2_{adj}	SSE	SSR	SST	RMSE	pValue
0.926	0.908	0.047553	0.56774	0.64587	0.109	0.00034

Statistically values for regression model

P15

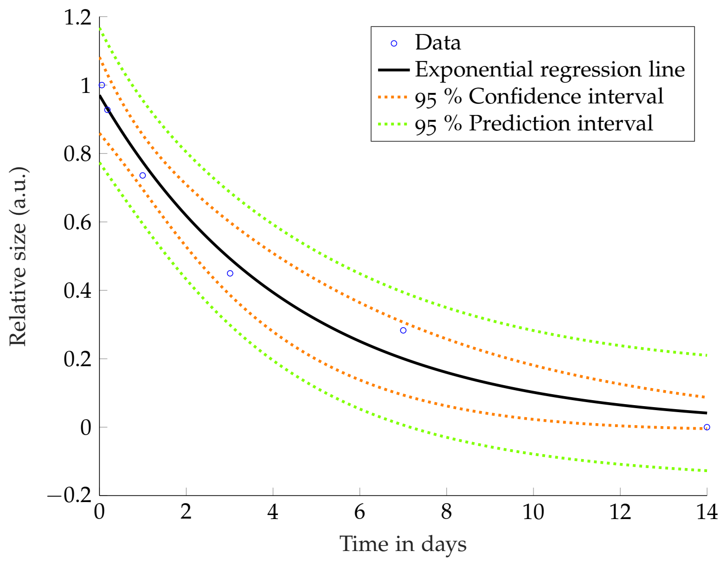

Figure C.10.: Graph of regression model

Table C.29.: Model parameter

Coefficients	a	b
Estimate	0.97056	0.79818
SE	0.040056	0.023773
tStat	24.23	33.575
p-Value	$1.7211*10^{-5}$	$4.6939*10^{-6}$

Parameter estimates and statistically values

Table C.30.: Model parameter

	Confidence interval	Prediction interval
Mean	(0.20674) - (0.38515)	(0.10976) - (0.48213)
SD	(0.2456) - (0.26249)	(0.24983) - (0.25708)

0.95% confidence and 0.95% prediction intervals

Table C.31.: Metrics of regression Model

R^2	R^2_{adj}	SSE	SSR	SST	RMSE	pValue
0.982	0.978	0.013674	0.74546	0.76198	0.0585	$2.59*10^{-5}$

Statistically values for regression model

P16

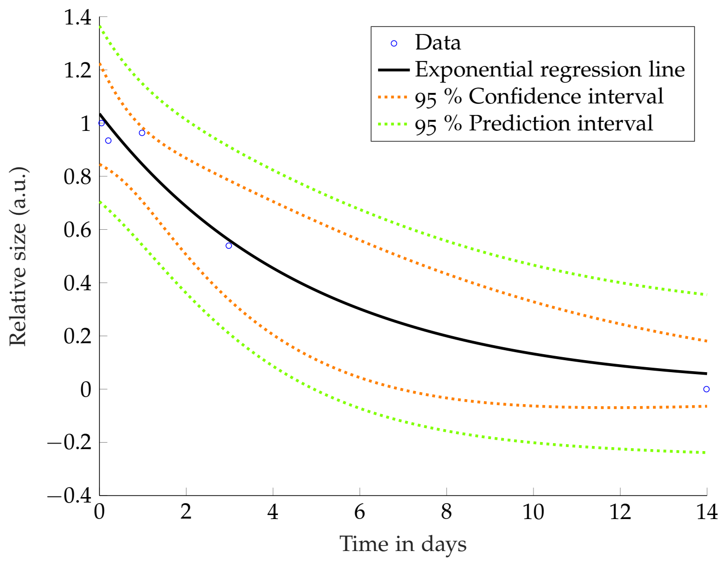

Figure C.11.: Graph of regression model

Table C.32.: Model parameter

Coefficients	a	b
Estimate	1.0353	0.81417
SE	0.05968	0.040134
tStat	17.348	20.287
p-Value	0.00041738	0.00026186

Parameter estimates and statistically values

Table C.33.: Model parameter

	Confidence interval	Prediction interval
Mean	(0.13951) - (0.54244)	(0.0020008) - (0.67996)
SD	(0.27381) - (0.27159)	(0.27104) - (0.26961)

0.95% confidence and 0.95% prediction intervals

Table C.34.: Metrics of regression Model

R^2	R^2_{adj}	SSE	SSR	SST	RMSE	pValue
0.97	0.96	0.021634	0.64383	0.72917	0.0849	0.000585

Statistically values for regression model

P17

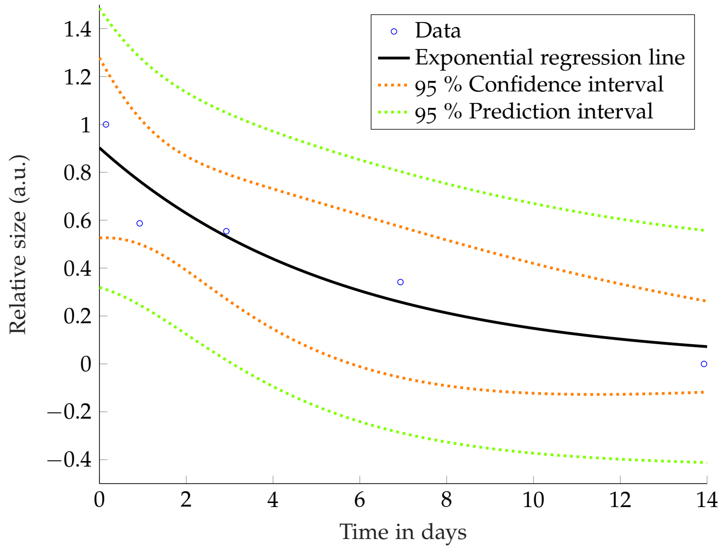

Figure C.12.: Graph of regression model

Table C.35.: Model parameter

Coefficients	a	b
Estimate	0.90246	0.83489
SE	0.11827	0.053371
tStat	7.6305	15.643
pValue	0.004673	0.00056774

Parameter estimates and statistically values

Table C.36.: Model parameter

	Confidence interval	Prediction interval
Mean	(0.056781) - (0.60279)	(-0.19362) - (0.85319)
SD	(0.22248) - (0.24623)	(0.22611) - (0.23832)

0.95% confidence and 0.95% prediction intervals

Table C.37.: Metrics of regression model

R^2	R^2_{adj}	SSE	SSR	SST	RMSE	pValue
0.89	0.854	0.058747	0.45433	0.53553	0.14	0.00606

Statistically values for regression model

P18

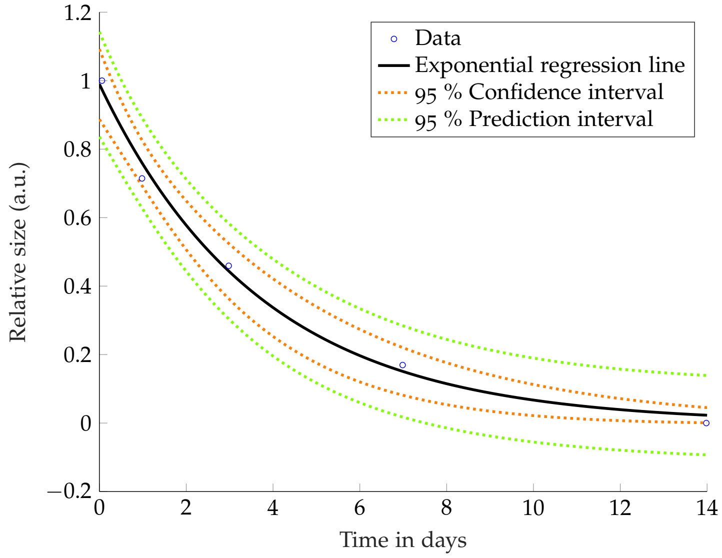

Figure C.13.: Graph of regression model

Table C.38.: Model parameter

Coefficients	a	b
Estimate	0.98959	0.76406
SE	0.032209	0.017503
tStat	30.724	43.652
p-Value	7.5748∗10^{-5}	2.6463∗10^{-5}

Parameter estimates and statistically values

Table C.39.: Model parameter

	Confidence interval	Prediction interval
Mean	(0.19802) - (0.31874)	(0.12819) - (0.38857)
SD	(0.24409) - (0.27138)	(0.25128) - (0.26344)

0.95% confidence and 0.95% prediction intervals

Table C.40.: Metrics of regression model

R^2	R^2_{adj}	SSE	SSR	SST	RMSE	pValue
0.994	0.992	0.0038404	0.64021	0.65203	0.0358	0.000103

Statistically values for regression model

P19

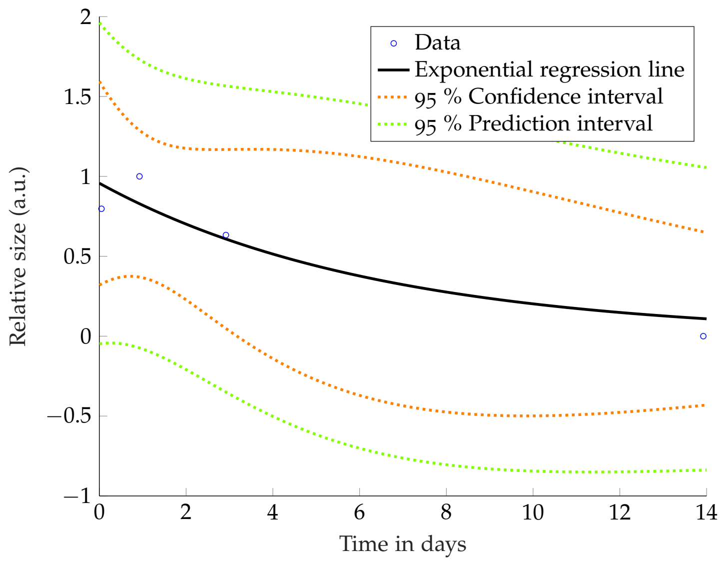

Figure C.14.: Graph of regression model

Table C.41.: Model parameter

Coefficients	a	b
Estimate	0.95706	0.85604
SE	0.14821	0.075469
tStat	6.4573	11.343
pValue	0.023153	0.0076828

Paramter estimates and statistically values

Table C.42.: Model parameter

	Confidence interval	Prediction interval
Mean	(-0.251) - (1.0328)	(-0.61993) - (1.4018)
SD	(0.30294) - (0.20368)	(0.27544) - (0.21379)

0.95% confidence and 0.95% prediction intervals

Table C.43.: Metrics of regression model

R^2	R^2_{adj}	SSE	SSR	SST	RMSE	pValue
0.883	0.825	0.065247	0.41377	0.55977	0.181	0.032

Statistically values for regression model

P20

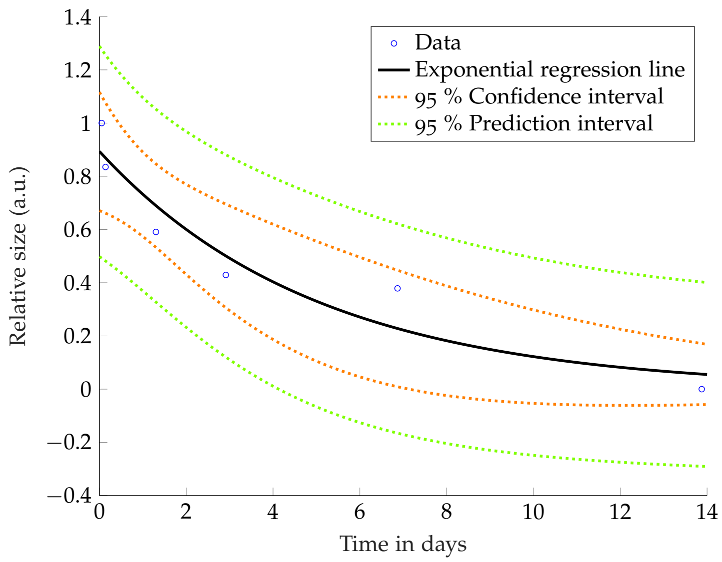

Figure C.15.: Graph of regression model

Table C.44.: Model parameter

Coefficients	a	b
Estimate	0.89364	0.81964
SE	0.080218	0.045661
tStat	11.14	17.95
pValue	0.00036949	$5.6613*10^{-5}$

Parameter estimates and statistically values

Table C.45.: Model parameter

	Confidence interval	Prediction interval
Mean	(0.1188) - (0.48591)	(-0.073577) - (0.67829)
SD	(0.22839) - (0.24249)	(0.22839) - (0.23593)

0.95% Confidence and 0.95% prediction intervals

Table C.46.: Metrics of regression model

R^2	R^2_{adj}	SSE	SSR	SST	RMSE	pValue
0.912	0.89	0.05541	0.58169	0.63102	0.118	0.000545

Statistically values for regression model

P21

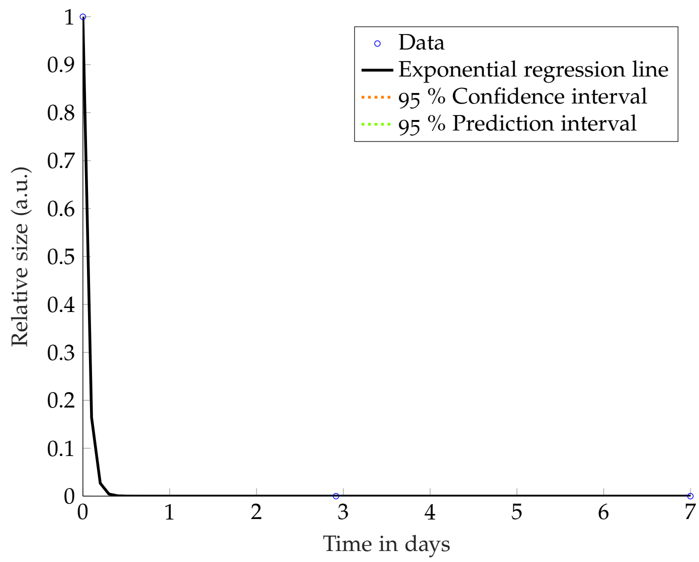

Figure C.16.: Graph of regression model

Table C.47.: Model parameter

Coefficients	a	b
Estimate	1	$1.4151*10^{-8}$
SE	$9.1821*10^{-24}$	0
tStat	$1.0891*10^{23}$	Inf
p-Value	$8.4311*10^{-47}$	0

Parameter estimates and statistically values

Table C.48.: Model parameter

	Confidence interval	Prediction interval
Mean	(NaN) - (NaN)	(NaN) - (NaN)
SD	(NaN) - (NaN)	(NaN) - (NaN)

0.95% confidence and 0.95% prediction intervals

Table C.49.: Metrics of regression model

R^2	R^2_{adj}	SSE	SSR	SST	RMSE	pValue
1	1	$1.6862*10^{-46}$	0.66667	0.66667	$9.18*10^{-24}$	$8.43*10^{-47}$

Statistically values for regression model

P23

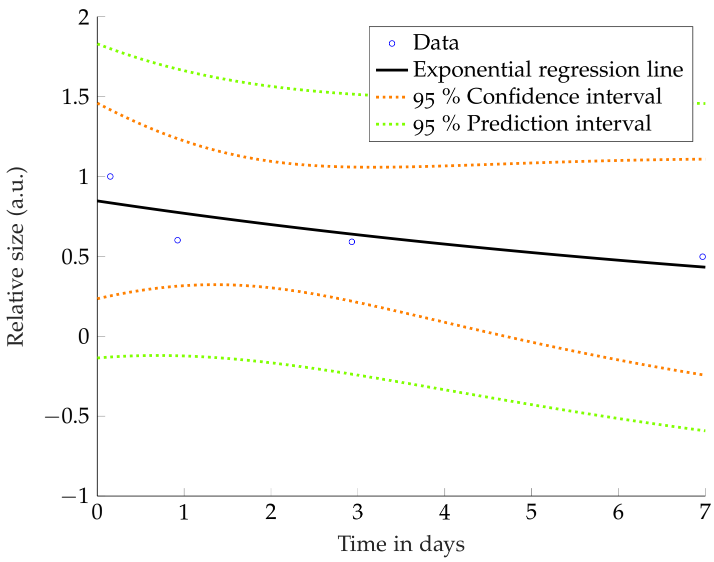

Figure C.17.: Graph of regression model

Table C.50.: Model parameter

Coefficients	a	b
Estimate	0.84712	0.90838
SE	0.14229	0.057875
tStat	5.9534	15.696
p-Value	0.027074	0.0040347

Parameter estimates and statistically values

Table C.51.: Model parameter

	Confidence interval	Prediction interval
Mean	(0.10516) - (1.1288)	(-0.30991) - (1.5439)
SD	(0.19047) - (0.09741)	(0.15808) - (0.098855)

0.95% Confidence and 0.95% prediction intervals

Table C.52.: Metrics of regression model

R^2	R^2_{adj}	SSE	SSR	SST	RMSE	pValue
0.572	0.358	0.063929	0.095103	0.14945	0.179	0.0326

Statistically values for regression model

P24

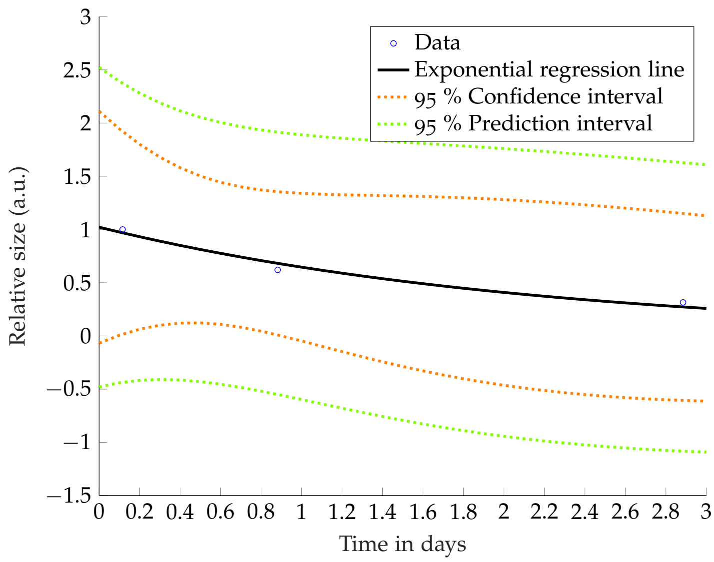

Figure C.18.: Graph of regression model

Table C.53.: Model parameter

Coefficients	a	b
Estimate	1.0214	0.63237
SE	0.085779	0.064831
tStat	11.908	9.7541
p-Value	0.053338	0.065039

Parameter estimates and statistically values

Table C.54.: Model parameter

	Confidence interval	Prediction interval
Mean	(-0.26074) - (1.3765)	(-0.76189) - (1.8777)
SD	(0.27) - (0.22818)	(0.24873) - (0.22503)

0.95% Confidence and 0.95% prediction intervals

Table C.55.: Metrics of regression model

R^2	R^2_{adj}	SSE	SSR	SST	RMSE	pValue
0.972	0.944	0.0066007	0.23554	0.24499	0.0812	0.0667

Statistically values for regression model

P27

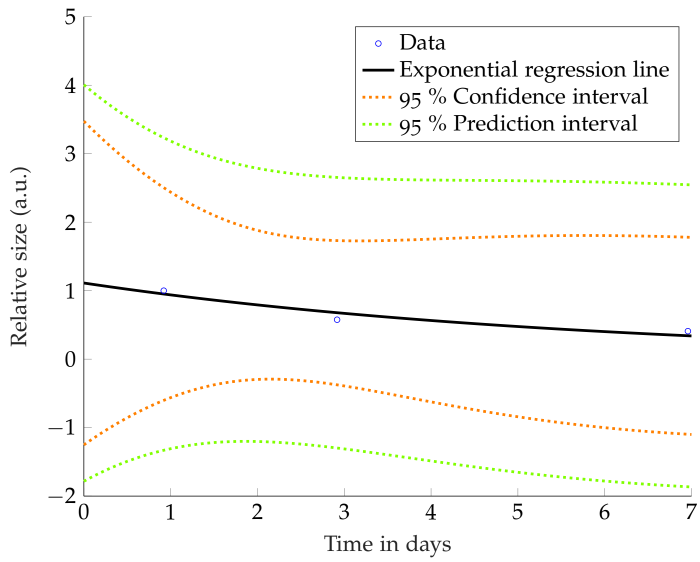

Figure C.19.: Graph of regression model

Table C.56.: Model parameter

Coefficients	a	b
Estimate	1.1118	0.84411
SE	0.18602	0.053461
tStat	5.9768	15.789
p-Value	0.10554	0.040266

Parameter estimates and statistically values

Table C.57.: Model parameter

	Confidence interval	Prediction interval
Mean	(-0.69414) - (1.9983)	(-1.5048) - (2.809)
SD	(0.28425) - (0.43751)	(0.22265) - (0.36155)

0.95% confidence and 0.95% prediction intervals

Table C.58.: Metrics of regression model

R^2	R^2_{adj}	SSE	SSR	SST	RMSE	pValue
0.907	0.814	0.01731	0.1864	0.18572	0.132	0.107

Statistically values for regression model

P28

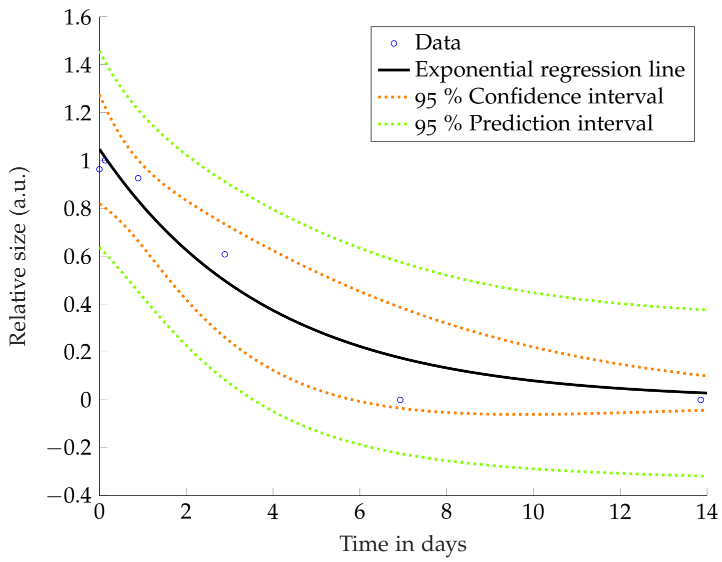

Figure C.20.: Graph of regression model

Table C.59.: Model parameter

Coefficients	a	b
Estimate	1.0472	0.77296
SE	0.082307	0.0516
tStat	12.723	14.98
p-Value	0.00021983	0.00011569

Parameter estimates and statistically values

Table C.60.: Model parameter

	Confidence interval	Prediction interval
Mean	(0.1071) - (0.46168)	(-0.10206) - (0.67084)
SD	(0.24965) - (0.30477)	(0.2622) - (0.28529)

0.95% confidence and 0.95% prediction intervals

Table C.61.: Metrics of regression model

R^2	R^2_{adj}	SSE	SSR	SST	RMSE	pValue
0.946	0.933	0.059878	0.94137	1.1159	0.122	0.000361

Statistically values for regression model

P29

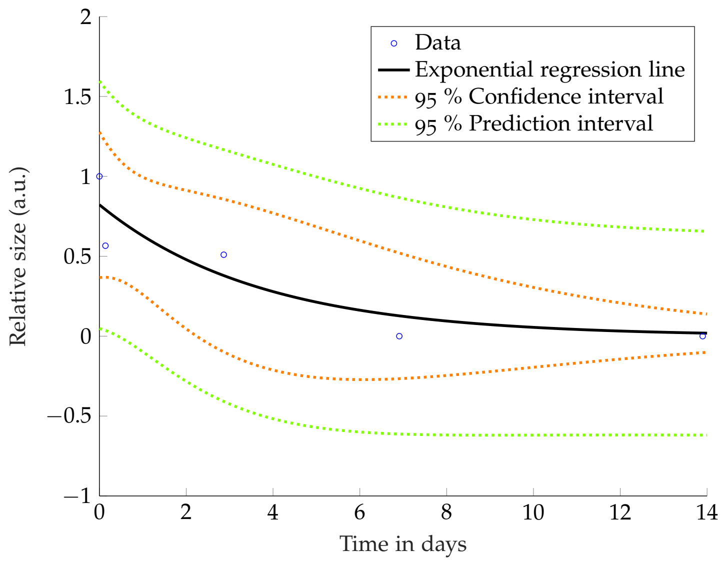

Figure C.21.: Graph of regression model

Table C.62.: Model parameter

Coefficients	a	b
Estimate	0.82232	0.76323
SE	0.14319	0.11271
tStat	5.743	6.7715
p-Value	0.010485	0.0065816

Parameter estimates and statistically values

Table C.63.: Model parameter

	Confidence interval	Prediction interval
Mean	(-0.12519) - (0.55306)	(-0.50634) - (0.93421)
SD	(0.17156) - (0.30131)	(0.18755) - (0.24884)

0.95% confidence and 0.95% prediction intervals

Table C.64.: Metrics of regression model

R^2	R^2_{adj}	SSE	SSR	SST	RMSE	pValue
0.838	0.784	0.11621	0.54883	0.71845	0.197	0.0199

Statistically values for regression model

P30

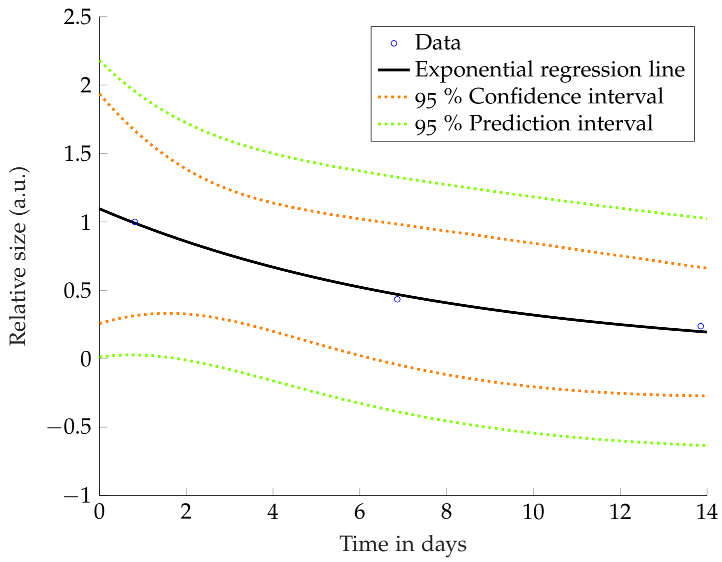

Figure C.22.: Graph of regression model

Table C.65.: Model parameter

Coefficients	a	b
Estimate	1.0959	0.88397
SE	0.066072	0.013763
tStat	16.587	64.23
p-Value	0.038335	0.0099108

Parameter estimates and statistically values

Table C.66.: Model parameter

	Confidence interval	Prediction interval
Mean	(-0.0020752) - (1.0475)	(-0.3425) - (1.3879)
SD	(0.22312) - (0.30373)	(0.23245) - (0.28721)

0.95% confidence and 0.95% prediction intervals

Table C.67.: Metrics of regression model

R^2	R^2_{adj}	SSE	SSR	SST	RMSE	pValue
0.991	0.981	0.002914	0.31318	0.32435	0.054	0.0484

Statistically values for regression model

P31

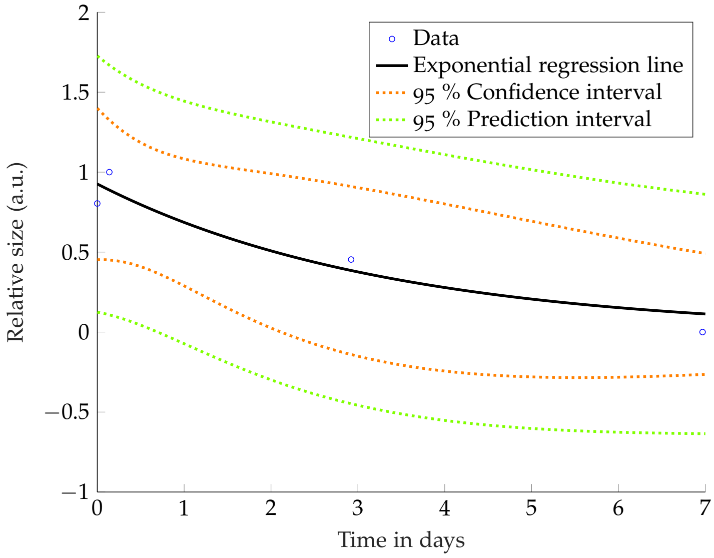

Figure C.23.: Graph of regression model

Table C.68.: Model parameter

Coefficients	a	b
Estimate	0.92585	0.7406
SE	0.11002	0.085502
tStat	8.4154	8.6618
p-Value	0.013828	0.013068

Parameter estimates and statistically values

Table C.69.: Model parameter

	Confidence interval	Prediction interval
Mean	(-0.07603) - (0.85308)	(-0.40841) - (1.1855)
SD	(0.24994) - (0.22511)	(0.24137) - (0.2269)

0.95% confidence and 0.95% prediction intervals

Table C.70.: Metrics of regression model

R^2	R^2_{adj}	SSE	SSR	SST	RMSE	pValue
0.922	0.883	0.045115	0.47024	0.57802	0.15	0.0244

Statistically values for regression model

P32

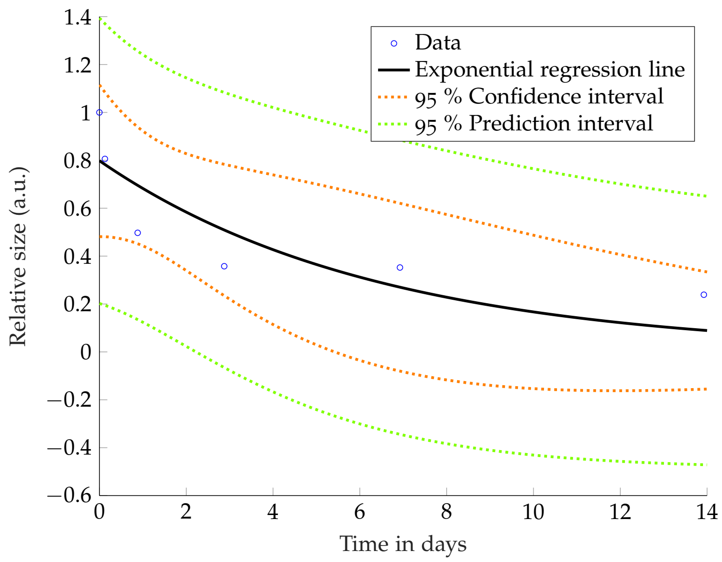

Figure C.24.: Graph of regression model

Table C.71.: Model parameter

Coefficients	a	b
Estimate	0.79831	0.85518
SE	0.11418	0.063838
tStat	6.9915	13.396
p-Value	0.0022021	0.00017959

Parameter estimates and statistically values

Table C.72.: Model parameter

	Confidence interval	Prediction interval
Mean	(0.022367) - (0.62675)	(-0.2646) - (0.91372)
SD	(0.21559) - (0.19015)	(0.20687) - (0.1942)

0.95% confidence and 0.95% prediction intervals

Table C.73.: Metrics of regression model

R^2	R^2_{adj}	SSE	SSR	SST	RMSE	pValue
0.702	0.627	0.13218	0.4261	0.4432	0.182	0.00359

Statistically values for regression model

P34

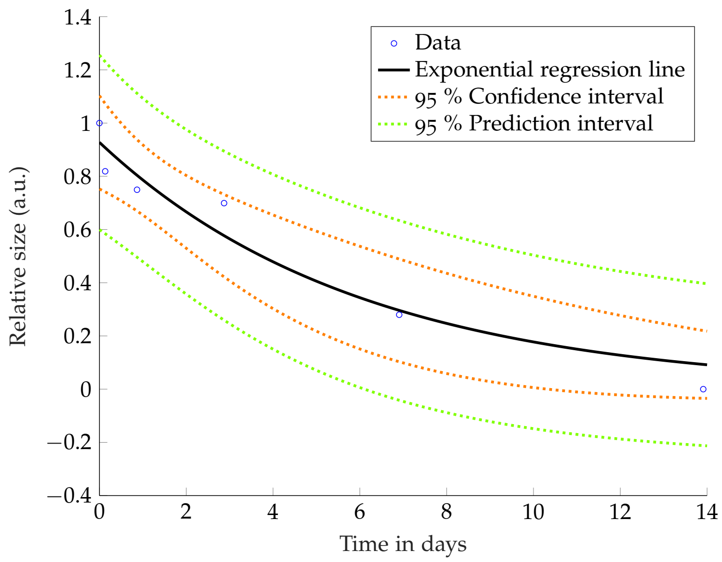

Figure C.25.: Graph of regression model

Table C.74.: Model parameter

Coefficients	a	b
Estimate	0.92762	0.84759
SE	0.063146	0.031773
tStat	14.69	26.677
p-Value	0.00012496	1.1737*10-5

Parameter estimates and statistically values

Table C.75.: Model parameter

	Confidence interval	Prediction interval
Mean	(0.19724) - (0.52714)	(0.039043) - (0.68534)
SD	(0.23989) - (0.23128)	(0.23702) - (0.23269)

0.95% confidence and 0.95% prediction intervals

Table C.76.: Metrics of regression model

R^2	R^2_{adj}	SSE	SSR	SST	RMSE	pValue
0.943	0.929	0.039883	0.59391	0.70218	0.0999	0.000203

Statistically values for regression model

P35

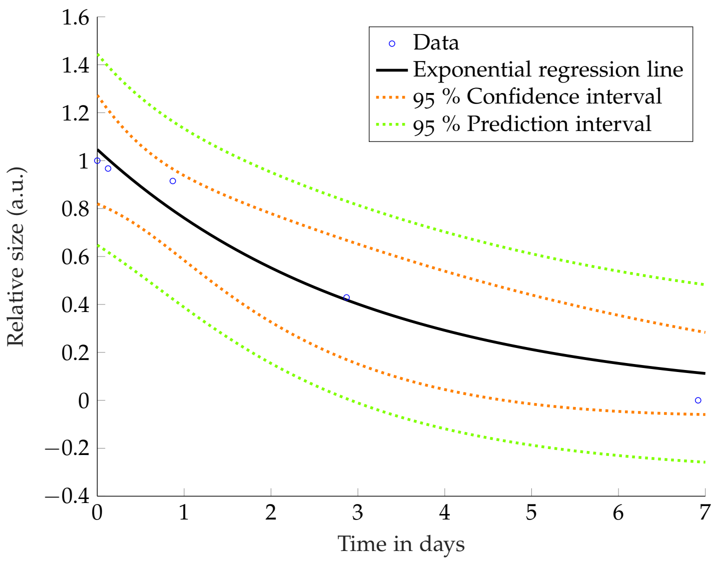

Figure C.26.: Graph of regression model

Table C.77.: Model parameter

Coefficients	a	b
Estimate	1.0466	0.72678
SE	0.07118	0.052733
tStat	14.704	13.782
p-Value	0.00068227	0.00082666

Parameter estimates and statistically values

Table C.78.: Model parameter

	Confidence interval	Prediction interval
Mean	(0.20461) - (0.63668)	(0.027039) - (0.81425)
SD	(0.27507) - (0.26015)	(0.27065) - (0.26269)

0.95% confidence and 0.95% prediction intervals

Table C.79.: Metrics of regression model

R^2	R^2_{adj}	SSE	SSR	SST	RMSE	pValue
0.958	0.944	0.031908	0.64158	0.76384	0.103	0.00112

Statistically values for regression model

P36

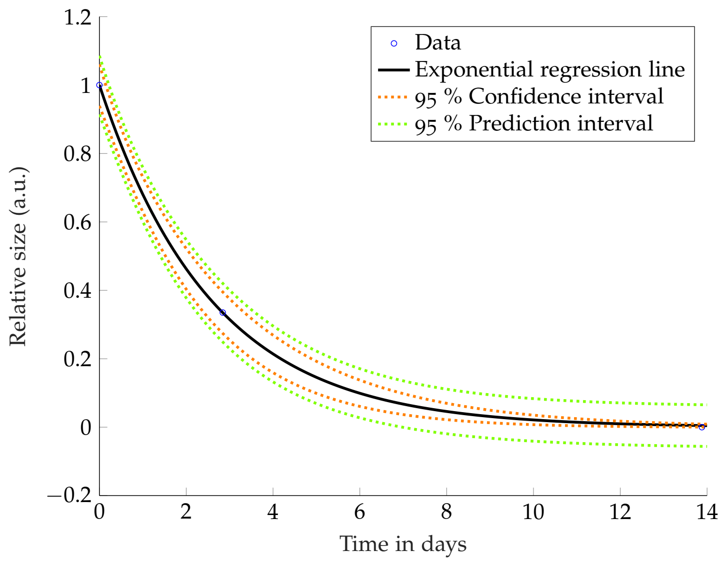

Figure C.27.: Graph of regression model

Table C.80.: Model parameter

Coefficients	a	b
Estimate	1.0001	0.68029
SE	0.0047726	0.0035915
tStat	209.55	189.41
p-Value	0.0030381	0.003361

Parameter estimates and statistically values

Table C.81.: Model parameter

	Confidence interval	Prediction interval
Mean	(0.15472) - (0.219)	(0.11593) - (0.25779)
SD	(0.233) - (0.26243)	(0.24047) - (0.25434)

0.95% confidence and 0.95% prediction intervals

Table C.82.: Metrics of regression Model

R^2	R^2_{adj}	SSE	SSR	SST	RMSE	pValue
1	1	$2.278*10^{-5}$	0.5141	0.51815	0.00477	0.00453

Statistically values for regression model

P38

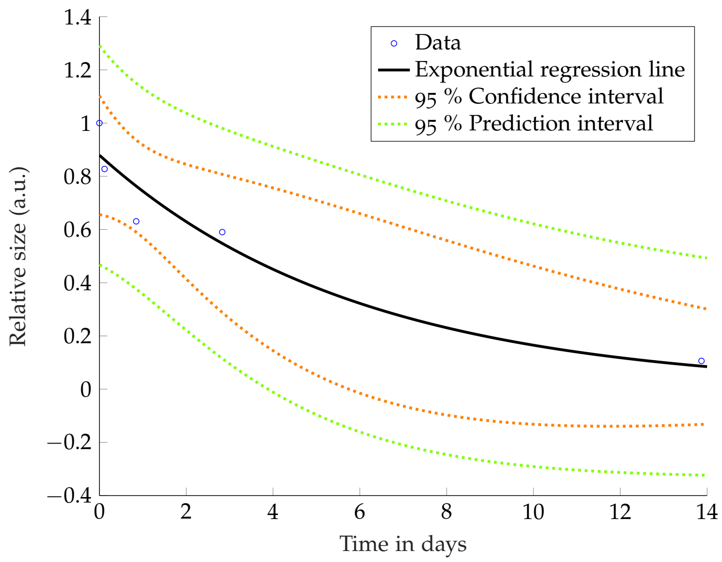

Figure C.28.: Graph of regression model

Table C.83.: Model parameter

Coefficients	a	b
Estimate	0.87938	0.84604
SE	0.07019	0.050683
tStat	12.529	16.693
p-Value	0.0010962	0.00175

Parameter estimates and statistically values

Table C.84.: Model parameter

	Confidence interval	Prediction interval
Mean	(0.063208) - (0.6179)	(-0.10472) - (0.78583)
SD	(0.25072) - (0.20402)	(0.23796) - (0.21112)

0.95% confidence and 0.95% prediction intervals

Table C.85.: Metrics of regression model

R^2	R^2_{adj}	SSE	SSR	SST	RMSE	pValue
0.922	0.895	0.035461	0.43599	0.45186	0.109	0.00175

Statistically values for regression model

P39

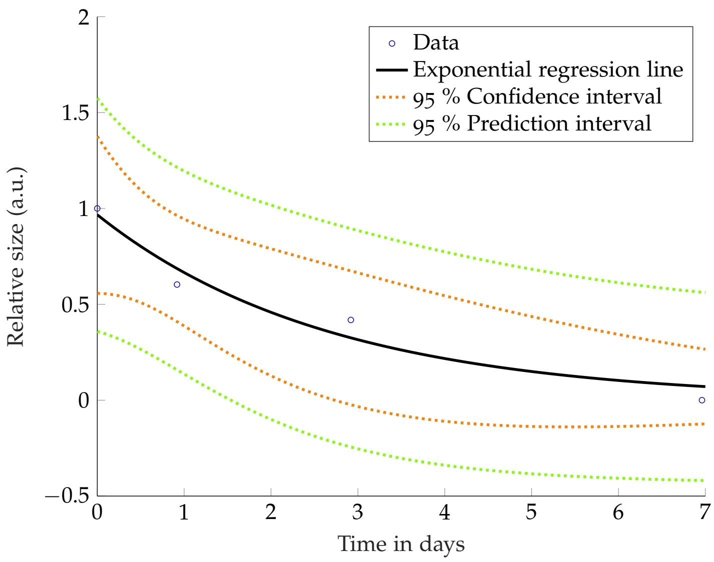

Figure C.29.: Graph of regression model

Table C.86.: Model parameter

Coefficients	a	b
Estimate	0.96694	0.68849
SE	0.095233	0.067097
tStat	10.153	10.261
p-Value	0.0095612	0.0093644

Parameter estimates and statistically values

Table C.87.: Model parameter

	Confidence interval	Prediction interval
Mean	(0.047037) - (0.64389)	(-0.19583) - (0.88676)
SD	(0.23332) - (0.27827)	(0.2413) - (0.26548)

0.95% Confidence and 0.95% prediction intervals

Table C.88.: Metrics of regression Model

R^2	R^2_{adj}	SSE	SSR	SST	RMSE	pValue
0.958	0.937	0.021864	0.46612	0.51719	0.105	0.0142

Statistically values for regression model

P40

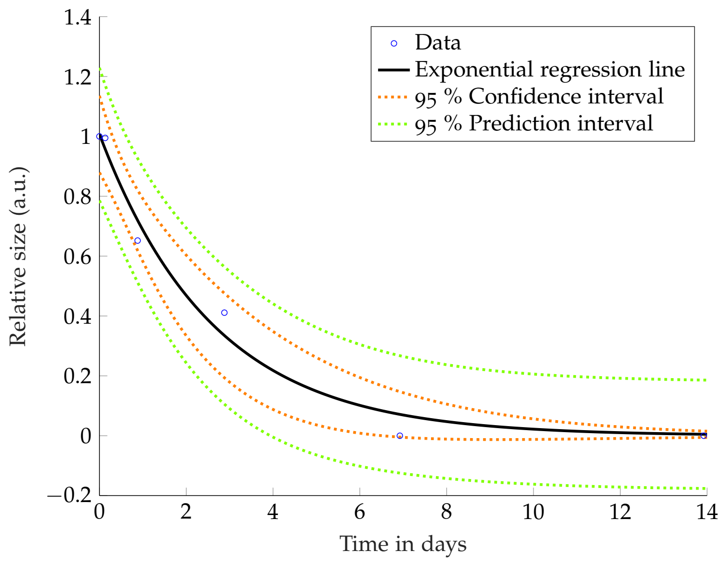

Figure C.30.: Graph of regression model

Table C.89.: Model parameter

Coefficients	a	b
Estimate	1.0076	0.68208
SE	0.046179	0.039659
tStat	21.819	17.199
p-Value	$2.6107*10^{-5}$	$6.7058*10^{-5}$

Parameter estimates and statistically values

Table C.90.: Model parameter

	Confidence interval	Prediction interval
Mean	(0.11479) - (0.26422)	(-0.010474) - (0.38948)
SD	(0.22275) - (0.28108)	(0.23891) - (0.26085)

0.95% confidence and 0.95% prediction intervals

Table C.91.: Metrics of regression model

R^2	R^2_{adj}	SSE	SSR	SST	RMSE	pValue
0.983	0.979	0.016953	0.97008	1.0254	0.0651	$4.3*10^{-5}$

Statistically values for regression model

C.3. Water Fraction vs Time

P6

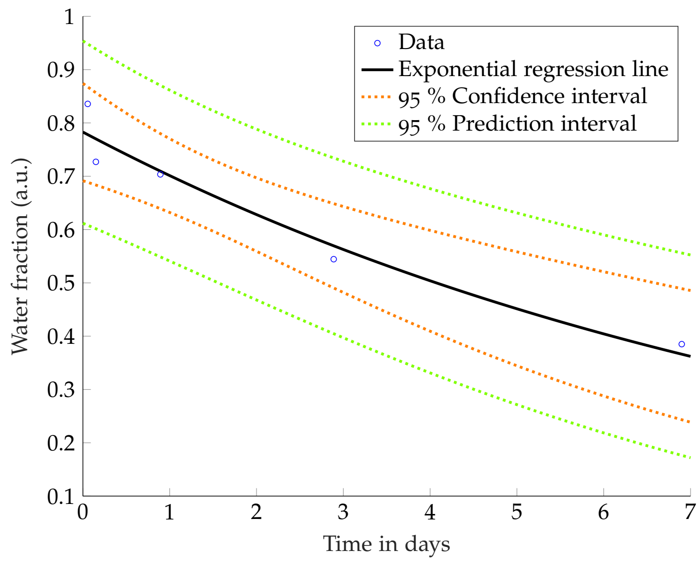

Figure C.31.: Graph of regression model

Table C.92.: Model parameter

Coefficients	a	b
Estimate	0.78287	0.89572
SE	0.028693	0.01565
tStat	27.285	57.234
p-Value	0.00010805	1.175*10^−5

Parameter estimates and statistically values

Table C.93.: Model parameter

	Confidence interval	Prediction interval
Mean	(0.45435) - (0.6379)	(0.37411) - (0.71814)
SD	(0.14042) - (0.10732)	(0.13262) - (0.11461)

0.95% confidence and 0.95% prediction intervals

Table C.94.: Metrics of regression model

R^2	R^2_{adj}	SSE	SSR	SST	RMSE	pValue
0.95	0.933	0.0061945	0.12075	0.12404	0.0454	0.000153

Statistically values for regression model

P8

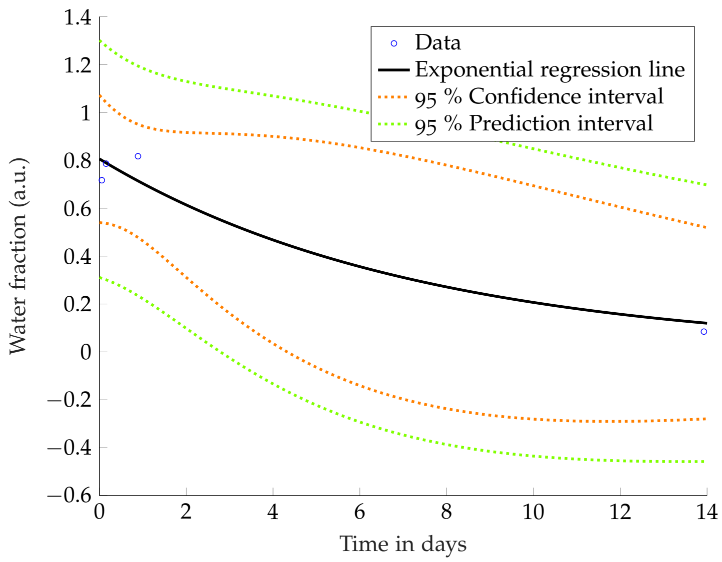

Figure C.32.: Graph of regression model

Table C.95.: Model parameter

Coefficients	a	b
Estimate	0.80599	0.87272
SE	0.061885	0.049609
tStat	13.024	17.592
p-Value	0.0058437	0.0032157

Parameter estimates and statistically values

Table C.96.: Model parameter

	Confidence interval	Prediction interval
Mean	(-0.066453) - (0.78792)	(-0.23993) - (0.9614)
SD	(0.26687) - (0.13895)	(0.24121) - (0.15565)

0.95% confidence and 0.95% prediction intervals

Table C.97.: Metrics of regression model

R^2	R^2_{adj}	SSE	SSR	SST	RMSE	pValue
0.948	0.922	0.018829	0.3182	0.36088	0.097	0.0104

Statistically values for regression model

P9

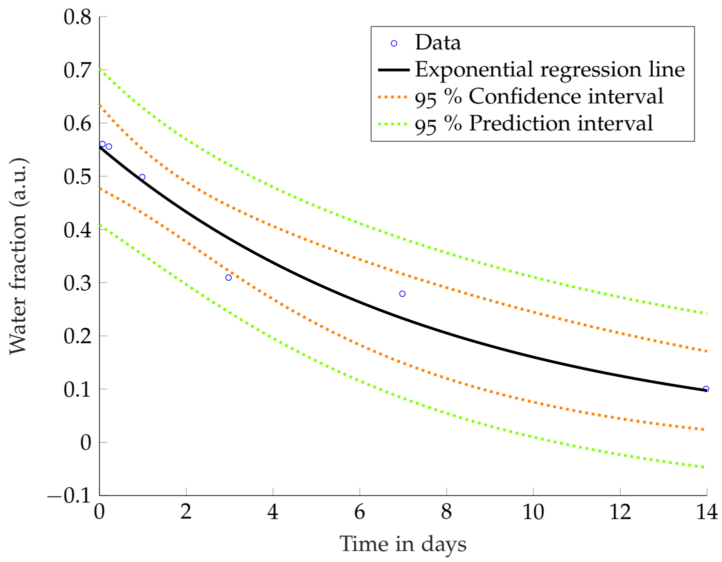

Figure C.33.: Graph of regression model

Table C.98.: Model parameter

Coefficients	a	b
Estimate	0.5554	0.88306
SE	0.028154	0.018604
tStat	19.727	47.465
p-Value	$3.8949*10^{-5}$	$1.178*10^{-6}$

Parameter estimates and statistically values

Table C.99.: Model parameter

	Confidence interval	Prediction interval
Mean	(0.18818) - (0.33886)	(0.11793) - (0.40912)
SD	(0.13815) - (0.1234)	(0.13433) - (0.127)

0.95% confidence and 0.95% prediction intervals

Table C.100.: Metrics of regression model

R^2	R^2_{adj}	SSE	SSR	SST	RMSE	pValue
0.953	0.941	0.0080182	0.16849	0.17077	0.0448	$5.77*10^{-5}$

Statistically values for regression model

P10

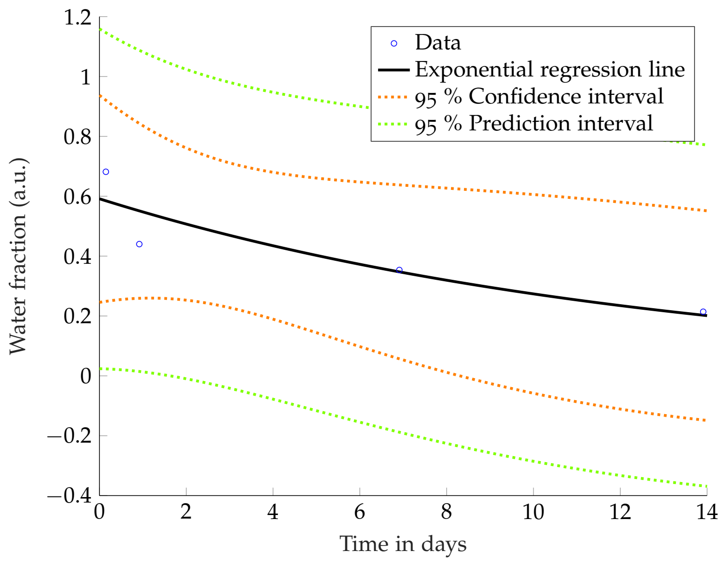

Figure C.34.: Graph of regression model

Table C.101.: Model parameter

Coefficients	a	b
Estimate	0.59157	0.92587
SE	0.080418	0.030257
tStat	7.3562	30.6
p-Value	0.017983	0.0010662

Parameter estimates and statistically values

Table C.102.: Model parameter

	Confidence interval	Prediction interval
Mean	(0.062416) - (0.66205)	(-0.17949) - (0.90395)
SD	(0.14258) - (0.09007)	(0.12871) - (0.099034)

0.95% confidence and 0.95% prediction intervals

Table C.103.: Metrics of regression model

R^2	R^2_{adj}	SSE	SSR	SST	RMSE	pValue
0.881	0.716	0.021881	0.96885	0.1156	0.105	0.0264

Statistically values for regression model

P11

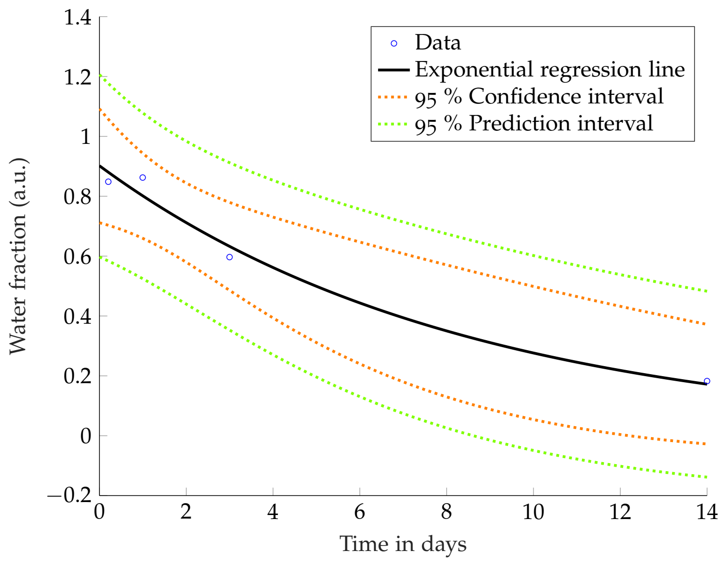

Figure C.35.: Graph of regression model

Table C.104.: Model parameter

Coefficients	a	b
Estimate	0.90189	0.88845
SE	0.044243	0.018656
tStat	20.385	47.623
p-Value	0.0023978	0.00044063

Parameter estimates and statistically values

Table C.105.: Model parameter

	Confidence interval	Prediction interval
Mean	(0.24905) - (0.63368)	(0.13456) - (0.74817)
SD	(0.23548) - (0.18293)	(0.22466) - (0.1929)

0.95% Confidence and 0.95% prediction intervals

Table C.106.: Metrics of regression model

R^2	R^2_{adj}	SSE	SSR	SST	RMSE	pValue
0.98	0.97	0.0061075	0.30138	0.30286	0.0553	0.0033

Statistically values for regression model

P12

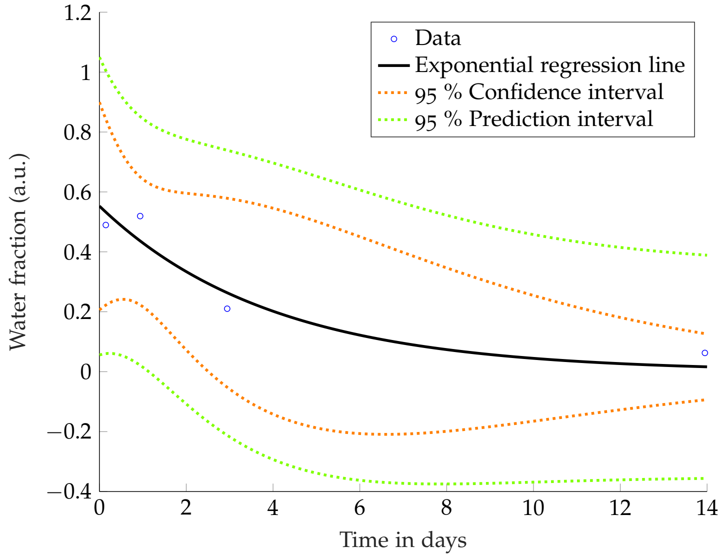

Figure C.36.: Graph of regression model

Table C.107.: Model parameter

Coefficients	a	b
Estimate	0.55279	0.7774
SE	0.080597	0.091847
tStat	6.8587	8.4642
p-Value	0.020603	0.013673

Parameter estimates and statistically values

Table C.108.: Model parameter

	Confidence interval	Prediction interval
Mean	(-0.9727) - (0.40356)	(-0.28638) - (0.59266)
SD	(0.13278) - (0.18624)	(0.13421) - (0.16371)

0.95% confidence and 0.95% prediction intervals

Table C.109.: Metrics of regression model

R^2	R^2_{adj}	SSE	SSR	SST	RMSE	pValue
0.907	0.86	0.013693	0.14678	0.15414	0.0827	0.0246

Statistically values for regression model

P13

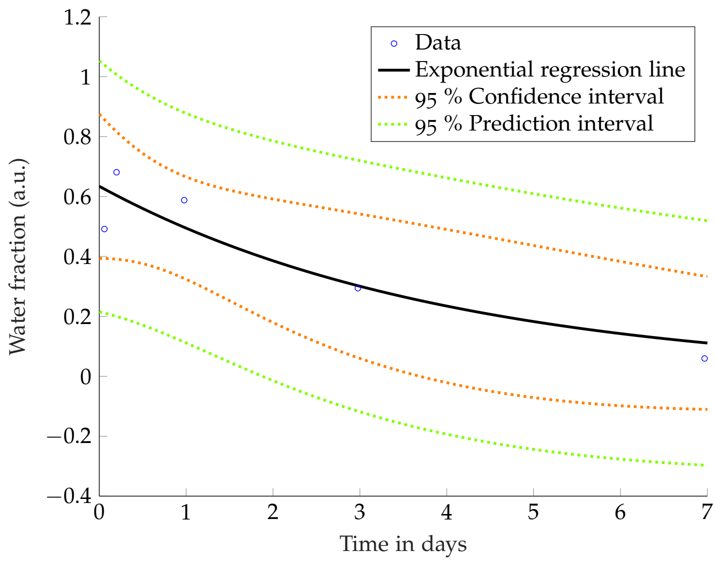

Figure C.37.: Graph of regression model

Table C.110.: Model parameter

Coefficients	a	b
Estimate	0.63426	0.77971
SE	0.075672	0.075678
tStat	8.3817	10.303
p-Value	0.0035617	0.0019501

Parameter estimates and statistically values

Table C.111.: Model parameter

	Confidence interval	Prediction interval
Mean	(0.074473) - (0.52826)	(-0.11049) - (0.71323)
SD	(0.17256) - (0.13189)	(0.16218) - (0.14049)

0.95% confidence and 0.95% prediction intervals

Table C.112.: Metrics of regression model

R^2	R^2_{adj}	SSE	SSR	SST	RMSE	pValue
0.859	0.812	0.034831	0.19023	0.24722	0.108	0.00533

Statistically values for regression model

P14

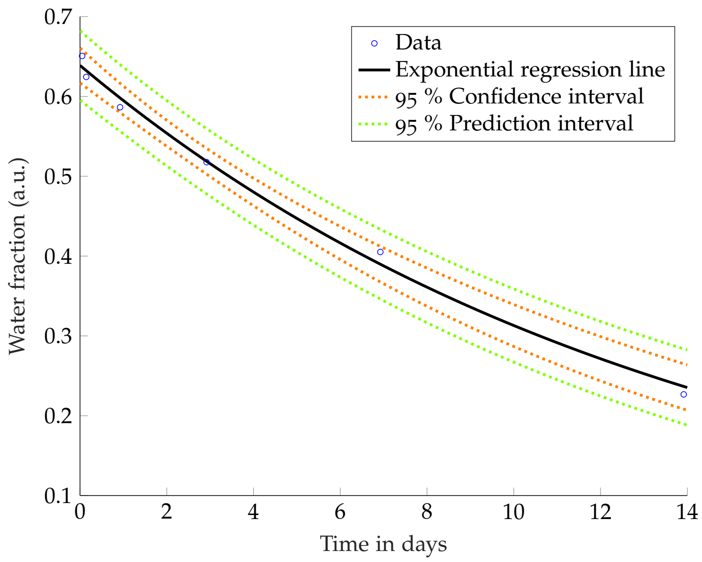

Figure C.38.: Graph of regression model

Table C.113.: Model parameter

Coefficients	a	b
Estimate	0.63882	0.93115
SE	0.0078923	0.0032346
tStat	80.943	287.87
p-Value	$1.3964*10^{-7}$	$8.7358*10^{-10}$

Parameter estimates and statistically values

Table C.114.: Model parameter

	Confidence interval	Prediction interval
Mean	(0.3819) - (0.42666)	(0.3604) - (0.44817)
SD	(0.12076) - (0.11291)	(0.11883) - (0.11482)

0.95% confidence and 0.95% prediction intervals

Table C.115.: Metrics of regression model

R^2	R^2_{adj}	SSE	SSR	SST	RMSE	pValue
0.994	0.993	0.0007322	0.12759	0.12963	$1.99*10^{-7}$	

Statistically values for regression model

P15

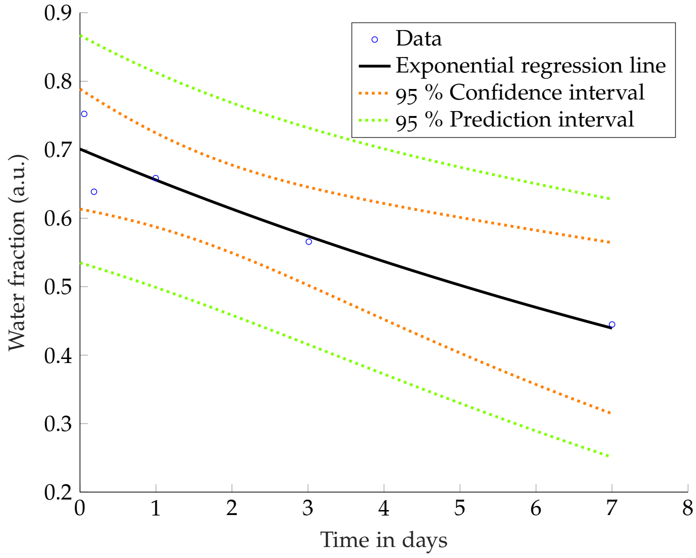

Figure C.39.: Graph of regression model

Table C.116.: Model parameter

Coefficients	a	b
Estimate	0.701	0.93546
SE	0.027541	0.014182
tStat	25.453	65.96
p-Value	0.000133	$7.678*10^{-6}$

Parameter estimates and statistically values

Table C.117.: Model parameter

	Confidence interval	Prediction interval
Mean	(0.47368) - (0.64676)	(0.39393) - (0.72651)
SD	(0.093715) - (0.06181)	(0.085926) - (0.0685)

0.95% Confidence and 0.95% prediction intervals

Table C.118.: Metrics of regression Model

R^2	R^2_{adj}	SSE	SSR	SST	RMSE	pValue
0.888	0.851	0.005895	0.04713	0.052663	0.0443	0.000169

Statistically values for regression model

P16

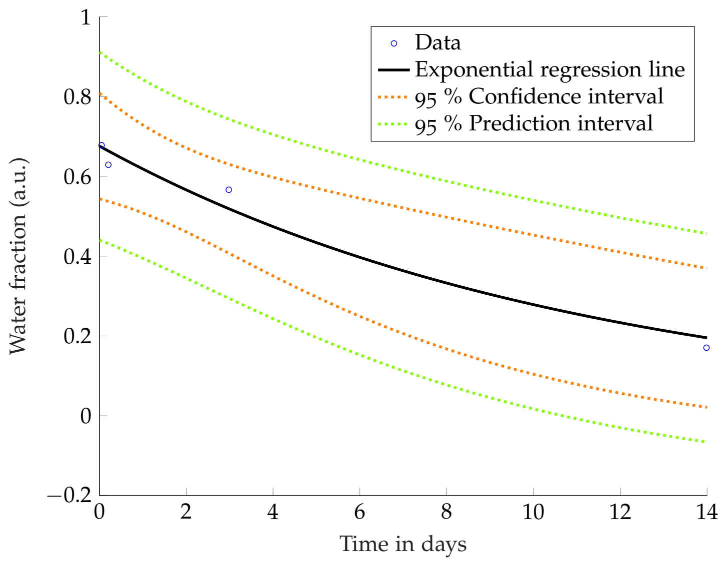

Figure C.40.: Graph of regression model

Table C.119.: Model parameter

Coefficients	a	b
Estimate	0.67574	0.91517
SE	0.030774	0.014516
tStat	21.958	63.044
p-Value	0.0020675	0.00025151

Parameter estimates and statistically values

Table C.120.: Model parameter

	Confidence interval	Prediction interval
Mean	(0.2387) - (0.53619)	(0.14145) - (0.63344)
SD	(0.16381) - (0.1138)	(0.15343) - (0.12379)

0.95% confidence and 0.95% prediction intervals

Table C.121.: Metrics of regression model

R^2	R^2_{adj}	SSE	SSR	SST	RMSE	pValue
0.975	0.962	0.0040977	0.149	0.1607	0.0453	0.0034

Statistically values for regression model

P17

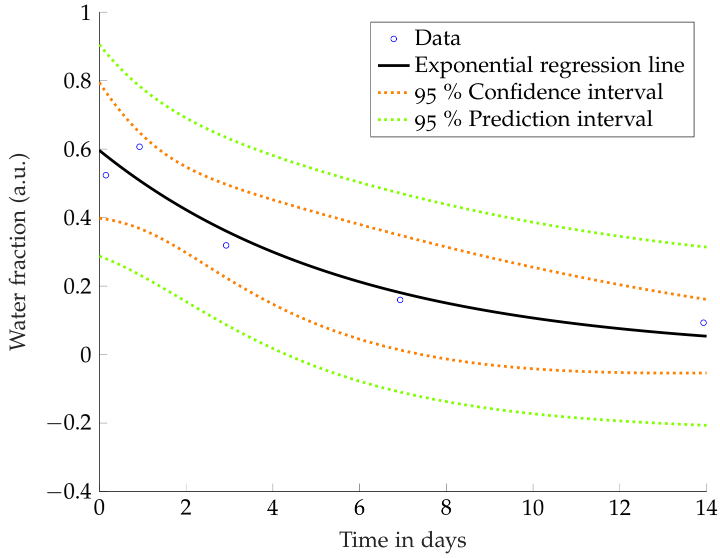

Figure C.41.: Graph of regression model

Table C.122.: Model parameter

Coefficients	a	b
Estimate	0.59636	0.84199
SE	0.062266	0.04108
tStat	9.5776	20.496
p-Value	0.002415	0.00025394

Parameter estimates and statistically values

Table C.123.: Model parameter

	Confidence interval	Prediction interval
Mean	(0.079613) - (0.37257)	(-0.053058) - (0.50524)
SD	(0.14886) - (0.15704)	(0.15) - (0.1543)

0.95% Confidence and 0.95% prediction intervals

Table C.124.: Metrics of regression model

R^2	R^2_{adj}	SSE	SSR	SST	RMSE	pValue
0.916	0.888	0.016651	0.19385	0.19897	0.0745	0.00313

Statistically values for regression model

P18

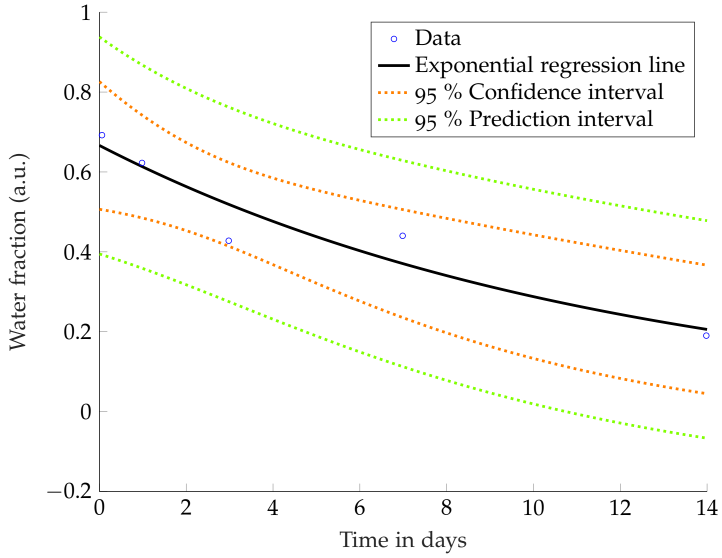

Figure C.42.: Graph of regression model

Table C.125.: Model parameter

Coefficients	a	b
Estimate	0.66634	0.9195
SE	0.050215	0.018492
tStat	13.27	49.724
p-Value	0.00092487	$1.7912*10^{-5}$

Parameter estimates and statistically values

Table C.126.: Model parameter

	Confidence interval	Prediction interval
Mean	(0.25538) - (0.52919)	(0.13286) - (0.65171)
SD	(0.14831) - (0.11907)	(0.14085) - (0.12545)

0.95% confidence and 0.95% prediction intervals

Table C.127.: Metrics of regression model

R^2	R^2_{adj}	SSE	SSR	SST	RMSE	pValue
0.907	0.876	0.014295	0.13969	0.15343	0.069	0.00118

Statistically values for regression model

P19

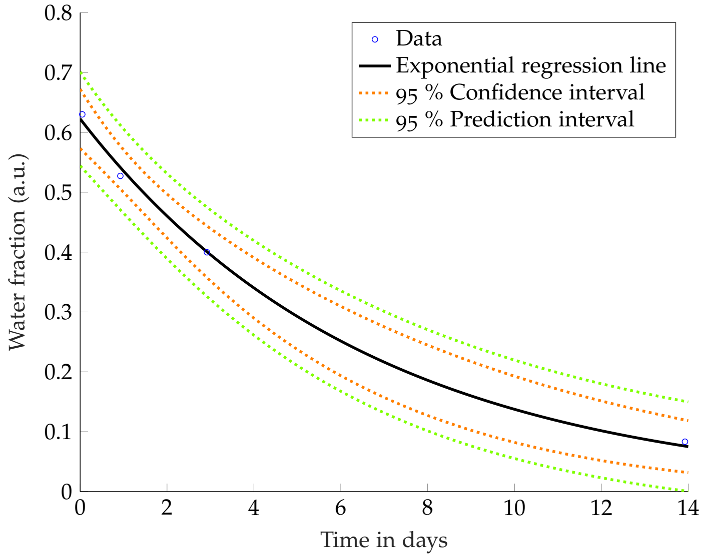

Figure C.43.: Graph of regression model

Table C.128.: Model parameter

Coefficients	a	b
Estimate	0.62258	0.85977
SE	0.01151	0.0088122
tStat	54.089	97.567
p-Value	0.00034163	0.00010503

Parameter estimates and statistically values

Table C.129.: Model parameter

	Confidence interval	Prediction interval
Mean	(0.20925) - (0.30972)	(0.18038) - (0.33858)
SD	(0.15918) - (0.1502)	(0.15731) - (0.15192)

0.95% confidence and 0.95% prediction intervals

Table C.130.: Metrics of regression model

R^2	R^2_{adj}	SSE	SSR	SST	RMSE	pValue
0.998	0.996	0.00039945	0.17219	0.16901	0.0141	0.000475

Statistically values for regression model

P20

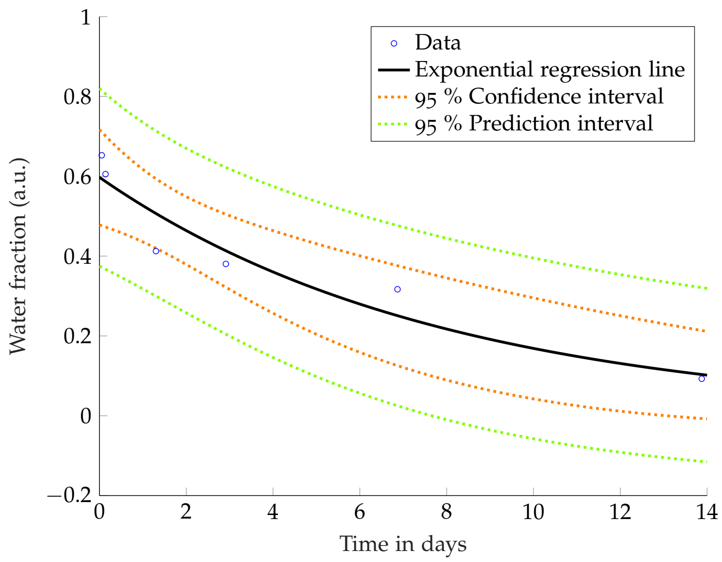

Figure C.44.: Graph of regression model

Table C.131.: Model parameter

Coefficients	a	b
Estimate	0.59748	0.88127
SE	0.043046	0.026416
tStat	13.88	33.361
p-Value	0.00015621	$4.8153*10^{-6}$

Parameter estimates and statistically values

Table C.132.: Model parameter

	Confidence interval	Prediction interval
Mean	(0.16747) - (0.39374)	(0.061016) - (0.50019)
SD	(0.15198) - (0.13119)	(0.14649) - (0.1362)

0.95% confidence and 0.95% prediction intervals

Table C.133.: Metrics of regression model

R^2	R^2_{adj}	SSE	SSR	SST	RMSE	pValue
0.912	0.89	0.018301	0.19369	0.20725	0.0676	0.000226

Statistically values for regression model

P21

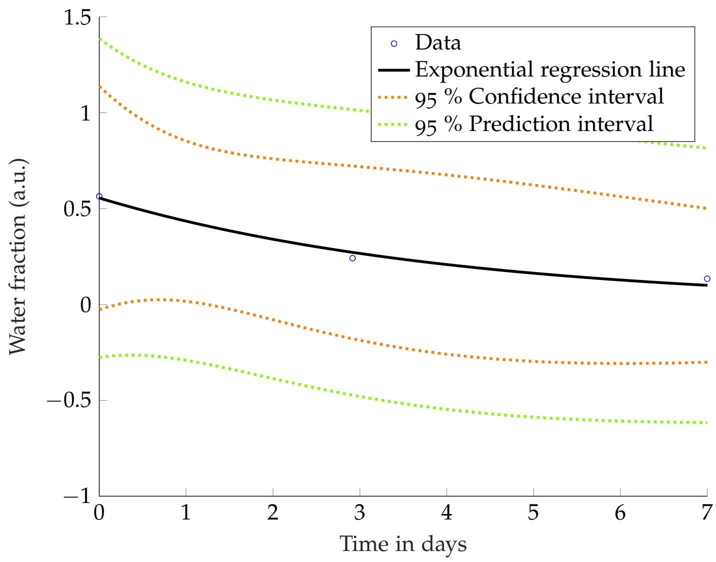

Figure C.45.: Graph of regression model

Table C.134.: Model parameter

Coefficients	a	b
Estimate	0.55516	0.78259
SE	0.045845	0.038306
tStat	12.11	20.43
pValue	0.052453	0.031136

Paramter estimates and statistically values

Table C.135.: Model parameter

	Confidence interval	Prediction interval
Mean	(-0.18064) - (0.71313)	(-0.47658) - (1.0091)
SD	(0.12556) - (0.14478)	(0.12654) - (0.13928)

0.95% confidence and 0.95% prediction intervals

Table C.136.: Metrics of regression model

R^2	R^2_{adj}	SSE	SSR	SST	RMSE	pValue
0.978	0.956	0.0021767	0.10579	0.10001	0.0467	0.0743

Statistically values for regression model

P23

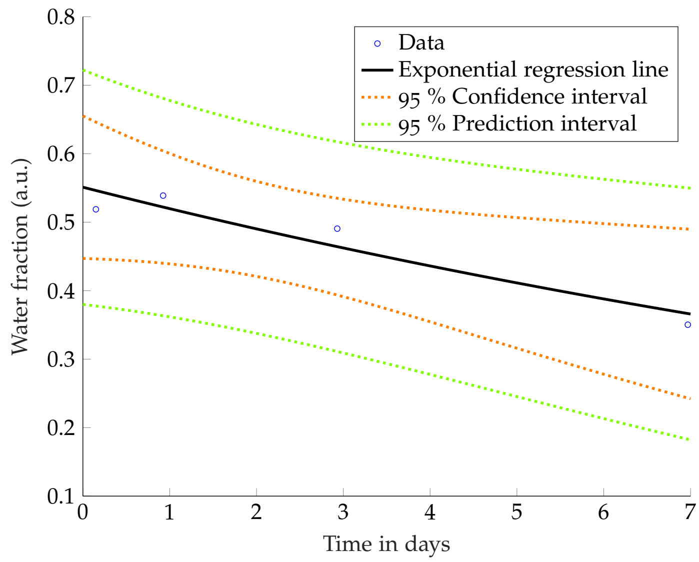

Figure C.46.: Graph of regression model

Table C.137.: Model parameter

Coefficients	a	b
Estimate	0.55108	0.94318
SE	0.024191	0.013536
tStat	22.78	69.681
p-Value	0.0019215	0.00020589

Parameter estimates and statistically values

Table C.138.: Model parameter

	Confidence interval	Prediction interval
Mean	(0.36358) - (0.541)	(0.28945) - (0.61512)
SD	(0.066137) - (0.046157)	(0.060852) - (0.049191)

0.95% confidence and 0.95% prediction intervals

Table C.139.: Metrics of regression model

R^2	R^2_{adj}	SSE	SSR	SST	RMSE	pValue
0.909	0.863	0.001994	0.19163	0.021793	0.0316	0.00216

Statistically values for regression model

P24

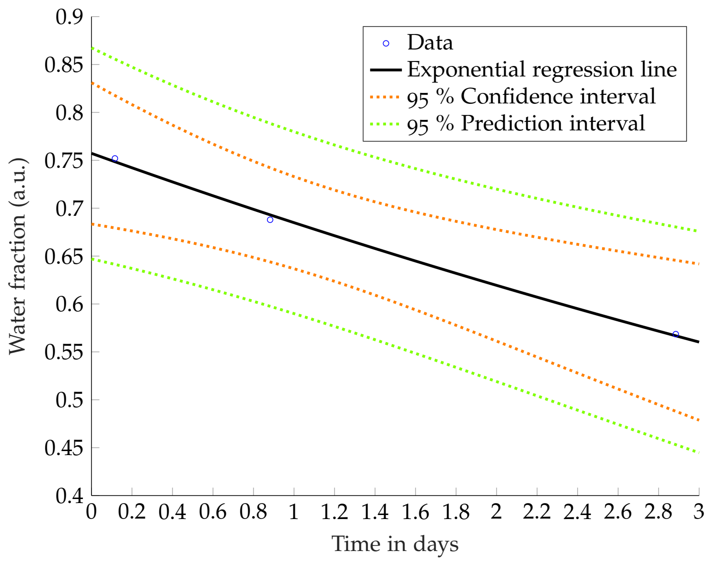

Figure C.47.: Graph of regression model

Table C.140.: Model parameter

Coefficients	a	b
Estimate	0.75726	0.90444
SE	0.0058053	0.0046298
tStat	130.44	195.35
p-Value	0.0048804	0.0032588

Parameter estimates and statistically values

Table C.141.: Model parameter

	Confidence interval	Prediction interval
Mean	(0.59389) - (0.71408)	(0.55211) - (0.75586)
SD	(0.064758) - (0.056111)	(0.062641) - (0.057254)

0.95% Confidence and 0.95% prediction intervals

Table C.142.: Metrics of regression model

R^2	R^2_{adj}	SSE	SSR	SST	RMSE	pValue
0.998	0.995	$4.15{*}10^{-5}$	0.017347	0.017333	0.00644	0.00552

Statistically values for regression model

P28

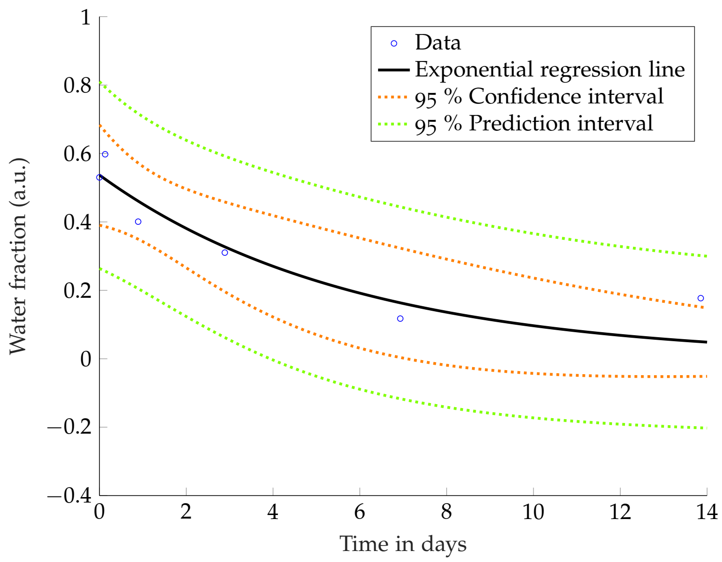

Figure C.48.: Graph of regression model

Table C.143.: Model parameter

Coefficients	a	b
Estimate	0.53708	0.84232
SE	0.052842	0.047077
tStat	10.164	17.892
p-Value	0.00052769	$5.7346*10^{-5}$

Parameter estimates and statistically values

Table C.144.: Model parameter

	Confidence interval	Prediction interval
Mean	(0.067994) - (0.33995)	(-0.06405) - (0.47199)
SD	(0.13979) - (0.13621)	(0.13798) - (0.13608)

0.95% confidence and 0.95% prediction intervals

Table C.145.: Metrics of regression model

R^2	R^2_{adj}	SSE	SSR	SST	RMSE	pValue
0.848	0.811	0.0027542	0.18177	0.20393	0.083	0.00858

Statistically values for regression model

P29

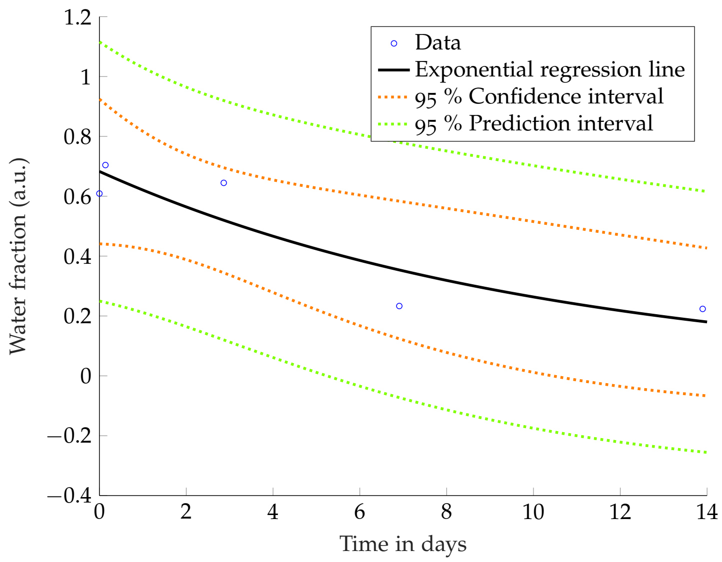

Figure C.49.: Graph of regression model

Table C.146.: Model parameter

Coefficients	a	b
Estimate	0.68286	0.9092
SE	0.07598	0.030761
tStat	8.9873	29.557
p-Value	0.0029077	$8.5056*10^{-5}$

Parameter estimates and statistically values

Table C.147.: Model parameter

	Confidence interval	Prediction interval
Mean	(0.15415) - (0.6011)	(-0.046081) - (0.80133)
SD	(0.16892) - (0.12242)	(0.15709) - (0.13281)

0.95% confidence and 0.95% prediction intervals

Table C.148.: Metrics of regression model

R^2	R^2_{adj}	SSE	SSR	SST	RMSE	pValue
0.827	0.769	0.038206	0.18514	0.22063	0.113	0.00457

Statistically values for regression model

P31

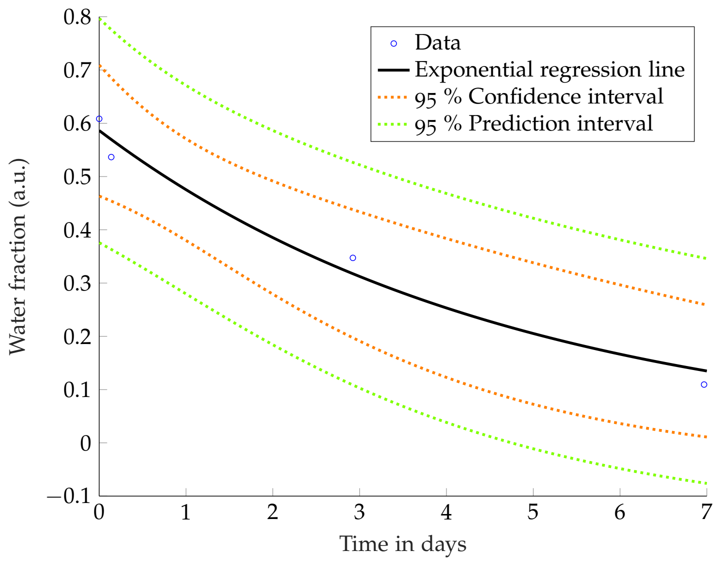

Figure C.50.: Graph of regression model

Table C.149.: Model parameter

Coefficients	a	b
Estimate	0.58635	0.81069
SE	0.028591	0.026415
tStat	20.508	30.69
p-Value	0.0023692	0.00106

Parameter estimates and statistically values

Table C.150.: Model parameter

	Confidence interval	Prediction interval
Mean	(0.18862) - (0.42745)	(0.099318) - (0.51676)
SD	(0.14199) - (0.12056)	(0.13714) - (0.12512)

0.95% confidence and 0.95% prediction intervals

Table C.151.: Metrics of regression model

R^2	R^2_{adj}	SSE	SSR	SST	RMSE	pValue
0.979	0.968	0.0031533	0.14003	0.14926	0.0397	0.00399

Statistically values for regression model

P32

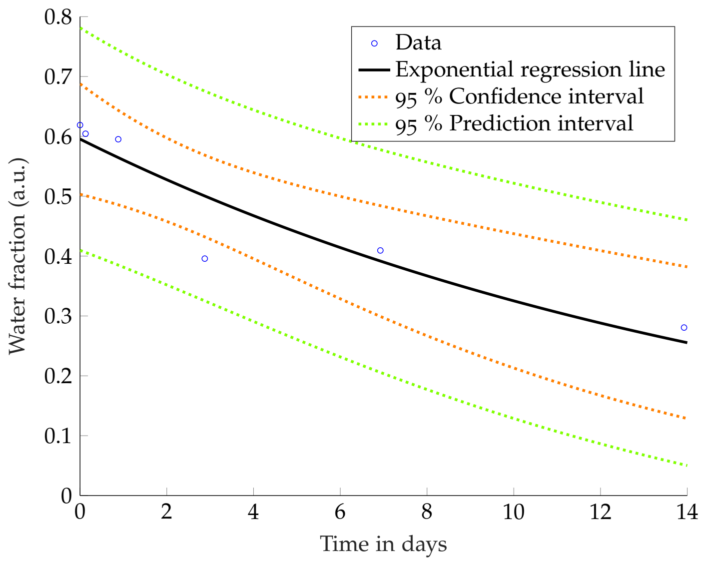

Figure C.51.: Graph of regression model

Table C.152.: Model parameter

Coefficients	a	b
Estimate	0.59546	0.94131
SE	0.033228	0.013545
tStat	17.921	69.495
p-Value	$5.698810*^{-5}$	$2.5689*10^{-7}$

Parameter estimates and statistically values

Table C.153.: Model parameter

	Confidence interval	Prediction interval
Mean	(0.30652) - (0.49716)	(0.21366) - (0.59002)
SD	(0.11696) - (0.081208)	(0.10797) - (0.089606)

0.95% confidence and 0.95% prediction intervals

Table C.154.: Metrics of regression model

R^2	R^2_{adj}	SSE	SSR	SST	RMSE	pValue
0.865	0.831	0.013509	0.090895	0.099758	0.0581	$8.05*10^{-5}$

Statistically values for regression model

P34

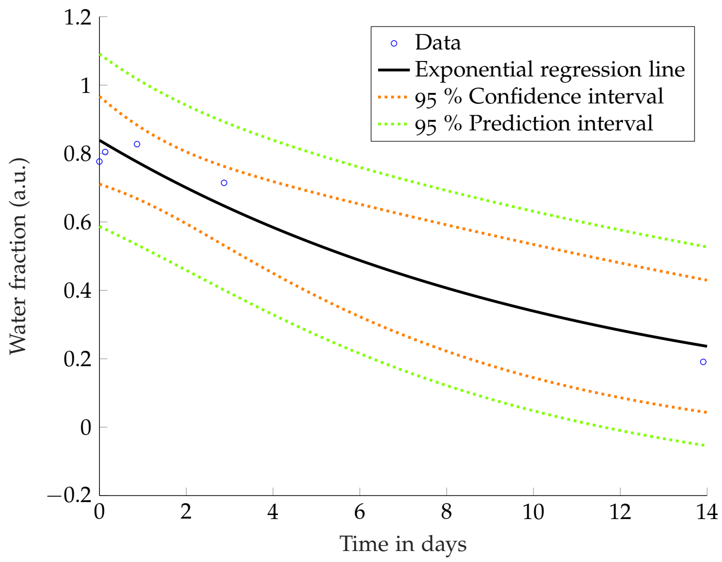

Figure C.52.: Graph of regression model

Table C.155.: Model parameter

Coefficients	a	b
Estimate	0.83873	0.91351
SE	0.040324	0.017868
tStat	20.8	51.125
p-Value	0.00024305	$1.648*10^{-5}$

Parameter estimates and statistically values

Table C.156.: Model parameter

	Confidence interval	Prediction interval
Mean	(0.31387) - (0.63824)	(0.20366) - (0.74846)
SD	(0.2071) - (0.14066)	(0.19279) - (0.15457)

0.95% confidence and 0.95% prediction intervals

Table C.157.: Metrics of regression model

R^2	R^2_{adj}	SSE	SSR	SST	RMSE	pValue
0.951	0.935	0.01395	0.25166	0.28542	0.0682	0.000422

Statistically values for regression model

P35

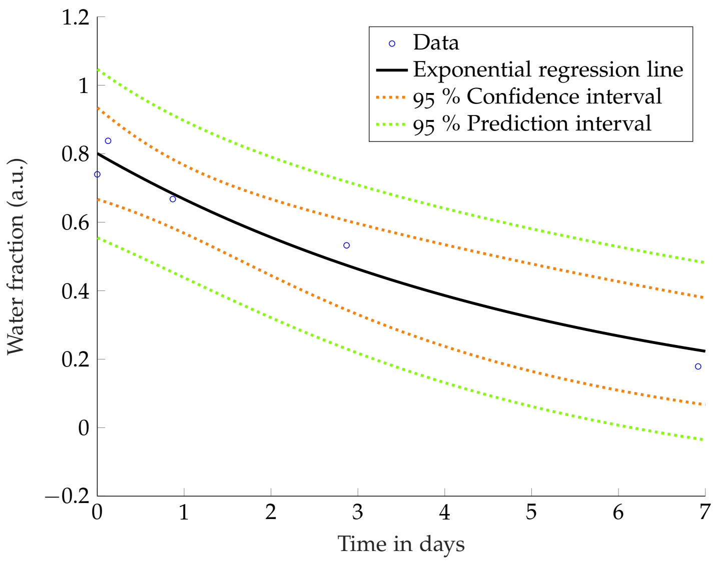

Figure C.53.: Graph of regression model

Table C.158.: Model parameter

Coefficients	a	b
Estimate	0.80084	0.83318
SE	0.042063	0.028614
tStat	19.039	29.118
p-Value	0.00031639	$8.8951 * 10^{-5}$

Parameter estimates and statistically values

Table C.159.: Model parameter

	Confidence interval	Prediction interval
Mean	(0.31747) - (0.58851)	(0.20528) - (0.70071)
SD	(0.18815) - (0.1491)	(0.17892) - (0.15789)

0.95% confidence and 0.95% prediction intervals

Table C.160.: Metrics of regression model

R^2	R^2_{adj}	SSE	SSR	SST	RMSE	pValue
0.952	0.936	0.012636	0.23575	0.26224	0.0649	0.000498

Statistically values for regression model

P36

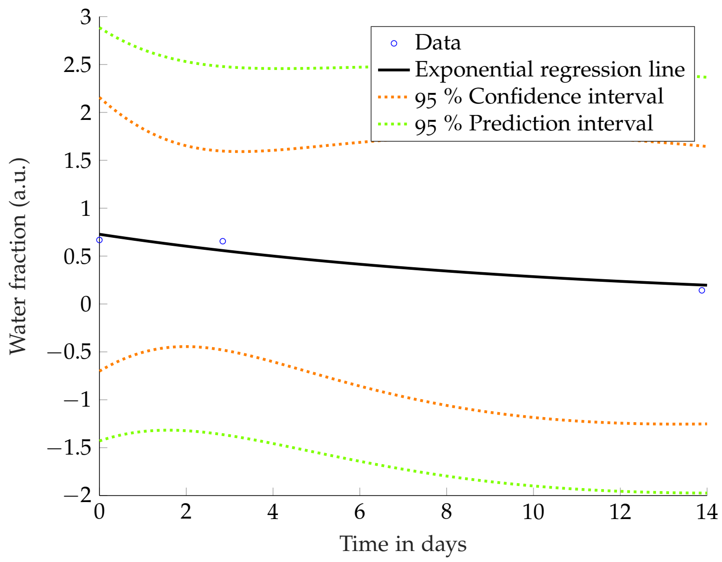

Figure C.54.: Graph of regression model

Table C.161.: Model parameter

Coefficients	a	b
Estimate	0.72774	0.91066
SE	0.11248	0.041539
tStat	6.4698	21.923
p-Value	0.097626	0.029019

Parameter estimates and statistically values

Table C.162.: Model parameter

	Confidence interval	Prediction interval
Mean	(-0.90418) - (1.7162)	(-1.6787) - (2.4907)
SD	(0.29968) - (0.098989)	(0.24149) - (0.092806)

0.95% confidence and 0.95% prediction intervals

Table C.163.: Metrics of regression model

R^2	R^2_{adj}	SSE	SSR	SST	RMSE	pValue
0.91	0.82	0.016185	0.14612	0.17991	0.127	0.134

Statistically values for regression model

P38

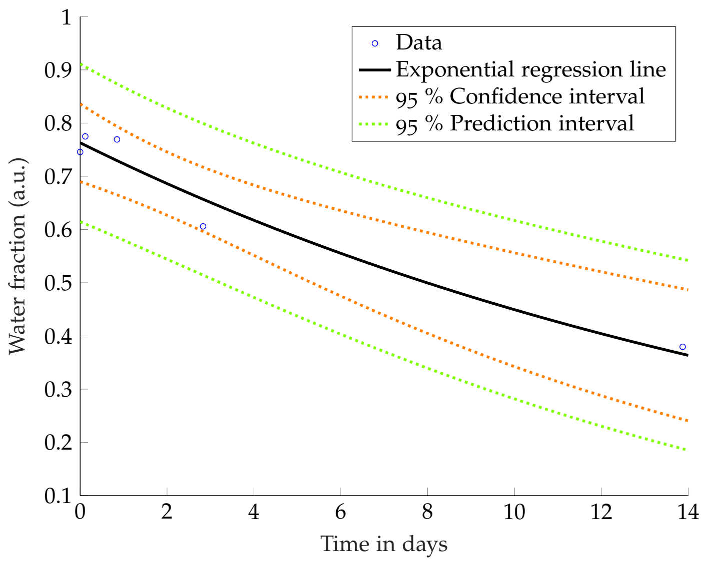

Figure C.55.: Graph of regression model

Table C.164.: Model parameter

Coefficients	a	b
Estimate	0.76302	0.94843
SE	0.022952	0.0078694
tStat	33.245	120.52
p-Value	$5.9827*10^{-5}$	$1.2594*10^{-6}$

Parameter estimates and statistically values

Table C.165.: Model parameter

	Confidence interval	Prediction interval
Mean	(0.4505) - (0.62757)	(0.38149) - (0.69658)
SD	(0.13714) - (0.095313)	(0.12791) - (0.1043)

0.95% confidence and 0.95% prediction intervals

Table C.166.: Metrics of regression model

R^2	R^2_{adj}	SSE	SSR	SST	RMSE	pValue
0.957	0.942	0.0049341	0.11136	0.11395	0.0406	0.000102

Statistically values for regression model

P39

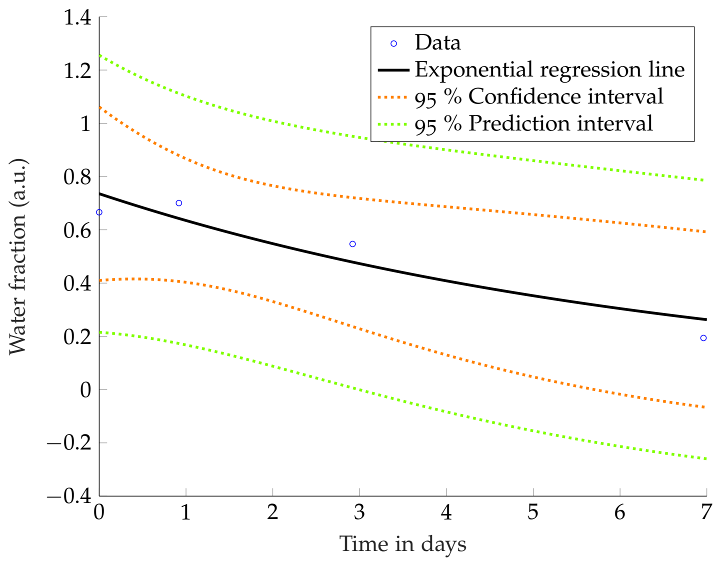

Figure C.56.: Graph of regression model

Table C.167.: Model parameter

Coefficients	a	b
Estimate	0.73558	0.86321
SE	0.075703	0.041712
tStat	9.7167	20.695
p-Value	0.010426	0.0023268

Parameter estimates and statistically values

Table C.168.: Model parameter

	Confidence interval	Prediction interval
Mean	(0.18551) - (0.73415)	(-0.030923) - (0.95059)
SD	(0.16707) - (0.11642)	(0.15379) - (0.12497)

0.95% confidence and 0.95% prediction intervals

Table C.169.: Metrics of regression model

R^2	R^2_{adj}	SSE	SSR	SST	RMSE	pValue
0.889	0.834	0.017772	0.12827	0.16077	0.0943	0.014

Statistically values for regression model

P40

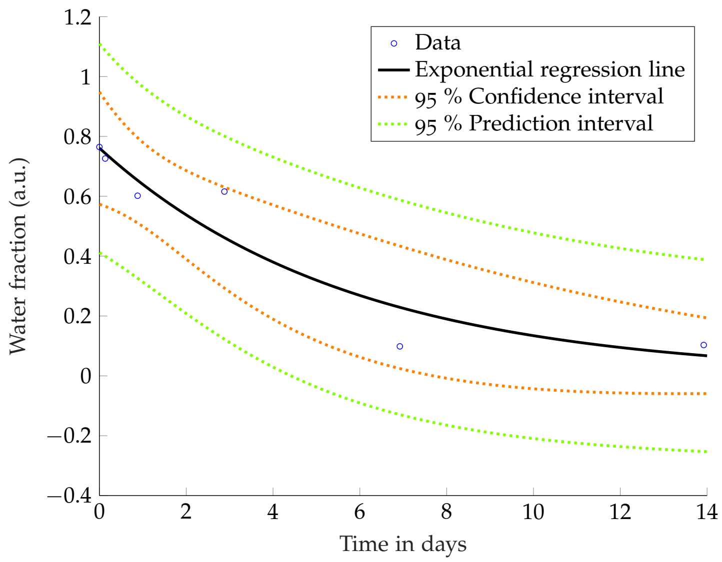

Figure C.57.: Graph of regression model

Table C.170.: Model parameter

Coefficients	a	b
Estimate	0.76081	0.84074
SE	0.067545	0.042974
tStat	11.264	19.564
p-Value	0.00035394	$4.0253*10^{-5}$

Parameter estimates and statistically values

Table C.171.: Model parameter

	Confidence interval	Prediction interval
Mean	(0.11282) - (0.46032)	(-0.055875) - (0.62902)
SD	(0.19733) - (0.19376)	(0.19535) - (0.1934)

0.95% confidence and 0.95% prediction intervals

Table C.172.: Metrics of regression model

R^2	R^2_{adj}	SSE	SSR	SST	RMSE	pValue
0.847	0.796	0.05042	0.2949	0.34532	0.13	0.0076

Statistically values for regression model